

2015

# Probing a Complex Dissociation Energy Surface with Experimental and Theoretical Methods

Hannah Elizabeth Bott  
bott1@marshall.edu

Follow this and additional works at: <http://mds.marshall.edu/etd>

 Part of the [Physical Chemistry Commons](#)

---

## Recommended Citation

Bott, Hannah Elizabeth, "Probing a Complex Dissociation Energy Surface with Experimental and Theoretical Methods" (2015). *Theses, Dissertations and Capstones*. Paper 932.

This Thesis is brought to you for free and open access by Marshall Digital Scholar. It has been accepted for inclusion in Theses, Dissertations and Capstones by an authorized administrator of Marshall Digital Scholar. For more information, please contact [zhangj@marshall.edu](mailto:zhangj@marshall.edu).

PROBING A COMPLEX DISSOCIATION ENERGY SURFACE WITH EXPERIMENTAL  
AND THEORETICAL METHODS

A thesis submitted to  
the Graduate College of  
Marshall University  
In partial fulfillment of  
the requirements for the degree of  
Master of Science  
in  
Chemistry  
by

Hannah Elizabeth Bott

Approved by

Dr. William Price, Committee Chairperson

Dr. Leslie Frost

Dr. B. Scott Day

Marshall University

May 2015

## ACKNOWLEDGEMENTS

*Certainly, above all else, I thank my God and my Savior. All good comes from Him, including the patience, focus, knowledge, and pure will it took to write this thesis.*

*“Whatever work you do, do it with all your heart. Do it for the Lord and not for men.”*

*Colossians 3:23 (NLT)*

*I also have a great deal of gratitude for Dr. Price. Constantly challenging me to learn and question more, he has molded me into the scientist I am today. I would not have been able to complete this project if it were not for his constant support and guidance throughout my three years of research at Marshall.*

*I would also like to thank the members of my committee, Dr. Frost and Dr. Day. Their direction and advice undoubtedly improved this thesis.*

*I would also like to thank the faculty of the Marshall University Department of Chemistry for the constant assistance that fueled the academic growth I experienced throughout my undergraduate and graduate careers.*

*Finally, I would like to thank my family and friends. Without their love and encouragement, I surely would not have the strength it took to make it this far.*

## CONTENTS

LIST OF TABLES .....	iv
LIST OF FIGURES .....	v
ABSTRACT .....	viii
CHAPTER ONE: INTRODUCTION.....	1
INTRODUCTION TO DENDRIMERS .....	1
Dendrimer Synthesis .....	2
Historical Background of Dendrimers .....	3
Types of Dendrimers .....	4
Dendrimer Applications .....	5
METHODS OF DENDRIMER CHARACTERIZATION.....	7
ELECTROSPRAY IONIZATION MASS SPECTROMETRY .....	9
ESI Probe.....	10
Mass Analyzer.....	11
CHAPTER TWO: MOTIVATION.....	13
PREVIOUS ESI-MS DATA .....	14
PREVIOUS COMPUTATIONAL DATA .....	17
DATA INCONSISTENCIES AND RESEARCH METHODS.....	20
CHAPTER THREE: EXPERIMENTAL.....	21
MATERIALS .....	21
METHODS .....	21
Synthesis of 1st Generation Nitrile-terminated PPI Dendrimer.....	21
Synthesis of Isotopically Labeled Dendrimer Cores.....	22
Synthesis of Isotopically Labeled G1 Nitrile-Terminated PPI Dendrimer .....	24
Synthesis of 260 m/z structure .....	25
Alkali and Alkaline Earth Metal Solutions .....	27
Mass Spectrometry.....	28
CHAPTER FOUR: RESULTS AND DISCUSSION.....	29
ISOTOPICALLY LABELED DENDRIMERS.....	29
Hypothesized Isotopic Structures.....	29
CID-ESI-MS Studies of DOC Structures.....	33
CID-ESI-MS Studies of DIC Structures .....	42
ALKALI AND ALKALINE EARTH METAL-DENDRIMER COMPLEXES.....	51
Sodium-Dendrimer Complex .....	51
Potassium-Dendrimer Complex .....	54
Magnesium-Dendrimer Complex.....	56
Calcium-Dendrimer Complex .....	58
CHAPTER FIVE: CONCLUSIONS .....	60
REFERENCES .....	61
APPENDIX A: LETTER FROM INSTITUTIONAL RESEARCH BOARD .....	63
APPENDIX B: SUPPLEMENTARY SPECTRA .....	64

## LIST OF TABLES

Table 1:	Verified structures for DOC 305 m/z G1 dendrimer and daughter ion of 264 m/z.....	36
Table 2:	Verified structures for DIC 305 m/z G1 dendrimer and daughter ion of 264 m/z.....	43
Table 3:	Sodium-dendrimer complex fragmentation structures.....	53
Table 4:	Potassium-dendrimer complex fragmentation structures.....	55
Table 5:	Magnesium-dendrimer complex fragmentation structures .....	57
Table 6:	Calcium-dendrimer complex fragmentation structures .....	59

## LIST OF FIGURES

Figure 1: General structure of a 4 <sup>th</sup> generation (G4) dendrimer with A) core, B) branching interior, C) void spaces, and D) peripheral layer of functional groups.....	1
Figure 2: Schematic of divergent dendrimer synthesis beginning with a core molecule and, with alternating coupling and activation steps, continuing generation addition.....	2
Figure 3: Schematic of convergent dendrimer synthesis in which terminal groups are added to a protecting group and, after reaching desired number of generations, attachment to core.....	3
Figure 4: PPI dendrimer of 1 <sup>st</sup> generation (G1) with terminal amine groups. This dendrimer is activated, allowing addition of more generations.....	4
Figure 5: PPI dendrimer of half generation (G0.5) with terminal nitrile groups. Also referred to as first generation (G1) nitrile-terminated PPI dendrimer. Reduction of terminal groups must occur to create a dendrimer of larger generation.....	5
Figure 6: Scheme depicting analyte ionization process from ESI probe to API source .....	11
Figure 7: Cut-out view of quadrupole ion-trap. Ions enter from API source through ion optics, propelled in the z-direction by the applied RF voltage on the rods.....	12
Figure 8: MS <sup>2</sup> spectra for parent ion of 317 m/z corresponding to 1 <sup>st</sup> generation (G1) amine-terminated PPI dendrimer fragmenting to one structure of 186 m/z.....	14
Figure 9: A) MS <sup>2</sup> spectra for parent ion of 301 m/z corresponding to 1 <sup>st</sup> generation (G1) nitrile-terminated PPI dendrimer having two fragmentation pathways at 260 m/z and 178 m/z. B) MS <sup>3</sup> of 260 m/z daughter ion showing collision-induced dissociation results, demonstrating the fragmentation pattern with daughter ions of high state population at 176 m/z and 137 m/z.....	15
Figure 10: Determined mechanism for loss of neutral 131 fragment seen on right to give 186 m/z daughter ion. ....	16
Figure 11: Graphic representation of CBS-QB3 quantum methods. CBS-QB3 composite methods have shown accuracy within 1.1kcal/mol in comparison with Gaussian 2 (G2) test set.....	18
Figure 12: CBS-QB3 energy surface for the gas-phase dissociation pathways of the 260 m/z ion. Transition states marked in blue. Six dissociation channels in red yield four products.....	19
Figure 13: Michael addition reaction between 1,4-diaminobutane with acrylonitrile in distilled water solvent to give the G1 nitrile-terminated PPI dendrimer. ....	22
Figure 14: Reduction reaction of succinamide with LiAlD <sub>4</sub> in THF to give α-labeled core. ....	23
Figure 15: Reduction reaction of d <sub>4</sub> -succinonitrile with LiAlH <sub>4</sub> in THF to give β-labeled core. ....	24

Figure 16: Michael addition reaction with $\alpha$ -d <sub>4</sub> -diaminobutane and acrylonitrile in distilled water solvent to give isotopically labeled G1 nitrile-terminated PPI dendrimer. ....	25
Figure 17: Michael addition reaction with $\beta$ -d <sub>4</sub> -diaminobutane and acrylonitrile in distilled water solvent to give isotopically labeled G1 nitrile-terminated PPI dendrimer. ....	25
Figure 18: Michael reaction with 1,4-diaminobutane and acrylonitrile in a distilled water solvent, followed by imine formation with excess formaldehyde and methanol to yield 260 m/z product.....	26
Figure 19: Michael reaction with $\alpha$ -d <sub>4</sub> -diaminobutane and acrylonitrile in a distilled water solvent, followed by imine formation with excess formaldehyde and methanol to yield 264 m/z product .....	27
Figure 20: Michael reaction with $\beta$ -d <sub>4</sub> -diaminobutane and acrylonitrile in a distilled water solvent, followed by imine formation with excess formaldehyde and methanol to yield 264 m/z product. ....	27
Figure 21: Hypothesized isotopic structures near the 180 m/z range. Pathways demonstrate many double bond migrations and deuteride shifts, as in the CBS-QB3 energy surface.....	30
Figure 22: Hypothesized isotopic structures near the 140 m/z range. Pathways demonstrate double bond migrations and deuteride shifts, as in the CBS-QB3 energy surface.....	32
Figure 23: MS <sup>2</sup> of DOC 305 m/z synthesized dendrimer conducted at activation amplitude of 23% and normal activation time of 30 ms resulting in two fragmentation pathways of 264 m/z and 182 m/z.....	33
Figure 24: MS <sup>2</sup> of DOC 305 m/z synthesized dendrimer conducted at activation amplitude of 42% and faster activation time of 3 ms resulting in the same two fragmentation pathways, but larger relative abundance of 264 m/z in comparison to 30 ms kinetic window. ....	34
Figure 25: MS <sup>3</sup> of 264 m/z daughter ion at normal kinetic window of 30 ms yielding two fragmentation pathways of large relative abundances at 179 m/z and 141 m/z.....	35
Figure 26: MS <sup>2</sup> of directly synthesized DOC 264 m/z species at activation amplitude of 28% and activation time of 30 ms yielding daughter ions at 179 m/z and 141 m/z.....	36
Figure 27: Zoom scan around 179 m/z for the DOC MS <sup>3</sup> spectrum. ....	37
Figure 28: Favored mechanisms for DOC MIN 1A.1 264 m/z structure yielding predominately 179 m/z with MIN 2A.1 and MIN 3A.1 transition states and only slight population of saturated ring structure of 182 m/z from direct nucleophilic substitution .....	39
Figure 29: Zoom scan around 141 m/z for the DOC MS <sup>3</sup> spectrum. ....	40
Figure 30: Favored mechanism for formation of highly populated 141 m/z unsaturated ring structure from the MIN 1A.1 264 m/z, as well as 140 m/z and 143 m/z ring structures.....	41
Figure 31: MS <sup>2</sup> of DIC 305 m/z synthesized dendrimer conducted at activation amplitude of 17% and normal activation time of 30 ms resulting in two fragmentation pathways of 264 m/z and 182 m/z.....	42

Figure 32: MS <sup>2</sup> of DIC 305 m/z synthesized dendrimer conducted at activation amplitude of 43% and activation time of 4 ms resulting in same two daughter ions as previous spectrum, however a 20% relative abundance increase for the 264 m/z daughter ion.....	44
Figure 33: MS <sup>3</sup> of 264 m/z daughter ion at normal kinetic window of 30 ms yielding two fragmentation pathways of large relative abundances at 179 m/z and 140 m/z.....	45
Figure 34: Zoom scan around 179 m/z for the DIC MS <sup>3</sup> spectrum.....	46
Figure 35: Favored mechanisms for DIC MIN 1A.1 264 m/z structure yielding predominately 179 m/z with MIN 2A.1 and MIN 3A.1 transition states and only slight population of 182 m/z from direct nucleophilic substitution.....	47
Figure 36: Zoom scan around 140 m/z for DIC MS <sup>3</sup> spectrum.....	48
Figure 37: Favored mechanism for formation of highly populated 140 m/z unsaturated ring structure from the MIN 1A.1 264 m/z, as well as the 143 m/z ring structure.....	49
Figure 38: Proposed mechanism for MIN1A.2 transition to MIN 2A.2 explaining appearance of 141 m/z in DIC MS <sup>3</sup> .....	50
Figure 39: MS <sup>2</sup> of sodium-dendrimer complex with activation time of 30 ms.....	51
Figure 40: MS <sup>3</sup> of sodium-dendrimer complex with activation time of 30 ms.....	52
Figure 41: MS <sup>2</sup> of potassium-dendrimer complex with activation time of 30 ms.....	54
Figure 42: MS <sup>2</sup> of magnesium-dendrimer complex with activation time of 30 ms....	56
Figure 43: MS <sup>2</sup> of calcium-dendrimer complex with activation time of 30 ms.....	58



## ABSTRACT

Dendrimers are hyperbranched polymers with a tree-like structure that can be tuned for size, shape, and functionality. Dendrimers have exhibited numerous possibilities in chemical and biochemical processes as their use in host-guest systems and controlled gene and drug delivery vehicles. Distinct properties of dendrimers, such as well-defined architecture and high ratio of functional moieties to molecular volume, make these polymers substantially useful for the development of nanomaterials and medicines. It has recently been demonstrated that polypropylene-imine (PPI) dendrimers have specific physical properties that are well suited for many applications. More specifically, the nitrile-terminated dendrimer creates a unique environment that is both aprotic and polar. Increasing interest in the design and use of these dendrimer systems has created a need for new methods of physical and chemical characterization. The current techniques used for characterization tend to be slow and sample limited, even for monodisperse samples. Polydisperse samples are even more analytically challenging. This thesis used a rapid and precise analytical framework for the characterization of dendrimers by systematically probing the electrospray ionization mass spectrometry (ESI-MS) speciation and the gas-phase collision-induced dissociation (CID) fragmentation patterns for early generation (PPI) dendrimers. Two isotopically labeled dendrimer species were employed for unambiguous assignment of complex structures and mechanisms. Hypothesized mechanisms were verified, while one anomaly presented for the  $\beta$ -labeled dendrimer. Also, the fragmentation patterns of certain alkali and alkaline earth metal-dendrimer complexes were investigated. These complexes of +1 and +2 charges exhibited similar losses, including radicals.

# CHAPTER ONE

## INTRODUCTION

### INTRODUCTION TO DENDRIMERS

Dendrimers are hyperbranched polymers with a tree-like structure with size, shape, and functionality that can be tuned for a variety of purposes. Their unique structures, unmatched by traditional linear polymers, allow for use in a considerable amount of applications stretching across many fields. These macromolecules tend to possess distinctive properties such as well-defined architecture, monodispersity, and high ratio of functional moieties to molecular volume, rendering dendrimers highly suitable for many sensitive functions.

The general architecture of a dendrimer is seen in Figure 1. Instead of the common linear form of many polymers, dendrimers branch from a central monomer, or initiator core. Each layer of branching constitutes a new generation, indicated by each concentric circle in Figure 1. With successive addition of generations, void spaces begin to form within the interior. The periphery is created from the packing together of functional groups, dependent upon the composition of the monomer, which allows for chemical modification.

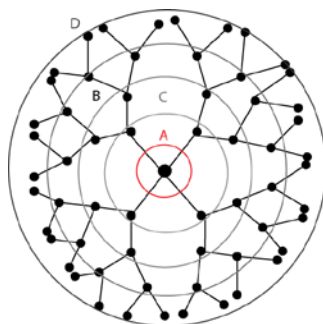


Figure 1. General structure of a 4<sup>th</sup> generation (G4) dendrimer with A) core, B) branching interior, C) void spaces, and D) peripheral layer of functional groups.

## Dendrimer Synthesis

Dendrimers have two synthetic approaches – divergent and convergent. As the name suggests, divergent synthesis begins at a core molecule and grows out to the periphery after successive addition of monomers with repeated coupling and activation steps as seen in Figure 2.<sup>1</sup> Inversely, convergent synthesis has a step-wise method where segments of the dendrimers are synthesized inwardly from terminal groups as seen in Figure 3. Once the segments, or dendrons, are large enough, they are attached to the core. Each form of synthesis has its inherent strengths and weaknesses. Divergent synthesis is ideal for large-scale production of dendrimers due to the inherent control that exists with the coupling and activation steps. However, because the number of branches increases exponentially with increasing generations, the probability of incomplete functionalization or undesirable side reactions also increases with divergent synthesis.<sup>1</sup> In contrast, convergent synthesis provides greater structural control, providing the attractive capabilities such as precisely placing functional groups throughout the structure, selectively modifying the focal point or the chain ends, and preparing well-defined asymmetrical dendrimers. Nevertheless, convergent synthesis pathways suffer such disadvantages as significant loss of product with succeeding coupling reactions and steric hindrance that prevents synthesis of dendrimers larger than approximately six generations.<sup>1</sup>

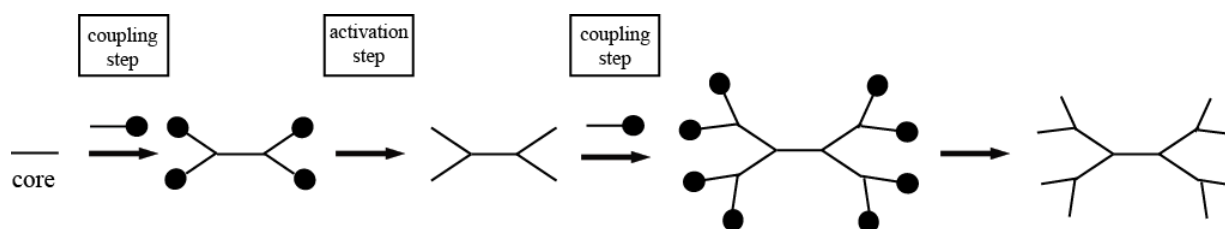


Figure 2. Schematic of divergent dendrimer synthesis beginning with a core molecule and, with alternating coupling and activation steps, continuing generation addition.

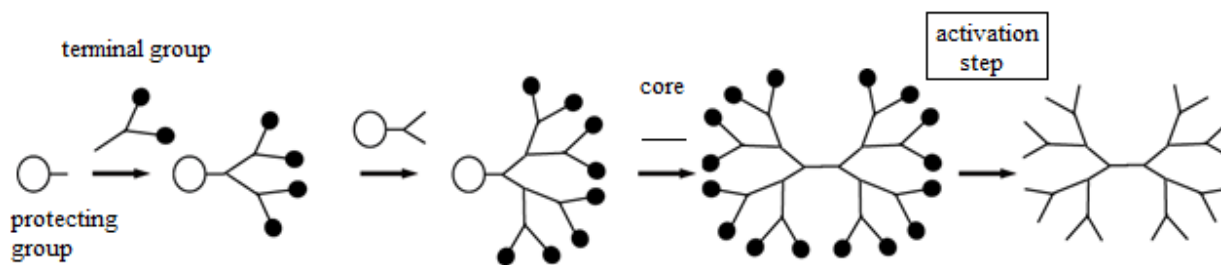


Figure 3. Schematic of convergent dendrimer synthesis in which terminal groups are added to a protecting group and, after reaching desired number of generations, attachment to core.

### Historical Background of Dendrimers

The very idea of a dendrimer-like polymer was envisioned in the early 1970s by Donald A. Tomalia, a synthetic polymer chemist for Dow Chemical, whose interest in horticulture fueled his desire to synthesize a polymer that exhibited branching, which one might see in biotic systems.<sup>2</sup> In 1978, Fritz Vögtle et al reported the first dendrimer prototype using cascade synthesis with low yields, difficult product isolation, and inability to produce large enough molecules.<sup>3</sup> The “cascadane” molecule that would later be known as the polypropylene imine (PPI) dendrimer required that the terminal cyano groups be reduced in order to increase its generation size. The homogeneous reducing agent  $\text{CoCl}_2/\text{NaBH}_4$  was first used, which presumably complexed with the resulting product, causing the low yields and difficult product isolation. Eventually, in a modified synthesis constructed by Mülhaupt and Meijer at DSM, the cyano groups were reduced with  $\text{H}_2$  on Raney cobalt.<sup>4</sup> Soon after Vögtle et al had introduced their flawed cascadane synthesis, the first true dendrimer was presented in 1984 at the First Polymer Conference for the Society of Polymer Science in Japan by the Tomalia group, then reported in 1985, wherein the detailed synthesis of the polyamidoamine (PAMAM) dendrimer was outlined.<sup>5,6</sup> Another notable group in the history of dendrimer discovery is the Meijer group

that discovered the potential of these types of polymers to be used as “dendritic boxes” in 1994. The group enclosed rose Bengal and p-nitrobenzoic acid molecules inside of a fifth generation PPI dendrimer.<sup>7</sup>

## Types of Dendrimers

There are various ways to categorize dendrimers. First, as previously mentioned, dendrimers are described by generation number. Each new layer of branching groups added comprises another generation. Non-activated end groups of an added generation would be a half-generation. Below are two examples – Figure 4 exhibits a G1, or first generation, PPI dendrimer, whereas Figure 5 shows the closely related G0.5, or half generation, PPI dendrimer. The only difference is the terminal functional group in which the full G1 has activated terminal amine groups and the G0.5 has non-activated terminal nitrile groups. Dendrimers will also be categorized by the monomers that create the branches. The PPI dendrimer is also referred to as POPAM, or Polypropylene Amine, designating its propylene amine branches.<sup>8</sup> Finally, a dendrimer is also defined by its core, as a PPI dendrimer will also be titled as DAB-dendrimer for its diaminobutane core.<sup>8</sup>

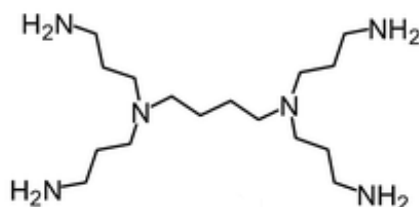


Figure 4. PPI dendrimer of 1<sup>st</sup> generation (G1) with terminal amine groups. This dendrimer is activated, allowing addition of more generations.

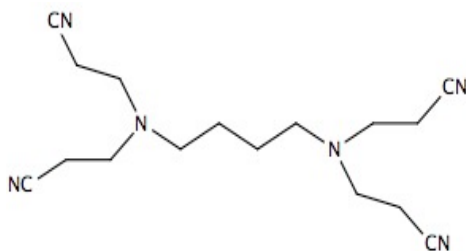


Figure 5. PPI dendrimer of half generation (G0.5) with terminal nitrile groups. Also referred to as first generation (G1) nitrile-terminated PPI dendrimer. Reduction of terminal groups must occur to create a dendrimer of larger generation.

The nitrile-terminated PPI dendrimer described above is the primary focus of this research, and will therefore be the dendrimer predominantly discussed. However, it should be noted that there are several other dendrimer designs, such as the previously mentioned PAMAM dendrimer, as well as Fréchet-type dendrimers with polybenzyl ether branching, or even dendrimers with biologically relevant building blocks like carbohydrates, amino acids, and nucleotides, all of which could have vastly different applications.<sup>8</sup>

### **Dendrimer Applications**

A great deal of research has shown the numerous ways dendrimers could be used to enhance the technology of many different fields. Perhaps most acclaimed is the ability of dendrimers to be used in target-specific gene and drug delivery.<sup>9,10</sup> Due to the nature of their structure, with its spherical shape and internal void spaces, dendrimers are highly suited for encapsulation of drugs. The hydrophobic nature of dendrimer void spaces allows for interactions with drugs which are poorly soluble in aqueous solution.<sup>10</sup> Furthermore, the high density of peripheral functional groups allows dendrimers to provide both electrostatic interaction and covalent conjugation upon drug contact to the exterior surface. Any of these three options for

drug interaction mechanisms will create viable drug delivery systems, with release of drug at target occurring through either environmental changes – such as temperature or pH – effectively releasing encapsulated and electrostatically-bound drugs, or chemical or enzymatic hydrolysis of covalent dendrimer-drug bonds.<sup>10</sup>

In a similar sense, PAMAM and PPI dendrimers have been proven as successful vectors in gene therapy, providing more efficient transport of DNA into the cell nucleus than viruses or liposomes.<sup>10</sup> Not only can this be attributed to the well-defined architecture of the spherical polymers, but also the low pKa of their peripheral amine groups. The amines provide a buffer for the changing pH of the endosomal compartment, achieving secure delivery of the genetic material into the cell.<sup>10</sup>

Dendrimers have also found use in catalyst chemistry as carriers for metal nanoparticles. The attractive qualities for dendrimer-metal complexes in catalysis include prevention of nanoparticle agglomeration, unpassivated confinement of nanoparticles, selective gating of small substrates to the encapsulated nanoparticles, and adjustability of dendrimer periphery to control solubility of the hybrid nanocomposite.<sup>11</sup> Metallodendrimers have four different general configurations that are solely dependent on the location of the metal – dendrimer-encapsulated metal nanoparticles (DEMNs), dendrimers modified on the periphery with metal ions or complexes, core metallodendrimers, and focal-point metallodendrimers.<sup>11</sup> Of the four configurations, DEMNs tend to be very attractive for many catalytic reactions due to the commercial availability of PAMAM and PPI dendrimers, while the other three configurations require complete synthesis.

A very important palladium-catalyzed reaction in organic chemistry is the Heck reaction, a carbon-carbon coupling between aryl halides or vinyl halides and activated alkenes. Phosphine

ligands are normally used to stabilize the palladium complex, but due to its toxicity and high cost, efforts have been made towards finding operational phosphine-free systems.<sup>12</sup> Research has shown that PAMAM dendrimers can encapsulate these Pd-nanoparticles to be used for the Heck reaction and the yields are fully comparable to that of a classical Heck procedure.<sup>13</sup>

With the aim of refining the design of artificial energy harvesting materials, research teams have sought after characteristics responsible for the high levels of efficiency in a wide variety of biomolecular systems that could harness solar energy. A key goal has been the accomplishment of similar levels of efficiency in synthetically less demanding materials, achieved by emulating the photobiological principles of photon capture.<sup>14</sup> Dendrimers proficiently fulfill this goal. Using a multiplicity of peripheral chromophores, typically in the form of benzene rings, these light harvesting molecules absorb photons, producing short-lived electronic excited states, then utilize their inherent mechanism for rapid transfer of resulting excitation towards a central trapping site – also referred to as a stepwise resonance energy transfer (RET).<sup>14</sup> This is the same sequence of events that occurs in typical solar energy capture materials, but dendrimers provide repeated branching that supports a special proliferation of chromophores on the outermost surface, as well as inner, chromophores that act with high efficiency as transient hosts for excited energy transfer to the central trap.<sup>14</sup>

## METHODS OF DENDRIMER CHARACTERIZATION

As made apparent by the small glimpse of a much larger picture of amassing dendrimer applications, these macromolecules are becoming increasingly vital to a number of scientific fields. Increasing interest in the design and use of these dendrimer systems has created a need for new methods of physical and chemical characterization. Currently, a wide array of instrumentation is used, each having its particular advantages for specific aspects of study.



Prevalent features for research include chemical composition, morphology, shape, and homogeneity of all types of dendrimers. Depending on desired area of analysis, certain instrumentation is more applicable.

A widely used routine analysis for dendrimers is nuclear magnetic resonance (NMR). NMR is particularly valuable during stepwise synthesis of dendrimers, even in higher generations, because it offers information about the chemical transformations undergone by peripheral functional groups.<sup>15</sup> Organic dendrimers, such as PPI, are commonly observed by <sup>1</sup>H- and <sup>13</sup>C-NMR, but often selective irradiation or more complex pulse sequences are necessary for better assignment. Similar examination of change in terminal functional groups can be performed with infrared (IR) and Raman spectroscopy.<sup>17</sup>

For such applications as the light-harvesting dendrimer antennas previously discussed, UV-Visible spectroscopy (UV-Vis) is preferential for characterization. This form of spectroscopy is useful for monitoring dendritic systems in which there is a growth and decay of the metal-to-ligand charge transfer band, and the intensity of the absorption band is proportional to the number of chromophoric units.<sup>15</sup> UV-Vis can also assist in determination of dendrimer purity, but this is restricted only to dendrimers with light absorbing functional groups, such as azobenzene, in the branches or at the terminal ends.

Mass spectrometry is normally considered to be one of the best methods to investigate dendrimers with respect to the presence and the nature of structural defects. It allows for environment-free conditions, and consequently, is very beneficial to use such instrumentation to examine the gas-phase chemistry, providing valuable new insight into properties which cannot easily be studied in solution.<sup>16</sup> Classical mass spectrometry techniques, such as chemical ionization (CI) or fast atom bombardment (FAB) are confined to use for small dendrimers due to

their mass limitations, but other techniques frequently used for protein characterization are fitting for most dendrimers.<sup>15</sup> Soft ionization techniques are employed due to excessive branching in dendrimer structures that could be too difficult to define with hard ionization techniques, like electron ionization (EI) mass spectrometry. Therefore, characterization of dendrimers is typically carried out with matrix-assisted laser desorption ionization time of flight (MALDI-TOF) or electrospray ionization mass spectrometry (ESI-MS), which use lasers and electrically-charged aerosol droplets, respectively, to ionize the analytes of interest. Both methods of ionization are powerful tools for dendrimer analysis due to their capability to gently transfer species from solution to the gas-phase while minimizing the fragmentation of the sample, permitting accurate molecular weight measurements and minimal sample consumption.

#### ELECTROSPRAY IONIZATION MASS SPECTROMETRY

For the purposes of this study that focuses on fragmentation of dendrimer species, ESI-MS is preferentially employed. As previously mentioned, ESI-MS is a soft ionization technique that utilizes an applied voltage to ionize an analyte of interest. Remarkably enough, the very idea of electrospray ionization was imagined, not by a biochemist in search of better protein characterization techniques, but a physical chemist searching for a mass spectrometry method that would better suit non-volatile synthetic polymers.<sup>18</sup> In 1966, Professor Malcolm Dole of Northwestern University conceived the idea of ESI which led to his infamous paper in 1968.<sup>19</sup> The paper detailed his proposal to utilize an ionization method that could take advantage of what happens during the evaporation of solvent from a droplet that has a net electric charge. The paper also presented his preliminary experimental results using a solution of polystyrene molecules infused through a small bore tube maintained at high potential relative to a counter electrode.<sup>19</sup> Purportedly, Dole conceived this idea from learning about the electro spraying of paint on to

automobile bodies while working as a consultant for a paint company in Chicago.<sup>20</sup> The electro spraying of paint relies on maintaining a potential difference between the sprayer and the object being painted. The result is enough charge on the paint droplets to attract them toward the object being painted, thereby decreasing substantially the loss of paint to the surroundings by convection currents.<sup>20</sup> However, due to the unavailability of mass analyzers that could detect a large enough molecule size, Dole was incapable of using ESI in a mass spectrometer with the polystyrene molecules he wanted to examine. It was not until 1982 that the first fully-operational ESI-MS was constructed and demonstrated in Dr. John Fenn's lab at Yale University by a post-doc student.<sup>20</sup>

### **ESI probe**

ESI is useful for large non-volatile, polar molecules that are heat-labile, normally unable to be studied with conventional mass spectrometry methods.<sup>21</sup> Analyte in solution is injected into the system through the syringe pump. Continuous sample is pumped through a capillary into the atmospheric pressure ionization (API) source where it is nebulized with nitrogen gas, rendering the sample to gaseous form. An applied voltage, commonly in the range of 2kV-6kV, is applied to the needle, spraying the sample solution into a fine mist of charged droplets.<sup>18</sup> The ESI probe can be seen in Figure 6.

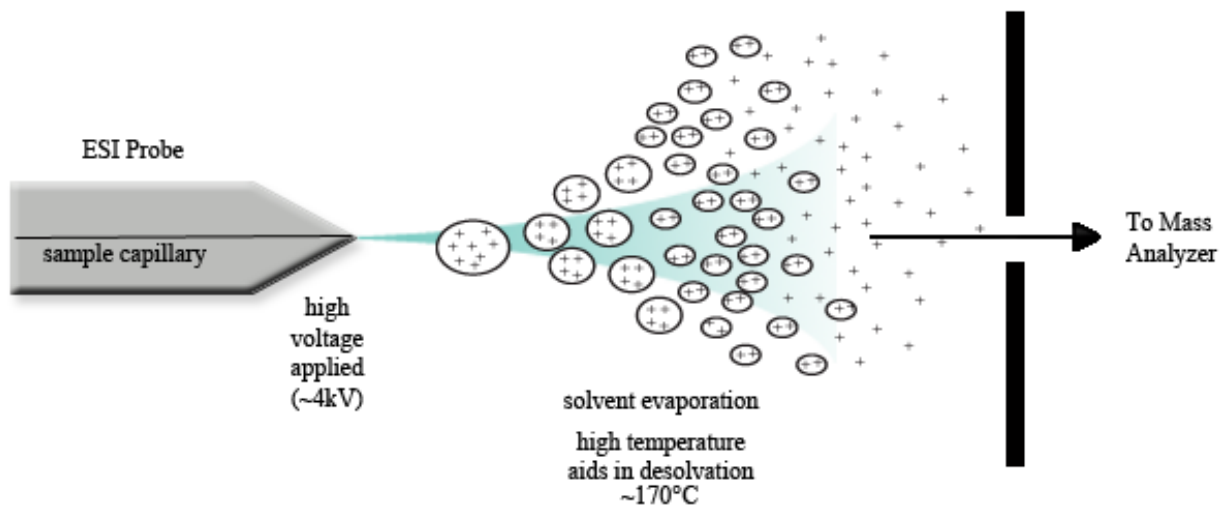


Figure 6. Scheme depicting analyte ionization process from ESI probe to API source.

Demonstrated in Figure 6, the sample leaves the ESI probe and enters the API source as a large charged droplet, containing both analyte of interest and solvent. The solvent is volatile, commonly methanol or acetonitrile. A combination of the nitrogen gas and the relatively low atmospheric pressure in the API source promotes solvent evaporation.<sup>20</sup> As the solvent evaporates, the density of charges on the surface increases to a critical value, known as the Rayleigh limit, when Coulomb repulsion overcomes surface tension.<sup>22</sup> This phenomenon continues until the analyte is almost entirely desolvated.

### Mass Analyzer

Ions then travel through a heated ion transfer capillary which further aids in desolvation of the sample. It is then that the ions are transferred through ion optics into the mass analyzer. The mass analyzer is the location of ion storage, ion isolation, collision-induced dissociation (CID) and ion scanout.<sup>23</sup> A quadrupole ion-trap is the mass analyzer in the instrument used for this research. Quadrupole refers to the existences of four parallel metal rods, each opposing rod being electrically connected. Between the two pairs of rods, a radio-frequency (RF) voltage is

applied, producing a three-dimensional quadrupole field. Ions are driven into the field in the z-direction as seen in Figure 7.

During ion scanout, when an ion of specific mass-to-charge ratio is selected and isolated, the RF voltage is increased, causing all other ions to become unstable in the x,y-direction. At this point, the ions not selected are ejected from the ion trap. With one single isolated ion of specific mass-to-charge ratio, it is now possible to perform collision-induced dissociation. This experimental method allows a parent-ion, created from direct ionization by electrospray, to collide with helium gas, a neutral collision activation partner. Collisions between the parent ion and a neutral target gas are accompanied by an increase in internal energy, which induces fragmentation.<sup>24</sup> This action is also referred to as tandem mass spectrometry (MS/MS or MS<sup>n</sup>) and results in the creation of daughter ions. Continuing steps of specific daughter ion isolation and subsequent collision-induced dissociation can be accomplished, up to n=10, yielding a unique fragmentation pathway.

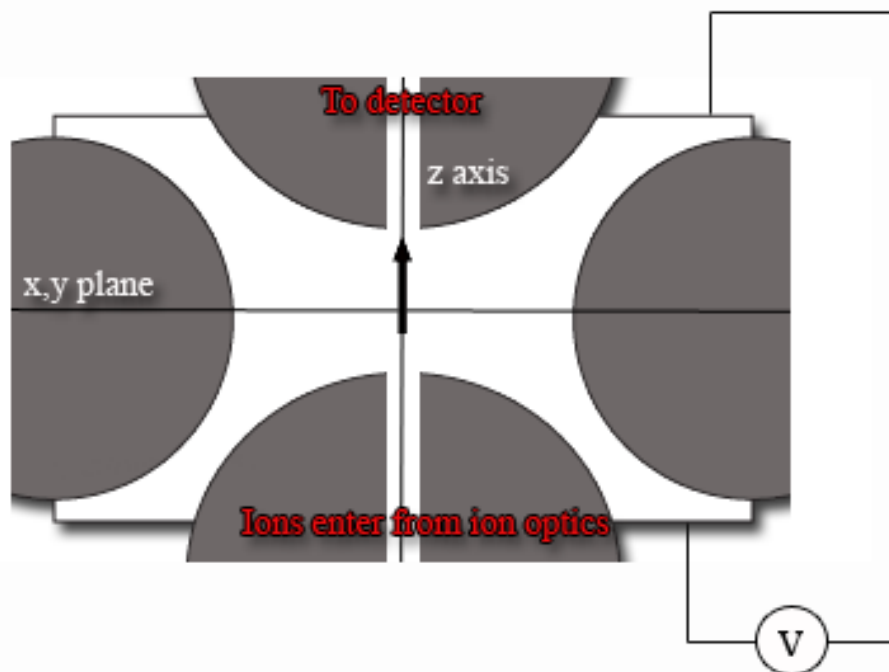


Figure 7. Cut-out view of quadrupole ion-trap. Ions enter from API source through ion optics, propelled in the z-direction by the applied RF voltage on the rods.

## CHAPTER TWO

### MOTIVATION

The primary motivation behind this thesis is to improve upon a rapid and precise analytical framework to characterize nitrile-terminated PPI dendrimers. The list of possibilities for this particular dendrimer system could be as expansive as its amine-terminated counterpart, yet completely distinctive. The absence of any published research to investigate the nitrile-terminated PPI dendrimer is evident. Nitrile-terminated PPI dendrimers create a unique environment which is both aprotic and polar, unlike that of the closely related amine-terminated PPI dendrimer. To analyze the structure, and consequently its behavior in gas-phase, of the nitrile-terminated PPI dendrimer is to comprehend the capabilities it possesses in future applications. In order to create such an analytical framework, the complete fragmentation pathways of such species must be accurately elucidated. This research is designed to develop a rapid and precise analytical framework for the characterization of dendrimers by systematically probing the ESI-MS speciation and the gas-phase CID fragmentation patterns and mechanisms for early generation PPI dendrimers. ESI-MS has not been used extensively for characterizing dendrimers; however, it has been successfully applied in the characterization of the structure and stability of biopolymers, classical polymers, and non-covalent and organometallic complexes. Additionally, understanding the gas-phase chemistry of dendrimers may play a critical role in determining the stability of the polymer by providing insight into the physical properties and reactions that dominate these particular molecules. The CID-ESI-MS data is most effectively used to elucidate structure and mechanistic pathways if it is augmented by computational methods which are presented.

## PREVIOUS ESI-MS DATA

Previous research in this lab has been conducted to elucidate pathways of the amine- and nitrile-terminated G1 and G2 PPI dendrimers complexed with various metals.<sup>25,26</sup> The former, as well as previous studies in other lab groups, also conducted research on fragmentation of the 1<sup>st</sup> generation amine-terminated PPI dendrimer in the absence of a metal ion, demonstrating the gas-phase fragmentation mechanisms of PPI dendrimers as suggested by tandem mass spectrometry.<sup>25,16,27</sup> Research then focused on nitrile-terminated PPI dendrimers and their respective fragmentation pathways.<sup>28</sup> The original spectra for both amine- and nitrile-terminated PPI dendrimers are displayed in Figures 8 and 9.<sup>25,26</sup>

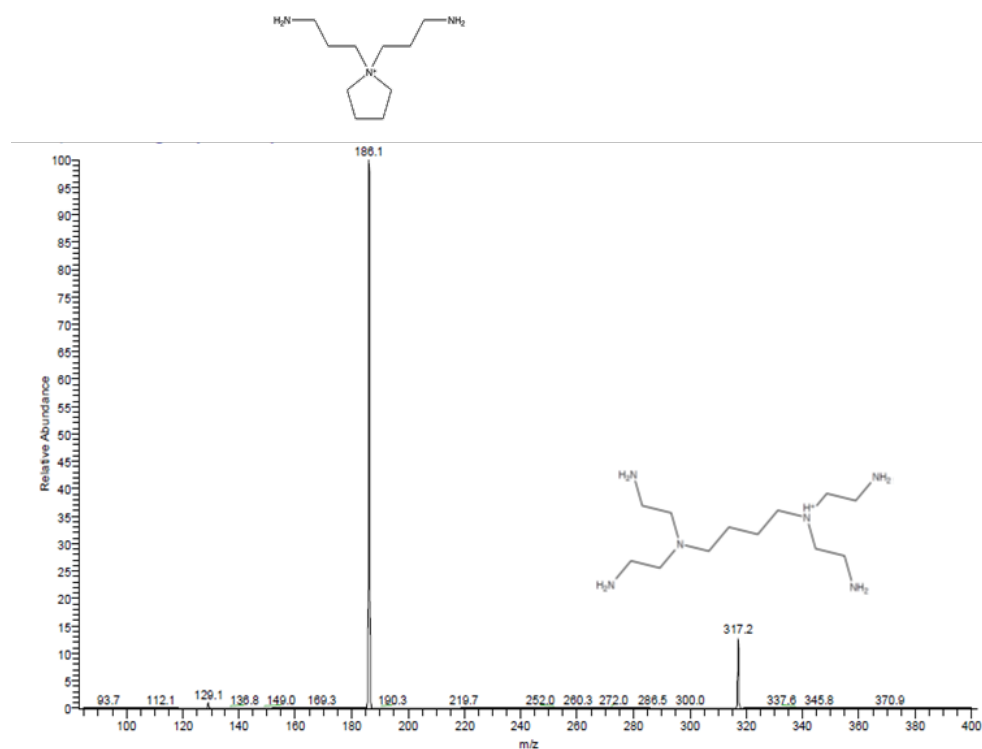


Figure 8. MS<sup>2</sup> spectra for parent ion of 317 m/z corresponding to 1<sup>st</sup> generation (G1) amine-terminated PPI dendrimer fragmenting to one structure of 186 m/z.

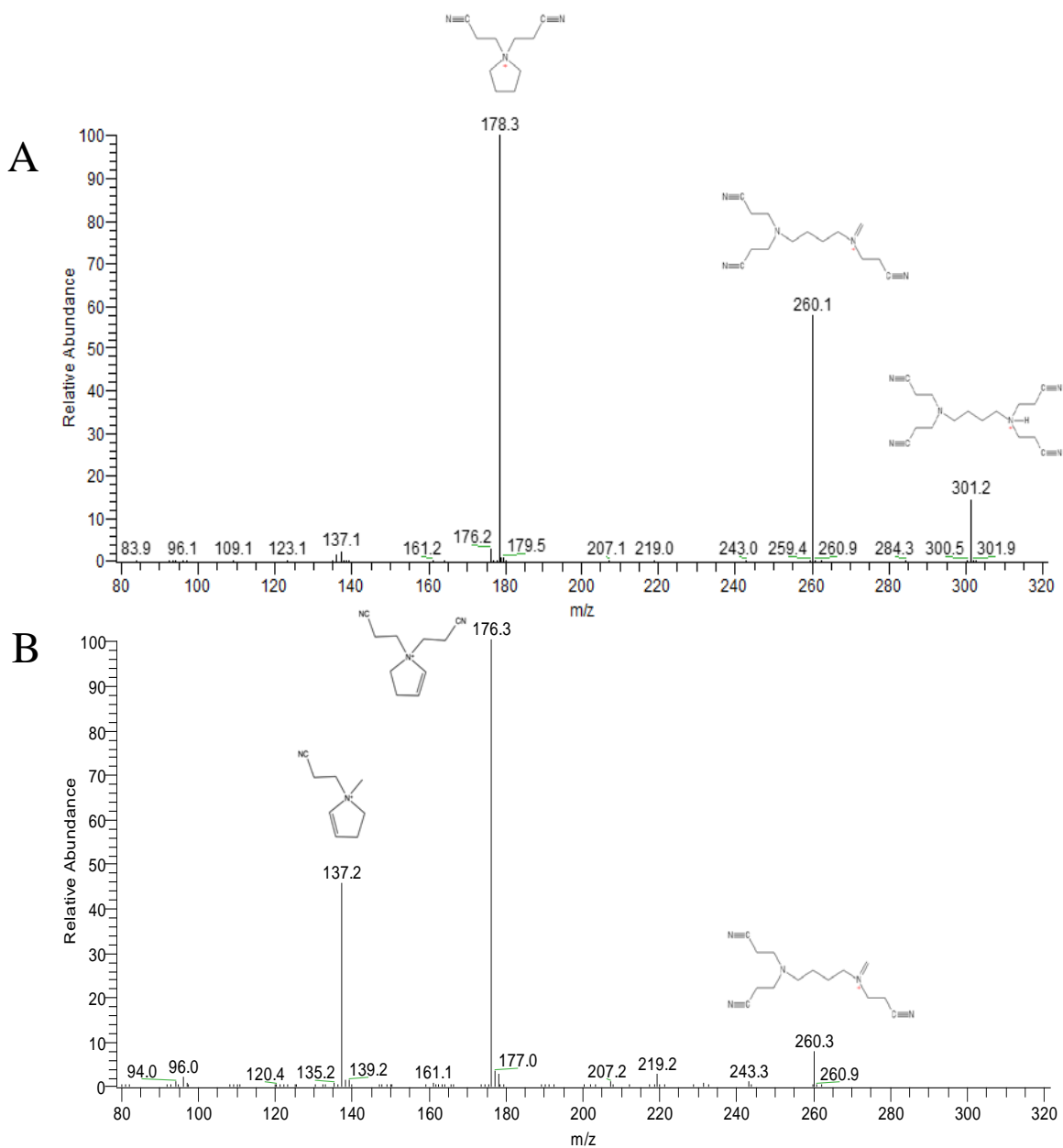


Figure 9. A) MS<sup>2</sup> spectra for parent ion of 301 m/z corresponding to 1<sup>st</sup> generation (G1) nitrile-terminated PPI dendrimer having two fragmentation pathways at 260 m/z and 178 m/z. B) MS<sup>3</sup> of 260 m/z daughter ion showing collision-induced dissociation results, demonstrating the fragmentation pattern with daughter ions of high state population at 176 m/z and 137 m/z.



The multiple low-energy CID conditions and 30 ms kinetic window used in both experiments are not expected to develop an effective internal temperature ( $T_{\text{eff}}$ ) of more than 500 K. Under these conditions, a simple Eyring analysis of the relative abundance of these ions shows that the  $\Delta G^\ddagger$  for these competing pathways must be less than 10 kJ/mole.

Notably, the G1 amine-terminated PPI dendrimer has only one pathway of fragmentation with parent ion of 317 m/z experiencing a loss of neutral 131 mass units for a daughter ion of 186 m/z. The mechanism for this fragmentation is presented in Figure 10.<sup>25</sup> On the other hand, the G1 nitrile-terminated PPI dendrimer has two pathways of fragmentation having parent ion of 301 m/z with a loss of 41 mass units to give a daughter ion of 260 m/z, as well as a loss of 123 mass units to give a daughter ion of 178 m/z.

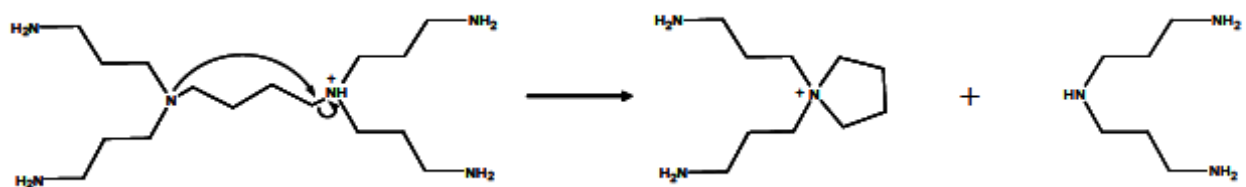


Figure 10. Determined mechanism for loss of neutral 131 fragment seen on right to give 186 m/z daughter ion.

This research seeks to elucidate further down the 260 m/z fragmentation pathway since no corresponding pathway exists for the amine-terminated PPI dendrimer. Upon first examination of the  $MS^3$  for the 260 m/z structure, it would seem as though there are only two structures of interest – the two fragments at 176 m/z and 137 m/z. Ab initio quantum calculations were performed in order to verify that which is seen in the experimental CID-ESI-MS data.

## PREVIOUS COMPUTATIONAL DATA

As previously stated, the CID-ESI-MS is most effective when coupled with computational methods. Previous research focused on modeling the gas-phase dissociation energy surface for the transition states and respective products resulting from fragmentation of the 260 m/z structure.<sup>29</sup> This research was accomplished with complete basis set-quadratic Becke3 (CBS-QB3) quantum calculations. Normally, the accurate computation of thermochemical quantities requires the use of elaborate quantum mechanical methods accounting for both static and dynamic electron correlation effects, as well as the limitations of finite basis sets. Unfortunately, such methods have very high computational cost and are therefore confined to small system investigations. Composite methods have been developed with the aim of reaching chemical accuracy in larger systems. The CBS-QB3 method belongs to a family of Complete Basis Set (CBS) methods developed by Petersson and co-workers that falls under the umbrella of composite methods.<sup>30</sup> In these calculations, the following steps are involved. Optimization and frequency calculations are performed at the B3LYP/CBSB7 level. Afterwards, single point calculations are performed at CCSD(T)/6-31+G(d') and MP4SDQ/CBSB4 levels. The total energy is extrapolated to the infinite-basis-set limit using pair natural-orbital energies at the MP2/CBSB3 level and an additive correction to the CCSD(T) level.<sup>30</sup> Figure 11 graphically demonstrates the benefits of using CBS-QB3 quantum methods. Theoretically, exact molecular energies are calculated by full electron correlation, or full configuration interaction (Full CI) and full basis set of the chemical system, but this is far too computationally expensive.

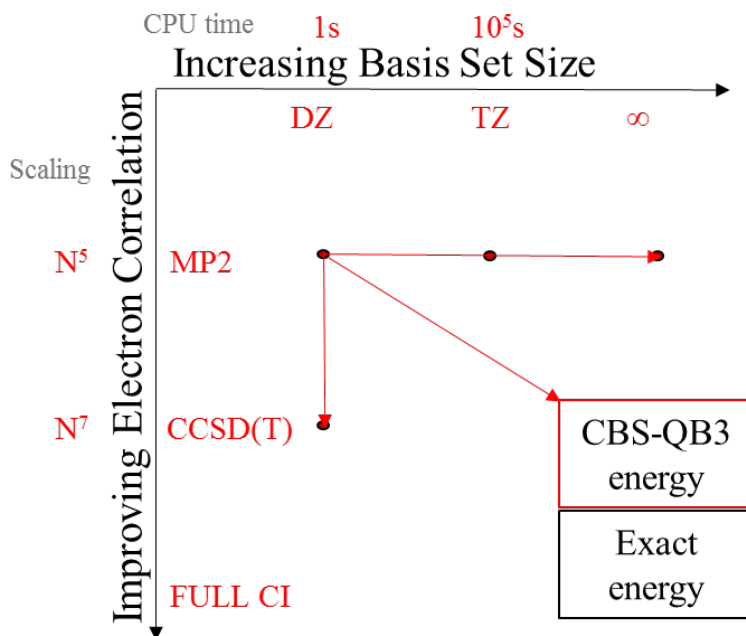


Figure 11. Graphic representation of CBS-QB3 quantum methods. CBS-QB3 composite methods have shown accuracy within 1.1kcal/mol in comparison with Gaussian 2 (G2) test set.

By utilizing CBS-QB3 calculations, the mechanisms, transition states, and respective products should have been verified for the 260 m/z pathway, allowing for a precise analysis of the G1 nitrile-terminated PPI dendrimer. The resulting CBS-QB3 energy surface is shown in Figure 12. All dissociation channel transition states involve an internal nucleophilic attack on a carbon adjacent to the positively charged nitrogen. All non-dissociative reaction channels involve either a hydride-shift or proton-transfer mechanism resulting in a complex network of double bond migrations. Interestingly, the reaction barriers leading to the formation of the pyrrolidinium – low abundance in mass spectra with m/z of 139 and 178 – moieties are lower than those for the pyrrolinium – high abundance in mass spectra with m/z 137 and 176 – ions.

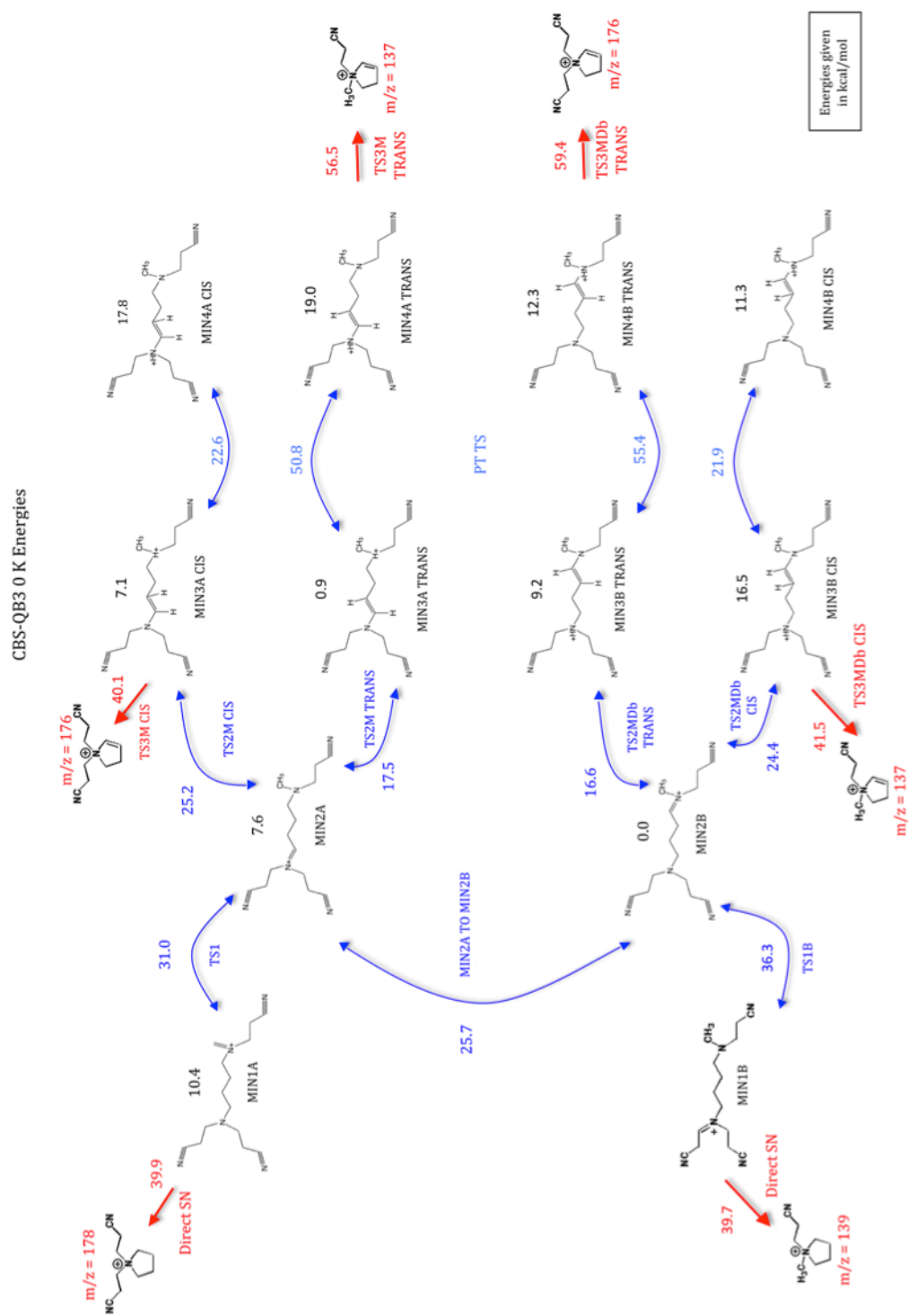


Figure 12. CBS-QB3 energy surface for the gas-phase dissociation pathways of the 260 m/z ion.

Transition states marked in blue. Six dissociation channels in red yield four products.

## DATA INCONSISTENCIES AND RESEARCH METHODS

Clearly, the results obtained from these computational methods indicated a discrepancy between theoretical calculations and experimental CID-ESI-MS data. Theoretically, the energetically favored pyrrolidinium fragments at 178 and 139 m/z should have higher, or at least competing, relative abundances in the CID-ESI-MS spectra. However, as observed in Figure 9B, the pyrrolidinium ions are small fractions when compared to the pyrrolinium ions of 176 and 137 m/z. In order to address such inconsistencies, further research consisted of two areas: synthesis of isotopically labeled PPI dendrimers and subsequent kinetic experiments with CID-MS at varying activation times (between 3 ms and 3000 ms) with corresponding collision energies. For the latter, the hypothesis was that the kinetic window formerly used allowed for too much random sampling, creating these misleading state populations. Hypothetically, in order to see experimental results more cohesive with theoretical results, the kinetic window must be expanded to allow less of the low energy double bond migrations to occur that would lead to the pyrrolinium ions. However, upon varying the kinetic window, it was determined that the 260 m/z ion was impervious to sampling in the range of kinetic windows available within this technique.

To unambiguously assign these fragments and the formation mechanisms, isotopic labeling is utilized. Due to the extensive branching of these systems, the dissociation studies result in fragmentation products of mass-to-charge ratios that can be assigned to multiple possible isomers formed by potentially competing mechanisms. CID mass spectra of dendrimer complexes with strategically labeled isotopes are compared to systems containing a natural abundance of isotopes to determine which atoms and functional groups are involved in the reaction, thus providing structural information. Supplemental results include the analysis of G1 nitrile-terminated PPI dendrimers complexed with alkali and alkaline earth metals.

## CHAPTER THREE

### EXPERIMENTAL

#### MATERIALS

Acrylonitrile, isopropanol, acetonitrile, methanol, and 2.4 M lithium aluminum hydride (LAH) in tetrahydrofuran (THF) were purchased from Acros Organics. Lithium aluminum deuteride (LAD), putrescine, succinamide, and d<sub>4</sub>-succinonitrile were purchased from Sigma Aldrich. Diethyl ether, acetic acid, formaldehyde, and potassium acetate were purchased from Fisher Scientific. Sodium acetate was purchased from Mallinckrodt. Magnesium hydroxide was purchased from Columbus Chemicals Industries. Calcium acetate was purchased from Matheson Coleman and Bell (MCB). All CID-ESI-MS experiments were performed with the ThermoFinnigan LCQ Ion-Trap Mass Spectrometer and analyzed with Xcalibur software.

#### METHODS

##### **Synthesis of 1<sup>st</sup> Generation Nitrile-terminated PPI Dendrimer**

In order to synthesize the G1 nitrile-terminated PPI dendrimer, a small-scale modified procedure of van der Wal et al is followed.<sup>31</sup> The reaction begins with 1,4-diaminobutane, commonly known as putrescine, and continues with a four to one Michael addition with acrylonitrile in a distilled water environment. Synthesis starts with 0.10 mL of 1,4-diaminobutane in a 10 mL round bottom flask equipped with a spin vane. Then, 1.0 mL of distilled H<sub>2</sub>O is added to the reaction flask, along with 0.50 mL of acrylonitrile, which is over a four to one molar ratio of acrylonitrile to 1,4-diaminobutane. Upon combination, two initial layers form – a bottom aqueous layer and top organic layer. While stirring, the reaction flask is heated in a hot water bath of 80°C for one hour. The mixture is then left to cool and stir

overnight. After one night, the mixture is still in two layers – the top, transparent yellow layer with the dendrimer and the bottom, cloudy colorless layer. This reaction is depicted in Figure 13.

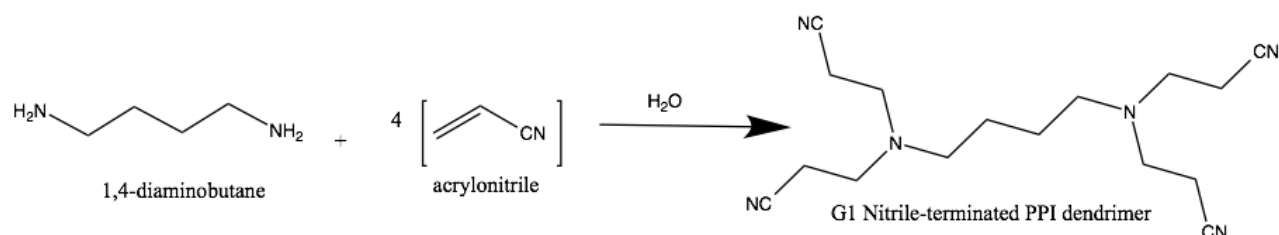


Figure 13. Michael addition reaction between 1,4-diaminobutane with acrylonitrile in distilled water solvent to give the G1 nitrile-terminated PPI dendrimer.

### Synthesis of Isotopically Labeled Dendrimer Cores

In order to unambiguously assign peaks in the mass spectrum, isotopically-labeled dendrimers are subjected to collision-induced dissociation. Isotopically-labeled dendrimers are synthesized by specifically placed deuterium on the 1,4-diaminobutane core. Deuterium atoms are located on the  $\alpha$ -carbons – the carbons adjacent to the terminal amine groups – or  $\beta$  carbons – the carbons furthest from the terminal amine groups.

In order to synthesize the  $\alpha$ -labeled core, the reaction begins with succinamide. In a 10 mL round bottom flask, 0.10 grams of succinamide and 0.20 grams of lithium aluminum deuteride (LiAlD<sub>4</sub> or LAD) are placed with a stir bar. A rubber septum is placed on top of the flask and the flask is purged with N<sub>2</sub> gas throughout the whole reduction reaction. Reaction vessel is suspended in an ice/acetone bath on a stir plate. Dropwise, about 5.0 mL of THF is added with a glass syringe to the succinamide with violent reaction. Once all of the THF is added, remove syringe and continue stirring. To make sure there is excess LAD, add one drop of water – noticeable reaction shows there is excess LAD, or all succinamide is reacted. System is

closed and left to stir overnight. After leaving the reaction to stir, product is quenched with about 7 mL of isopropanol to remove excess LAD. Once all LAD is quenched, product is vacuum filtered, rinsing with diethyl ether. The product filtrate is streamed with nitrogen gas to evaporate most of the ether, leaving the  $\alpha$ -d<sub>4</sub>-1,4-diaminobutane. The reaction is displayed in Figure 14.

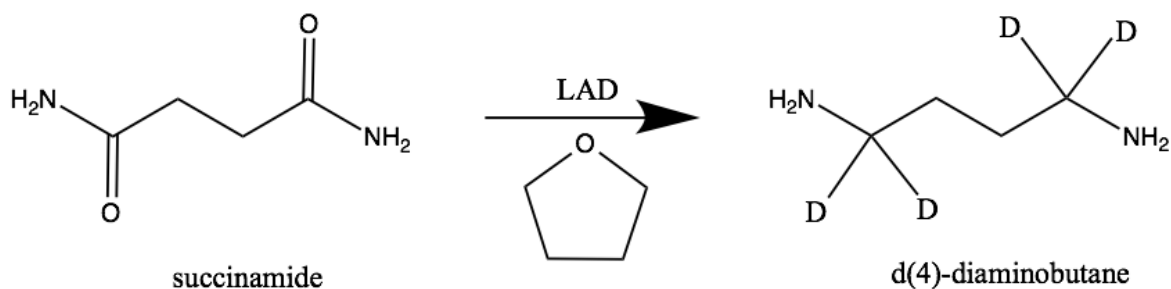


Figure 14. Reduction reaction of succinamide with LiAlD<sub>4</sub> in THF to give  $\alpha$ -labeled core.

The synthesis for the  $\beta$ -labeled core is similar, except the reaction begins with an isotopically labeled molecule – d<sub>4</sub>-succinonitrile. In a 50 mL pear shaped flask with sideneck joint, 0.35 grams d<sub>4</sub>-succinonitrile is added along with a spin vane. The main neck joint is equipped with a 50 mL cylindrical addition funnel with stopcock for gradual addition of reducing agent. Nitrogen gas is streamed into the system through a rubber septum on the sideneck joint, and a rubber septum closes off the top joint of the addition funnel as well. The entire system is also suspended in an ice/acetone bath. Excess dry THF is also used to solvate the d<sub>4</sub>-succinonitrile. With a glass syringe, 3-4 mL of dry tetrahydrofuran (THF) is added to solvate the succinamide, as well as to allow the reaction to remain stirring during the entire reaction. The reaction uses lithium aluminum hydride (LiAlH<sub>4</sub> or LAH) as a reducing agent. About 5.0 mL of 2.4 M LAH in THF is drawn up in a glass syringe and added into the addition funnel with stopcock closed. LAH/THF solution is also added dropwise, presenting a very violent reaction. If



reaction becomes too solid, excess THF is added to the vessel. To make sure there is excess LAH, add one drop of water – noticeable reaction shows all  $d_4$ -succinonitrile is reacted. The reaction is then left to stir overnight. The next day, reaction is quenched with about 8.0 mL of isopropanol, vacuum filtered, and rinsed with diethyl ether. Excess ether in product filtrate is evaporated off with nitrogen stream. The remaining oily liquid is the  $\beta$ - $d_4$ -1,4-diaminobutane. The reaction is presented in Figure 15.

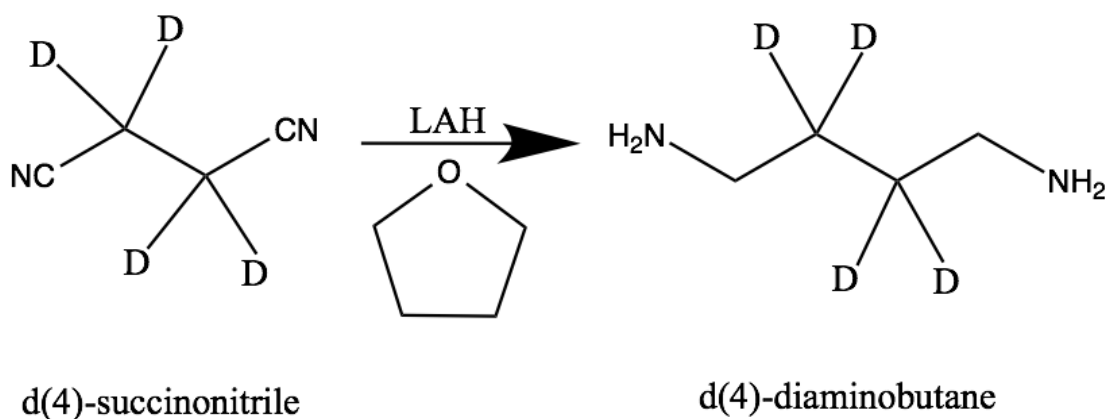


Figure 15. Reduction reaction of  $d_4$ -succinonitrile with  $LiAlH_4$  in THF to give  $\beta$ -labeled core.

### Synthesis of Isotopically Labeled G1 Nitrile-Terminated PPI Dendrimer

To synthesize both the  $\alpha$ - and  $\beta$ -labeled first generation dendrimers, the same procedure for the G1 nitrile-terminated PPI dendrimer is followed with a Michael addition reaction with four to one ratio of acrylonitrile to the  $\alpha$ - $d_4$ -diaminobutane or  $\beta$ - $d_4$ -diaminobutane in water. The  $\alpha$ - and  $\beta$ -labeled Michael reactions are displayed in Figure 16 and Figure 17, respectively.

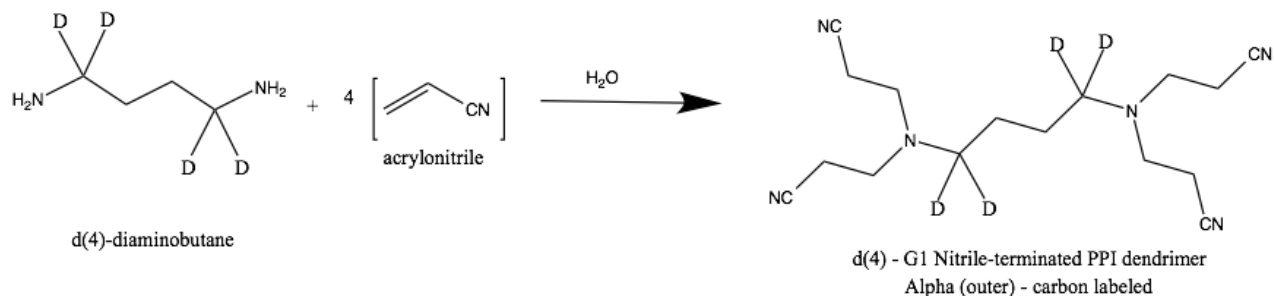


Figure 16. Michael addition reaction with  $\alpha$ -d<sub>4</sub>-diaminobutane and acrylonitrile in distilled water solvent to give isotopically labeled G1 nitrile-terminated PPI dendrimer.

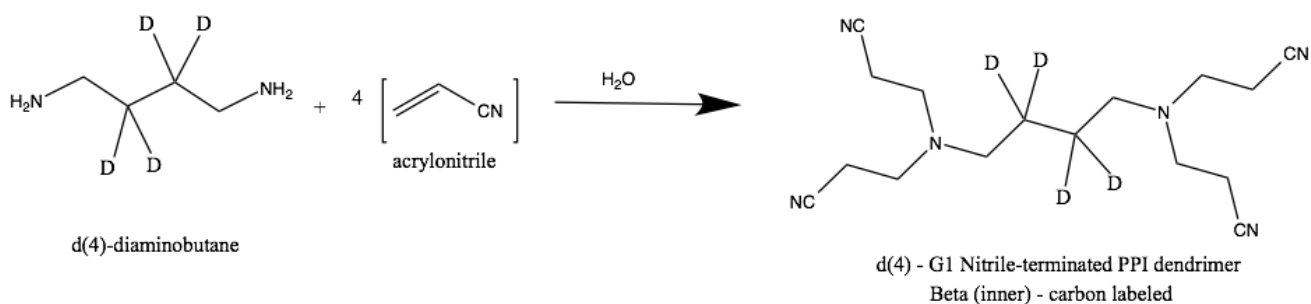


Figure 17. Michael addition reaction with  $\beta$ -d<sub>4</sub>-diaminobutane and acrylonitrile in distilled water solvent to give isotopically labeled G1 nitrile-terminated PPI dendrimer.

### Synthesis of 260 m/z structure

To verify the starting structure for the MS<sup>3</sup> fragmentation pathway, it is valuable to directly synthesize the hypothesized structure for the 260 m/z daughter ion and perform MS<sup>2</sup> collision-induced dissociation. Fragmentation patterns are compared for confirmation of initial structure. Synthesizing the structure that corresponds to the 260 m/z daughter ion begins much like the synthesis of the G1 nitrile-terminated dendrimer. However, instead of using four times the molar amount of acrylonitrile, only about two times the molar amount of acrylonitrile is used; here, the aim is to only add acrylonitrile to three out of the four available nitrogen bonds.

The synthesis normally begins with about 0.10 mL of 1,4-diaminobutane. The 1,4-diaminobutane is placed in a 10 mL round bottom flask with about 1.0 mL of distilled water. Approximately 0.15 mL of acrylonitrile is added and solution is left to stir at 80°C for one hour. At this point in the reaction, excess formaldehyde – about 0.50 mL – and one drop of methanol is added. The formaldehyde allows for amine addition to the carbonyl, followed by loss of water. The remaining product should be the 1,4-diaminobutane core with three arms and an imine. The reaction is shown in Figure 18.

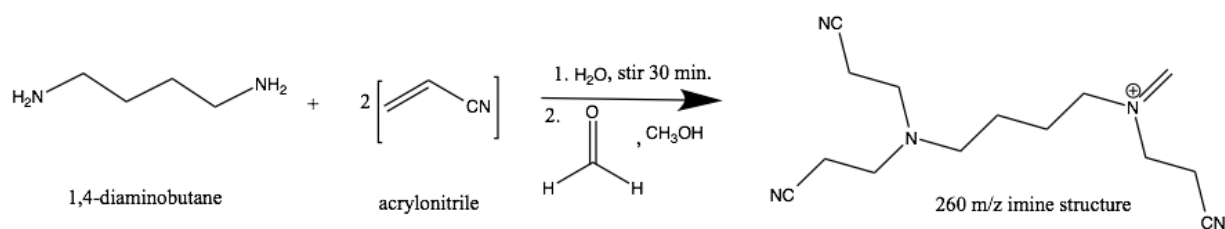


Figure 18. Michael reaction with 1,4-diaminobutane and acrylonitrile in a distilled water solvent, followed by imine formation with excess formaldehyde and methanol to yield 260 m/z product.

To form the structure corresponding to the 264 m/z daughter ion, or the 260 m/z structure with either  $\alpha$ - or  $\beta$ -labeled carbons, synthesis procedure follows along identical to that of the 260 m/z. Beginning with desired isotopically labeled core, a Michael addition reaction with about two times the molar ratio of acrylonitrile in a distilled water solvent is initiated. Reaction is left to stir for about 30 minutes. Then excess amount of formaldehyde and one drop of methanol is added. These reactions are displayed in Figure 19 and Figure 20.

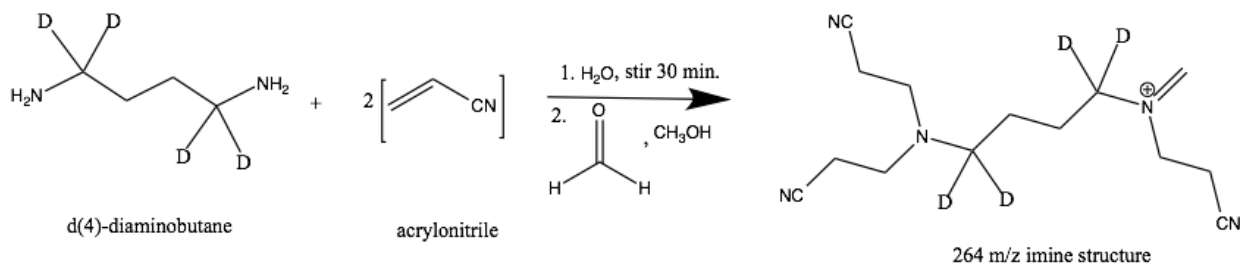


Figure 19. Michael reaction with  $\alpha$ -d<sub>4</sub>-diaminobutane and acrylonitrile in a distilled water solvent, followed by imine formation with excess formaldehyde and methanol to yield 264 m/z product.

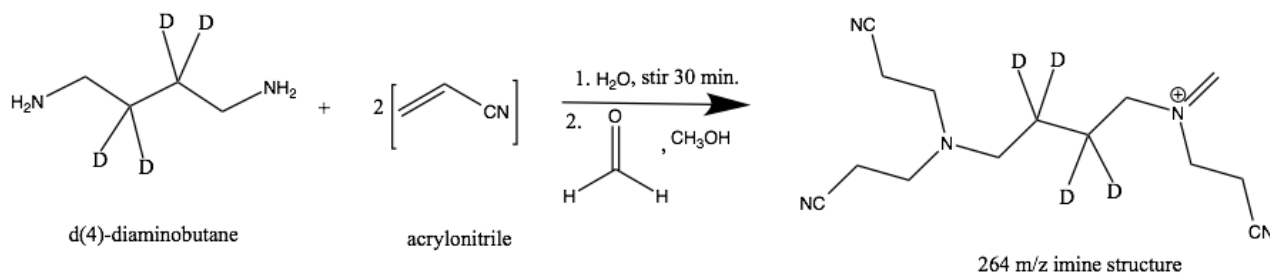


Figure 20. Michael reaction with  $\beta$ -d<sub>4</sub>-diaminobutane and acrylonitrile in a distilled water solvent, followed by imine formation with excess formaldehyde and methanol to yield 264 m/z product.

### Alkali and Alkaline Earth Metal Solutions

Adding 0.15 grams of  $\text{CH}_3\text{COONa} \cdot 3\text{H}_2\text{O}$  to 10 mL of distilled water creates a 0.1M sodium acetate solution. Adding 0.21 grams of  $\text{MgCl}_2 \cdot 6\text{H}_2\text{O}$  to 10 mL of distilled water creates a 0.1 M magnesium chloride solution. Adding 0.10 grams of  $\text{CH}_3\text{COOK}$  to 10 mL of distilled water forms a 0.1 M potassium acetate solution. Finally, adding 0.18 grams of  $\text{Ca}(\text{COOCH}_3)_2 \cdot \text{H}_2\text{O}$  to 10 mL of distilled water forms a 0.1 M calcium acetate solution.

## Mass Spectrometry

Samples used for electrospray are created by combining approximately 0.10 mL of concentrated sample, 1.4 mL of a 1:1 mixture of acetonitrile and distilled water, and one drop of acetic acid. For the 260 m/z and 260 m/z directly synthesized samples, a 1:1 mixture of methanol and distilled water is used instead. Alkali and alkaline earth metal solutions are combined in a 1:1 ratio with the dendrimer samples and acetic acid is not added. Approximately 0.50 mL of the sample is drawn into syringe for automatic dispensing into the mass spectrometer by way of syringe pump. Sample is introduced into the system at a flow rate of 6  $\mu\text{L}/\text{min}$  with a source voltage normally kept around 4.1 kV. Data was collected and taken over a period of 100 total scans to be averaged. Activation amplitude and time varied, depending on the purpose, but normal activation time of 30 ms with corresponding activation amplitude was most commonly used.

## CHAPTER FOUR

### RESULTS AND DISCUSSION

#### ISOTOPICALLY LABELED DENDRIMERS

After synthesis of isotopically labeled species, fragmentation studies are performed. By labeling  $\alpha$ - &  $\beta$ -carbons in the nitrile-terminated PPI dendrimers, the movement of protons about the energy surface is unambiguously determined. Daughter ions differing in mass-to-charge ratio are produced depending on the location of deuterium atoms.

#### **Hypothesized Isotopic Structures**

The hypothesized gas-phase fragmentation mechanisms and resulting daughter ion products are outlined in Figure 21 and Figure 22. The movement of  $\alpha$ -deuterium (in red) is followed to yield corresponding daughter ions, referred to as deuterated outer carbon structures, or DOC. The movement of  $\beta$ -deuterium (in blue) is seen to yield the corresponding daughter ions, referred to as deuterated inner carbon structures, or DIC. By comparing the physical CID-ESI-MS results for the hypothesized isotopically labeled dendrimer fragments, appropriate mechanisms and structures are verified or rejected.

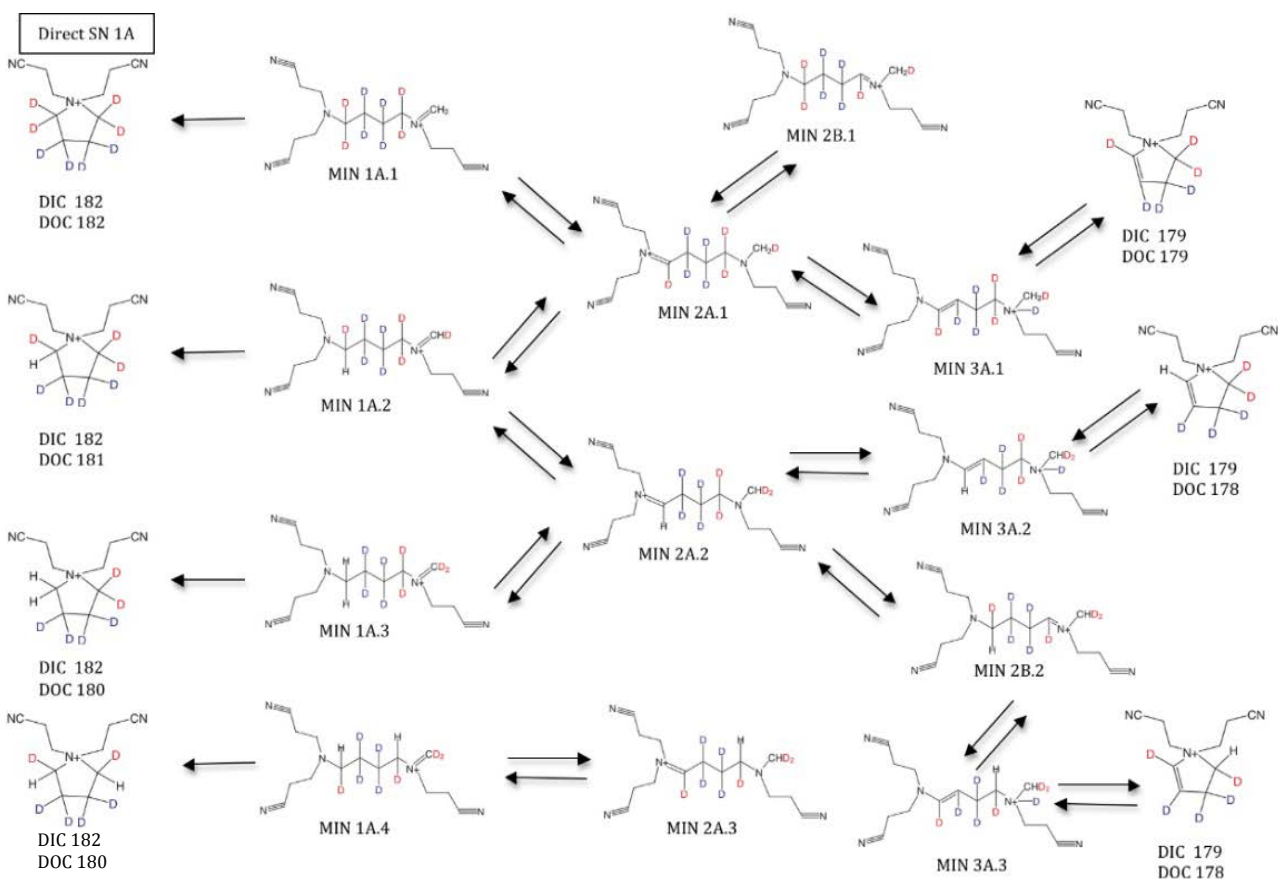


Figure 21. Hypothesized isotopic structures near the 180  $m/z$  range. Pathways demonstrate many double bond migrations and deuteride shifts, as in the CBS-QB3 energy surface.

Figure 21 begins with the MIN 1A structure, which is the starting point for the 260  $m/z$   $MS^3$  pathway. The three other MIN 1A structures – 1A.2, 1A.3, and 1A.4 – are similar imine structures resulting from varying  $\alpha$ -deuteride shifts with MIN 2A transition state structures. Direct dissociation products resulting from internal nucleophilic substitution of MIN 1A structures could potentially yield four different structures. The DOC resulting structures could have fragments of 182, 181 and 180  $m/z$ . On the other hand, the DIC resulting structure should only reveal a direct dissociation product of 182  $m/z$ , with all deuterium atoms on initial  $\beta$ -carbons. It is important to note that these structures correspond to the saturated ring structure of 178  $m/z$  in the energy surface in Figure 12.

After  $\alpha$ -deuteride shifts occur in MIN 1A structures to give MIN 2A transition state structures, the nucleophilic nitrogen can attack a  $\beta$ -deuterium causing a double bond migration, giving an alternative to direct dissociation. The transitions consequential of these double bond migrations are represented in the MIN 3A structures – 3A.1, 3A.2, and 3A.3. It is now the opposing nitrogen which is nucleophilic and will attack the furthest carbon to form a ringed structure with the loss of a secondary amine. The DOC species could produce structures of 179 m/z and 178 m/z by following this dissociation pathway. The DIC species, however, should once again only produce one value for a mass-to-charge ratio – 179 m/z. These structure directly correspond to the unsaturated ring structure of 176 m/z in the energy surface in Figure 12.

The connection between Figure 21 and Figure 22 are the two shared structures – MIN 2B.1 and MIN 2B.2 The MIN 2B structures are characterized by internal double bond to the nitrogen previously nucleophilic in the MIN 2A structures. The molecule can then follow a path giving way to a hydride shift from an arm hydrogen, yielding MIN 1A structures. Then subsequent nucleophilic substitution for neutral loss of a secondary aldimine results in the four possible saturated ring structures. The DOC resulting structures could have mass-to-charge ratios of 143 and 142 depending on the loss of a deuterium in the aldimine. Alternatively, the DIC resulting structures should only result in one mass-to-charge ratio of 143, since no  $\beta$ -deuterium move.



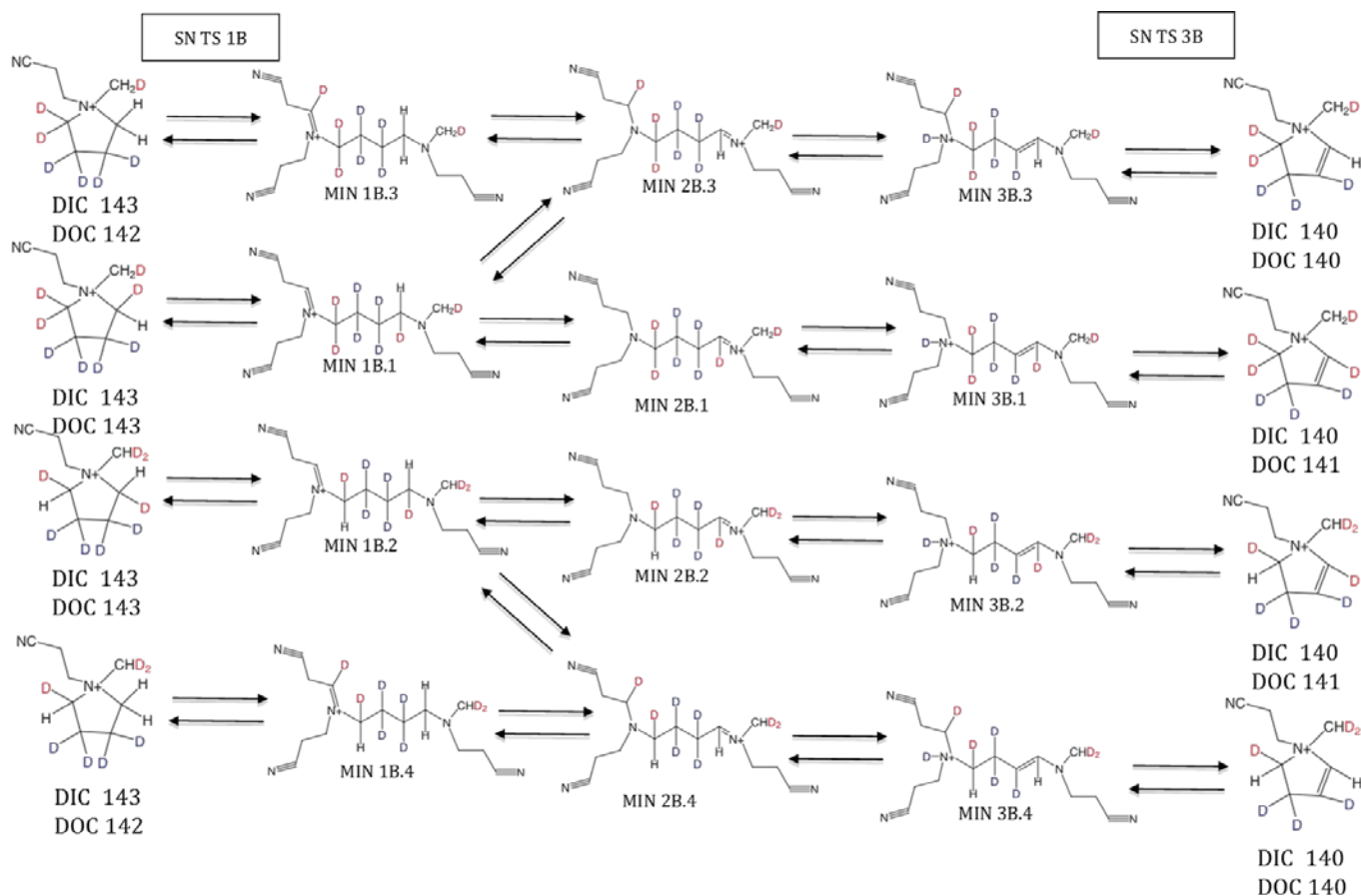


Figure 22. Hypothesized isotopic structures near the 140  $m/z$  range. Pathways demonstrate double bond migrations and deuteride shifts, as in the CBS-QB3 energy surface.

Otherwise, the MIN 2B structures could undergo double bond migration caused by nucleophilic attack of the nitrogen on the furthest  $\alpha$ -deuterium. This movement results in the MIN 3B transition state structures. Similar to the mechanism of MIN 3A structures, the MIN 3B structures can form the ring structures of varying mass-to-charge ratios resultant of the nucleophilic attack of the nitrogen and subsequent neutral loss of the primary amine. The DOC structure can result in mass-to-charge ratios of 141 and 140, while yet again, little movement should occur with the  $\beta$ -deuterium, leaving the DIC structure to have only one possible mass-to-charge ratio of 140.

## CID-ESI-MS Studies of DOC Structures

The first isotopically labeled species investigated was the DOC 1<sup>st</sup> generation nitrile-terminated PPI dendrimers. The initial CID-ESI-MS spectrum of parent ion 305 m/z is shown in Figure 23. The two fragmentation pathways of high population are 264 m/z and 182 m/z, each corresponding to the imine species of 260 m/z and ring structure of 178 m/z in the fragmentation of the non-isotopic nitrile-terminated PPI dendrimer.

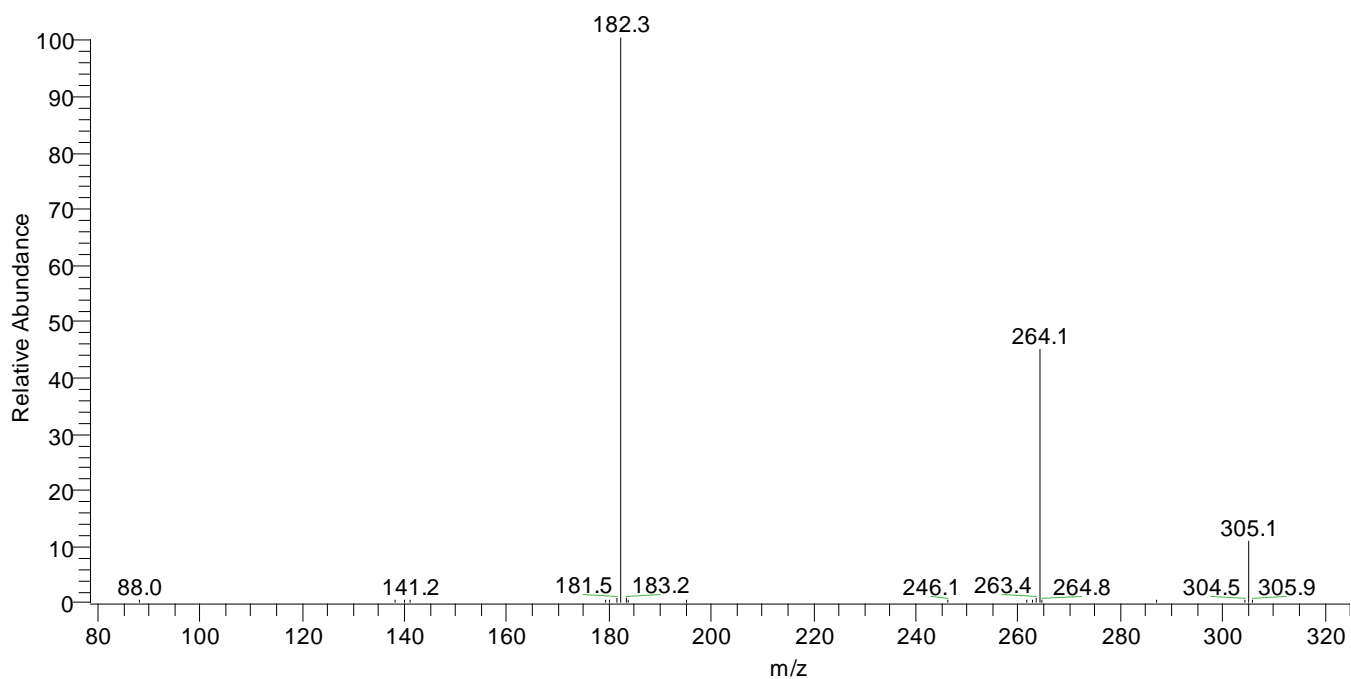


Figure 23. MS<sup>2</sup> of DOC 305 m/z synthesized dendrimer conducted at activation amplitude of 23% and normal activation time of 30 ms resulting in two fragmentation pathways of 264 m/z and 182 m/z.

At an attempt to follow hypothesis of varying kinetic window to change state populations, various activation times – 3000 ms, 300 ms, 6 ms, and 3 ms – were tested for the MS<sup>2</sup> pathway. The underlying aim was to increase the population of the 264 m/z for better resolution further down this fragmentation pathway. It was determined that the activation time of 3 ms completed this task fittingly, increasing the relative abundance by over 20%. The resulting spectrum with 3 ms activation time is presented in Figure 24.

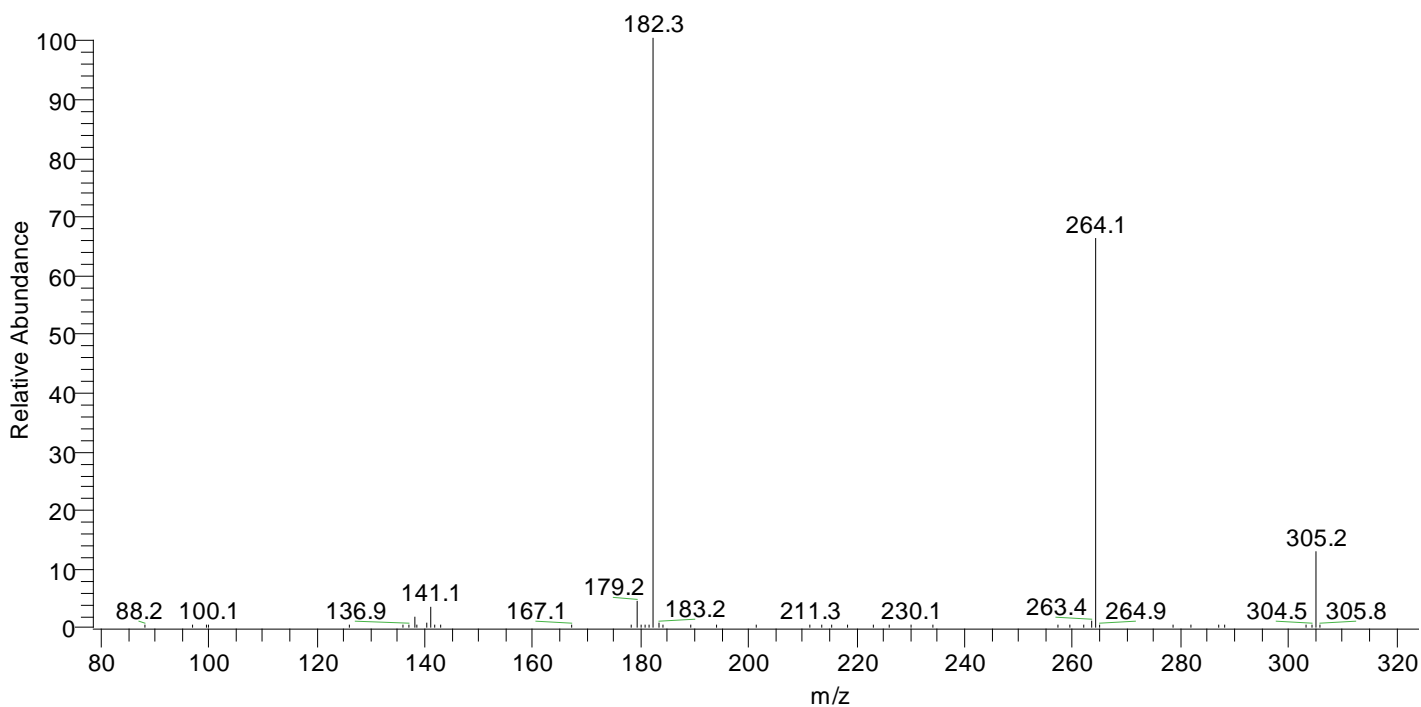


Figure 24. MS<sup>2</sup> of DOC 305 m/z synthesized dendrimer conducted at activation amplitude of 42% and faster activation time of 3 ms resulting in the same two fragmentation pathways, but larger relative abundance of 264 m/z in comparison to 30 ms kinetic window.

Utilizing the larger state population of the 264 m/z daughter ion, further CID-ESI-MS was performed on this ion. The resulting fragmentation is shown in Figure 25. Two fragmentation pathways of high relative abundances result at 179 m/z and 141 m/z. Compared to the hypothesized structures in Figure 21 and Figure 22, respectively, it can be assumed that these daughter ion peaks will correspond with the unsaturated ring structures. Further zoom scans were performed to see the presence of other hypothesized daughter ion mass-to-charge ratios.

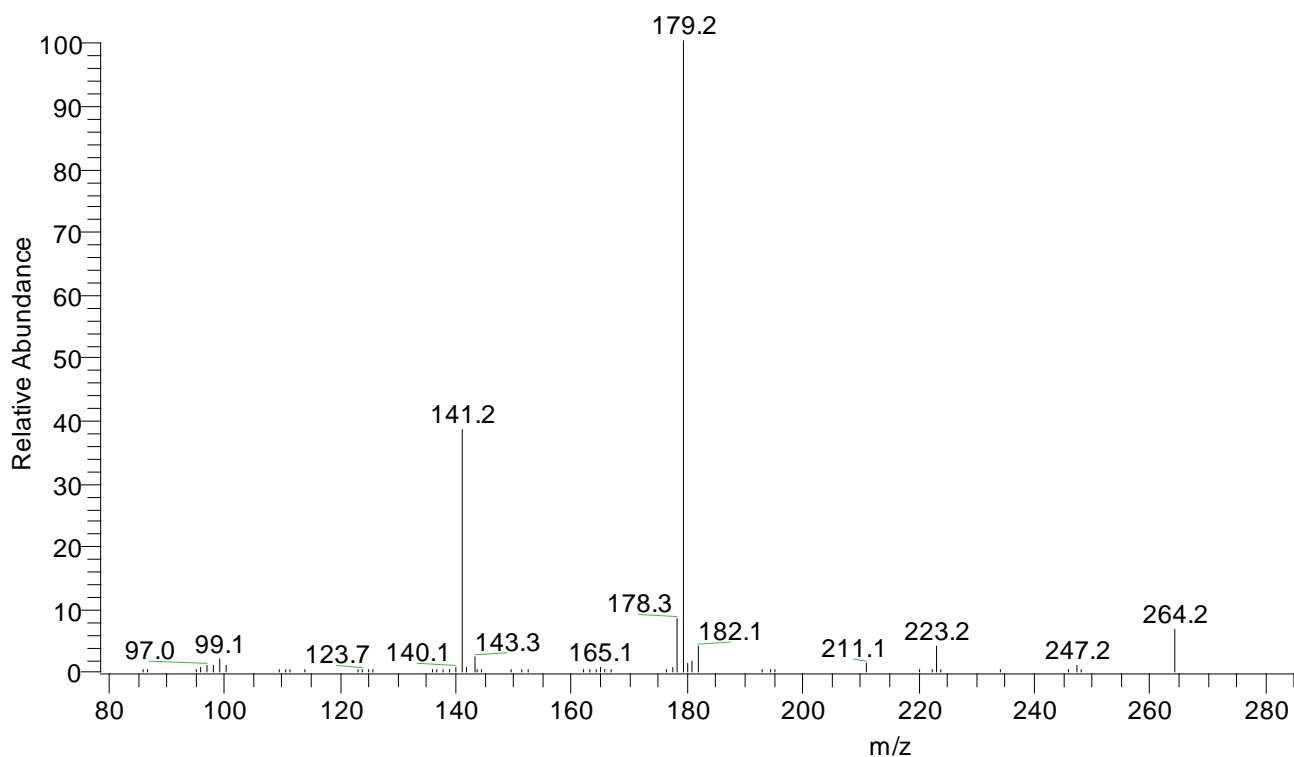


Figure 25. MS<sup>3</sup> of 264 m/z daughter ion at normal kinetic window of 30 ms yielding two fragmentation pathways of large relative abundances at 179 m/z and 141 m/z.

To verify starting 264 m/z structure, a parallel CID-ESI-MS study was performed on the directly synthesized 264 m/z structure. The resulting fragmentation pattern is shown in Figure 26 for comparison. It is clear that the two spectra in Figure 25 and Figure 26 have identical fragmentation patterns – therefore the MIN 1A structure is verified. The structures for the 305 m/z DOC dendrimer and 264 m/z DOC structure are displayed in Table 1.

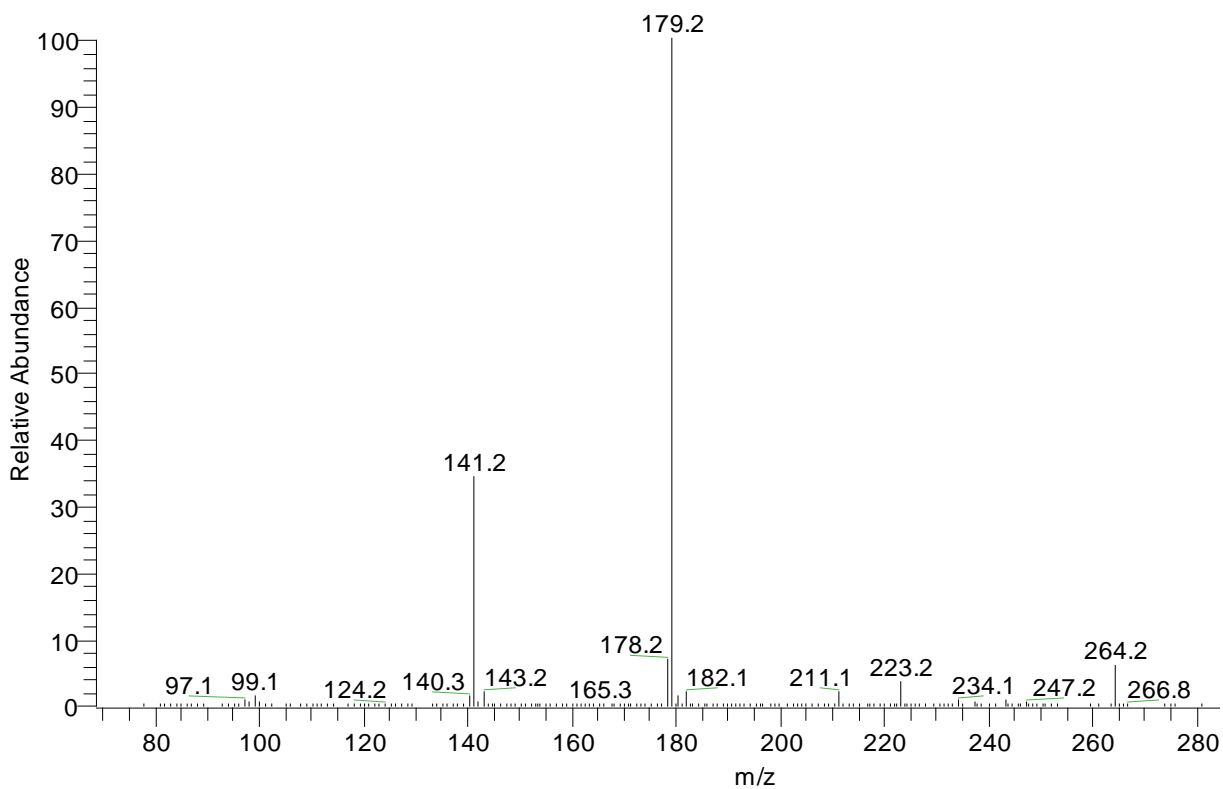


Figure 26. MS<sup>2</sup> of directly synthesized DOC 264 m/z species at activation amplitude of 28% and activation time of 30 ms yielding daughter ions at 179 m/z and 141 m/z.

m/z	305 m/z	264 m/z
Verified Structure		

Table 1. Verified structures for DOC 305 m/z G1 dendrimer and daughter ion of 264 m/z.

Zoom scans centered on each mass-to-charge ratio peak of high abundance in the DOC MS<sup>3</sup> spectrum were taken. The zoom scans correspond to the general range of mass-to-charge ratio seen in the hypothesized structures in Figure 21 and Figure 22. The MS<sup>3</sup> zoom scan centered around 179 m/z is presented in Figure 27. The well-defined leading daughter ion is that of the m/z 179. Two other mass-to-charge ratios stand out as structures with noticeable state population – 178 m/z and 182 m/z. However, the relative abundances still fall below 10% of the 179 m/z species. The 178 m/z structure also corresponds to two possible unsaturated ring structures, much like that of the 179 m/z species. Alternatively, the 182 m/z peak does correspond to a saturated ring structure; 182 m/z is the product of direct nucleophilic substitution immediately fragmenting from the 264 m/z. This further reinforces the CID-ESI-MS of the original 260 m/z yielding highly populated unsaturated ring structure over saturated ring structure coming from direct dissociation.

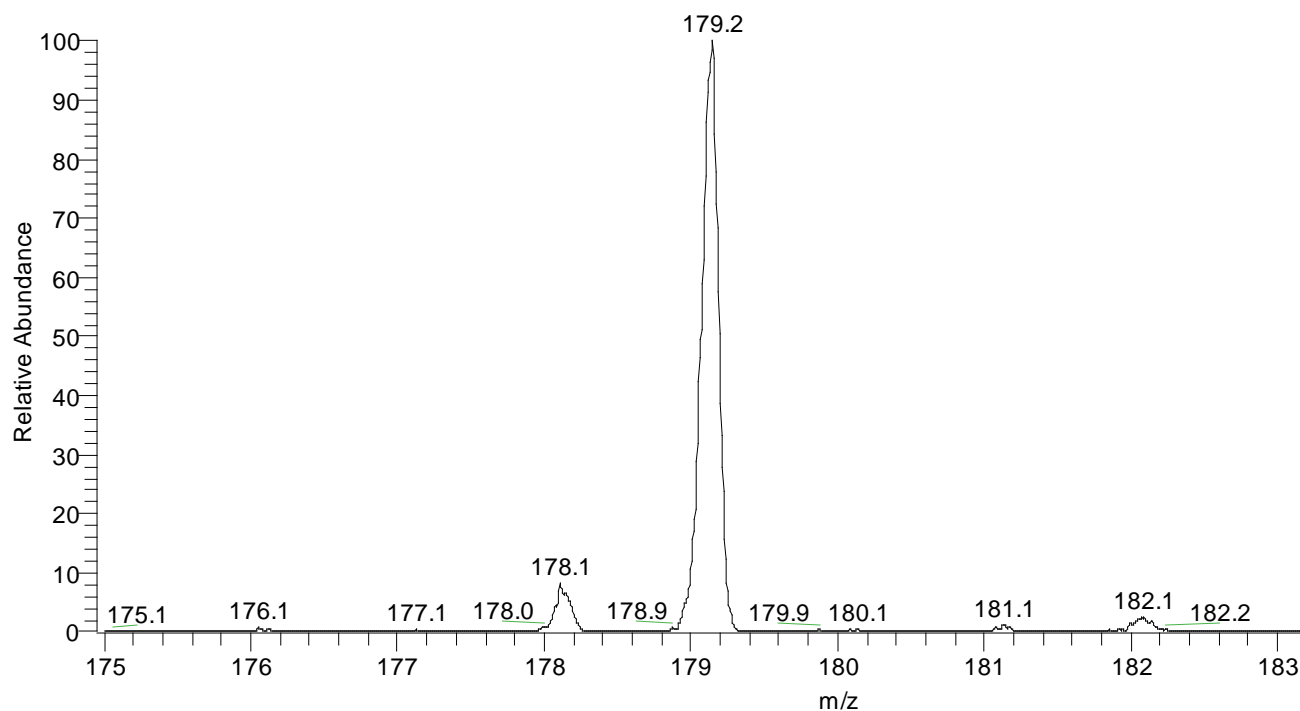


Figure 27. Zoom scan around 179 m/z for the DOC MS<sup>3</sup> spectrum.

It is also evident from the zoom spectrum that very little isotopic scrambling occurs, even for larger kinetic windows. The same abundances were resultant for zoom scans at 3000 ms. The 179 m/z and 182 m/z can only result from a combination of one deuteride shift and double bond migration or direct dissociation, respectively. The low abundances for 181 m/z, 180 m/z, and 178 m/z in comparison with their respective higher abundance structures suggest only minor deviation from the more direct mechanisms to other transition states that arise from further deuteride shifting and double bond migration. Also evident through this zoom scan is the location and movement of hydrides during fragmentation. The favored mechanisms for the DOC 264 m/z structure are shown in Figure 28.

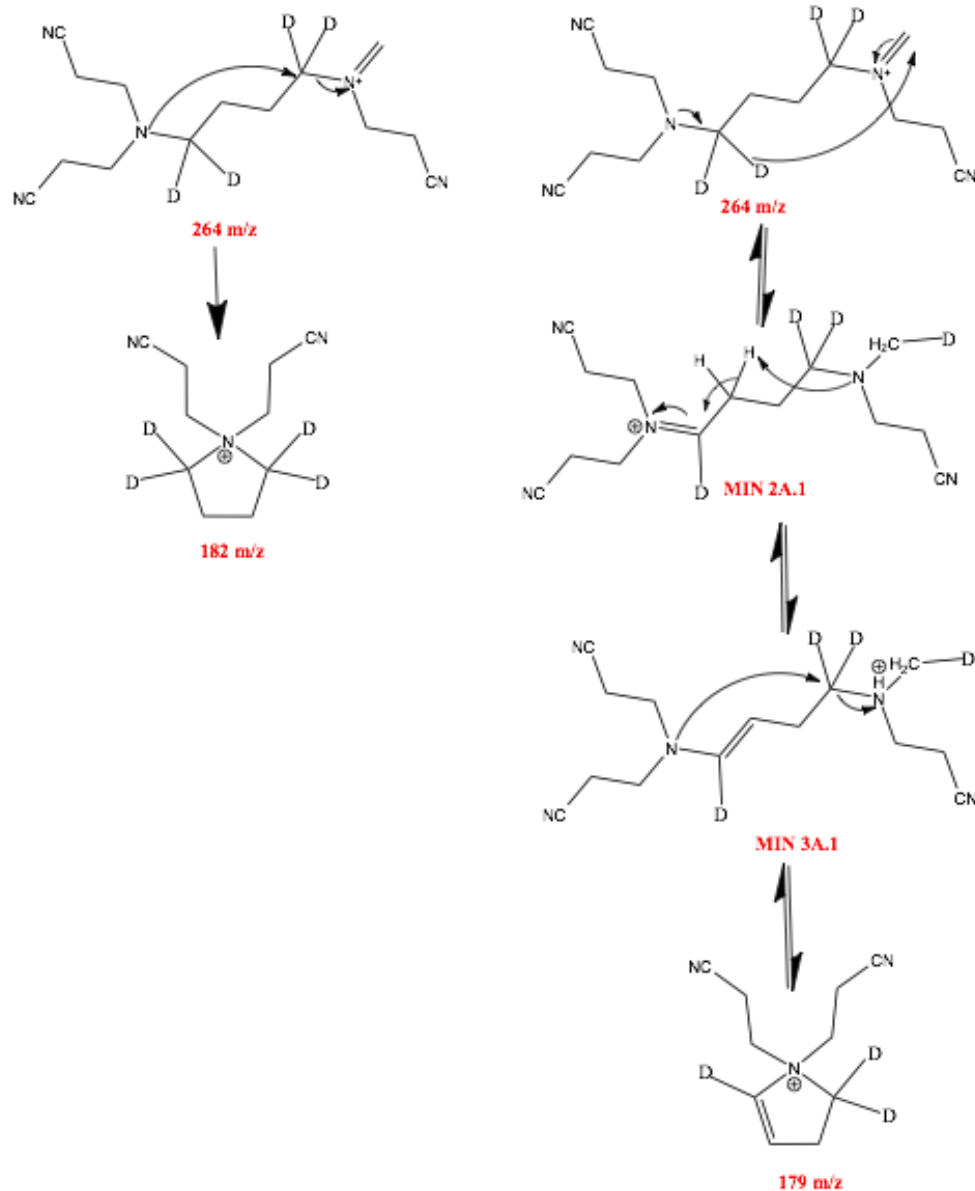


Figure 28. Favored mechanisms for DOC MIN 1A.1 264 m/z structure yielding predominately 179 m/z with MIN 2A.1 and MIN 3A.1 transition states and only slight population of saturated ring structure of 182 m/z from direct nucleophilic substitution.

The zoom scan around the 141 m/z peak seen with high state population in the MS<sup>3</sup> is shown in Figure 29. Clearly 141 m/z surpasses the relative abundance of all other possible structures with 94% higher population than the next closest peak at 143 m/z. Peaks at 143 m/z



and 140 m/z have the next highest state population. By comparing this zoom scan to the hypothesized structures in Figure 22, it is once again evident that little deviation from the most direct pathways occurs. The structures around this m/z range originate from the 260 m/z MIN 1A.1 structure through the subsequent transitions leading to the MIN 2B.1 and MIN 2B.2 transition state structures. It is from these two structures that a hydride shift can lead to direct nucleophilic substitution producing the possible 143 m/z structures, or nucleophilic attack of a nitrogen on a  $\beta$ -carbon hydrogen with subsequent double bond migration and ring formation to yield the 141 m/z structure. Interesting enough, the presence of 140 m/z suggests some deviation from direct pathways, as the channel it follows is quite convoluted in comparison.

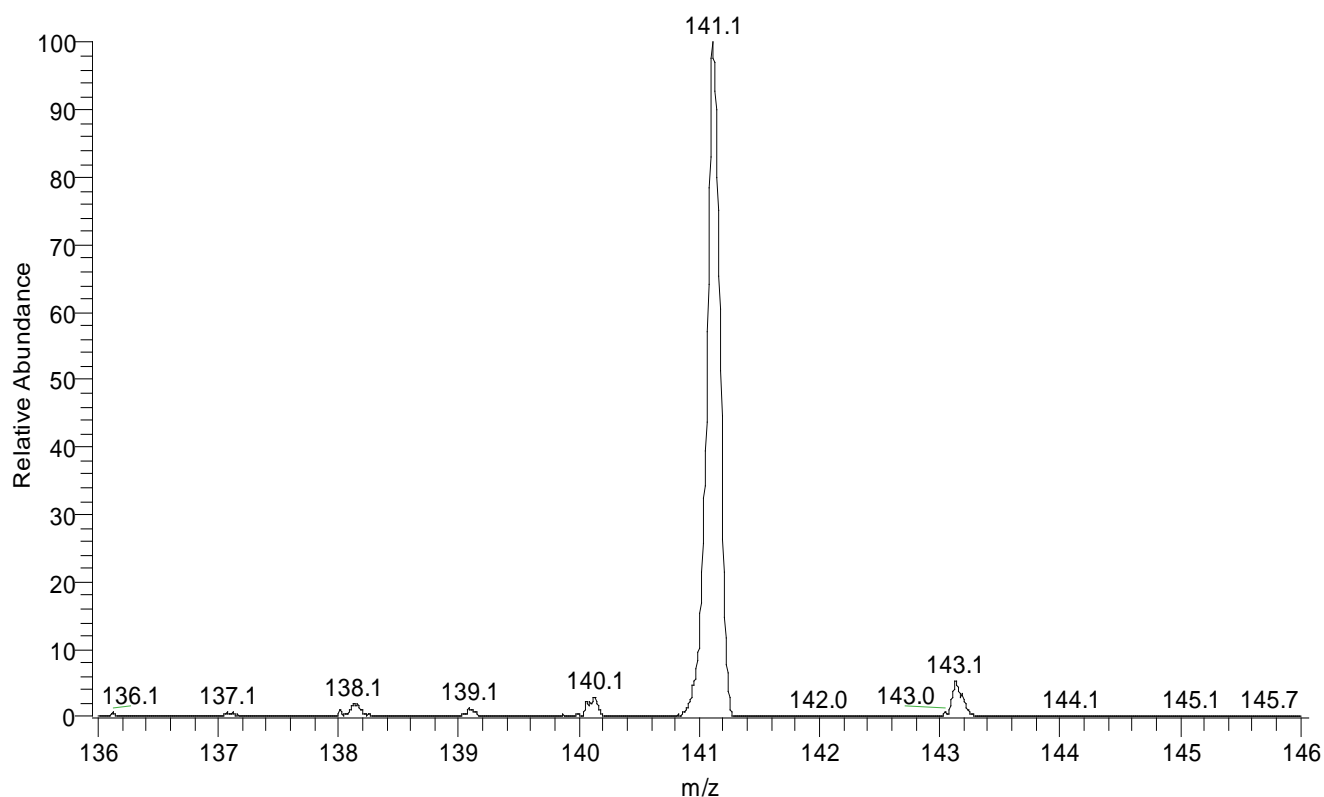


Figure 29. Zoom scan around 141 m/z for the DOC MS<sup>3</sup> spectrum.

The favored mechanisms indicated by the zoom spectrum around 141 m/z are indicated in Figure 30. In the first indicated mechanisms for the 179 m/z range, it is suggested that the

primary transition states appear to be the MIN 2A.1 and MIN 3A.1 transition state structures specified by the higher relative abundances of certain mass-to-charge ratios. Therefore, the only mechanisms that will be presented are those originating from the MIN 2B.1 transition state structure.

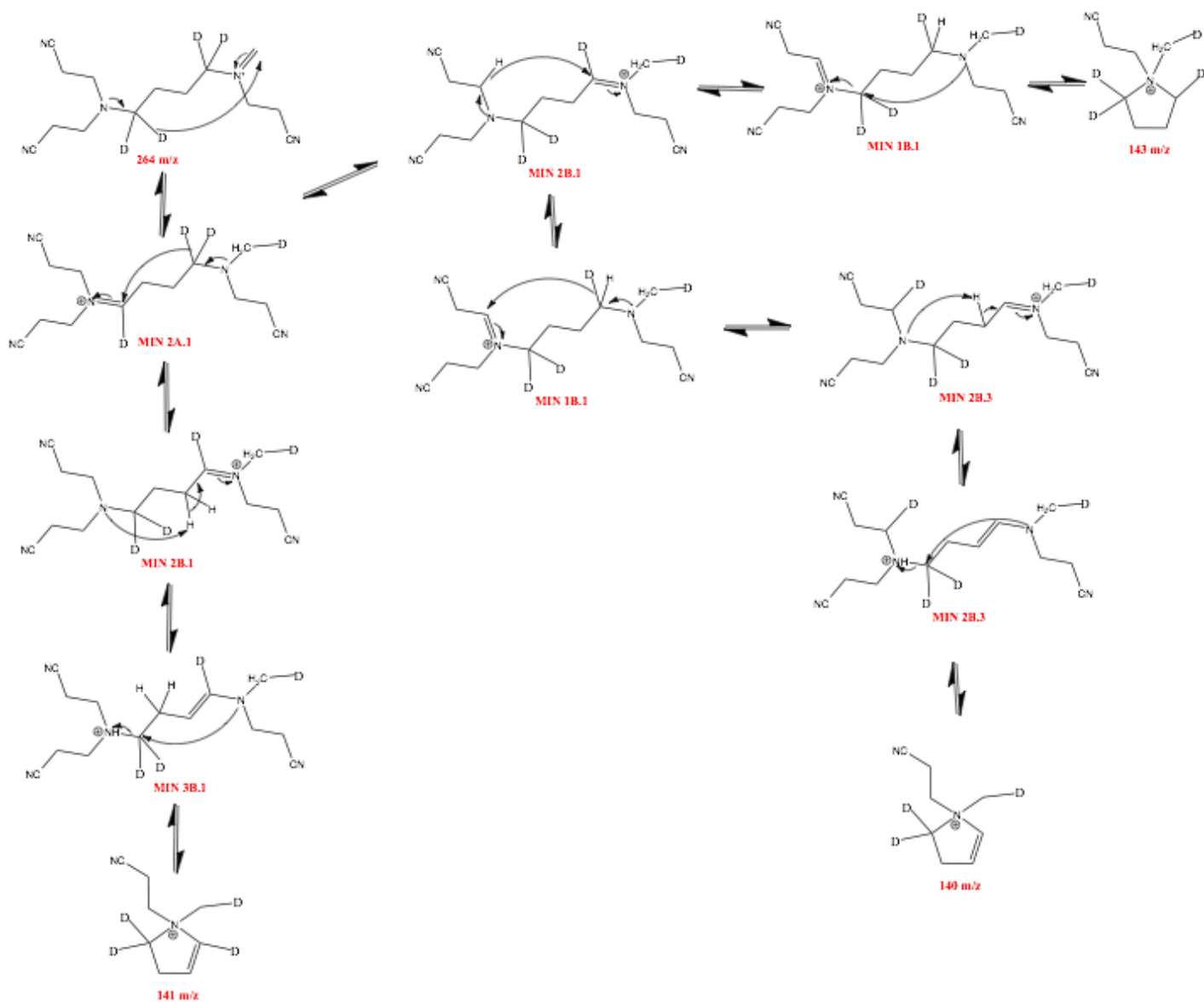


Figure 30. Favored mechanism for formation of highly populated 141 m/z unsaturated ring structure from the MIN 1A.1 264 m/z, as well as 140 m/z and 143 m/z ring structures.

## CID-ESI-MS Studies of DIC Structures

By examining the possible structures for the hypothesized transition states and resulting fragments for the DIC structures, it is apparent that variation of  $m/z$  is not as prominent when compared to the varying  $m/z$  of the DOC structures. The lack of changing  $m/z$  values stems from the hypothesis that most of the mechanisms involve movement of  $\alpha$ -hydrogens. Investigating these structures, however, will still verify or reject the mechanisms set in place by DOC structures. The resulting CID-ESI-MS spectrum from the DIC 305  $m/z$  parent ion is presented in Figure 31.

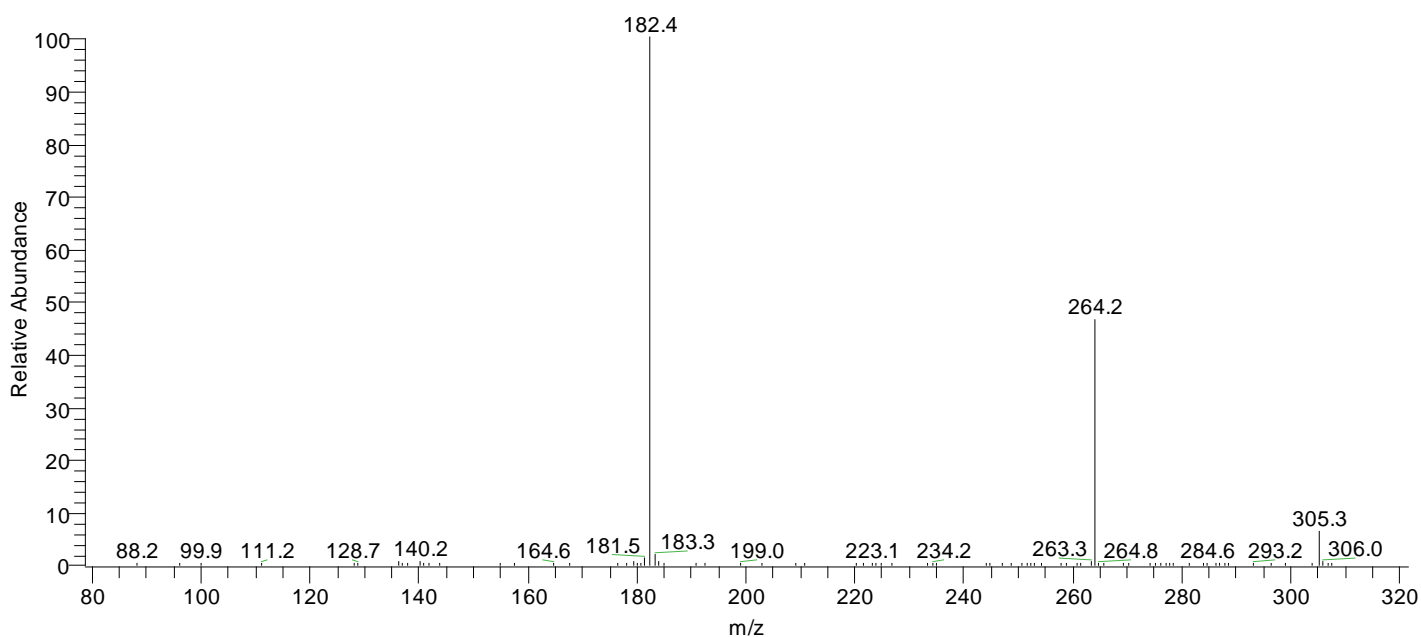


Figure 31.  $MS^2$  of DIC 305  $m/z$  synthesized dendrimer conducted at activation amplitude of 17% and normal activation time of 30 ms resulting in two fragmentation pathways of 264  $m/z$  and 182  $m/z$ .

The MS<sup>2</sup> fragmentation for the DIC presents the same daughter ions as the DOC. This suggests that the 264 m/z is, in fact, the same starting structure as the structure which was verified for the DOC dendrimer. The true structures for the DIC 305 m/z and 264 m/z are displayed in Table 2.

m/z	305 m/z	264 m/z
Verified Structure		

Table 2. Verified structures for DIC 305 m/z G1 dendrimer and daughter ion of 264 m/z.

Again, the strategy of changing the kinetic window to allow for a higher abundance of the 264 m/z pathway was employed. Since smaller kinetic windows yielded higher relative abundance, times were only varied at windows smaller than the standard 30 ms activation time. The 3 ms activation time proved to be too small for the DIC dendrimer for reasons unknown. However, activation times of 6 ms and 4 ms resulted in appropriate spectra. It was determined that 4 ms yielded the best relative abundance for the 264 m/z fragment; the spectrum is presented in Figure 32 showing, again, a growth in state population of approximately 20% when compared to the 30 ms spectrum.

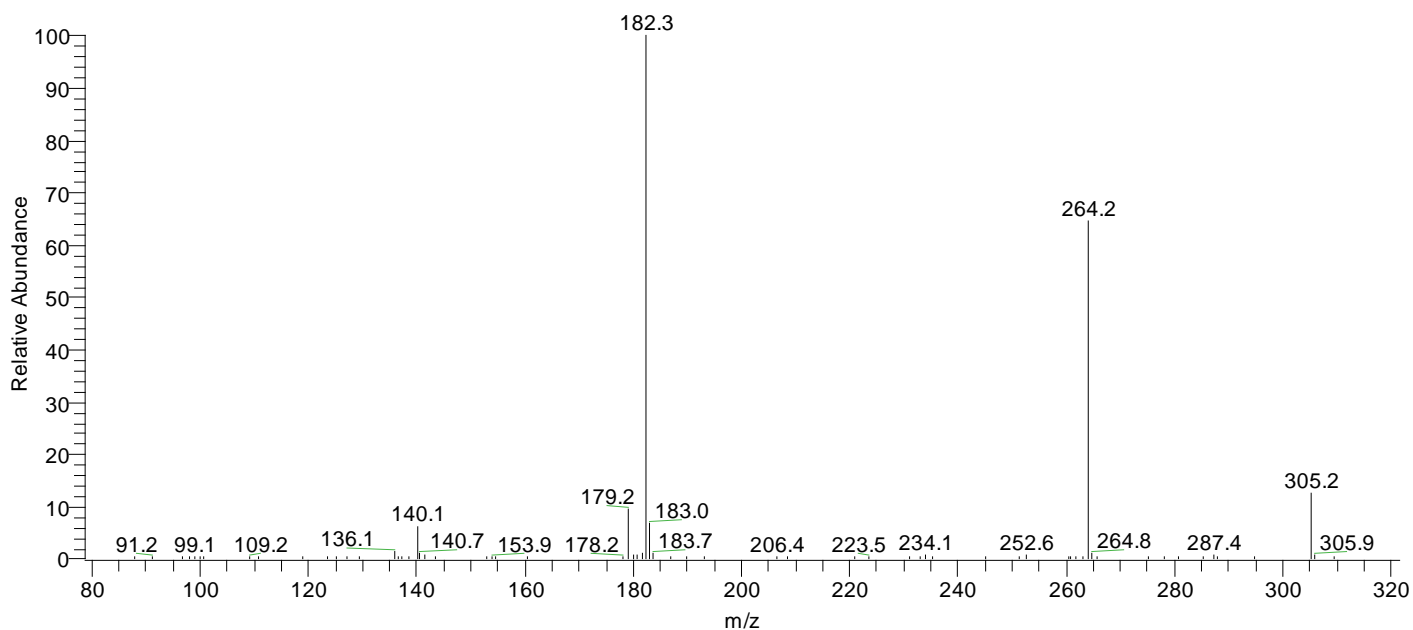


Figure 32. MS<sup>2</sup> of DIC 305 m/z synthesized dendrimer conducted at activation amplitude of 43% and activation time of 4 ms resulting in same two daughter ions as previous spectrum, however a 20% relative abundance increase for the 264 m/z daughter ion.

Further fragmentation was explored for the 264 m/z of larger population resulting from the 4 ms kinetic window. The CID-ESI-MS of daughter ion 264 m/z fragments into two noticeable m/z – 179 and 140 – as seen in Figure 33. As previously mentioned, the DIC structures lack variation of m/z, but can still be used for verification. The movement of any  $\beta$ -deuterium occurs mostly in the 140 m/z range. This is further indicated by the differing daughter ion fragments of the DIC and DOC in this range – DIC exhibits a highly populated state of 140 m/z whereas DOC exhibits highly populated state of 141 m/z. The disagreeing m/z between the DIC and DOC are explained through mechanisms and will be discussed.

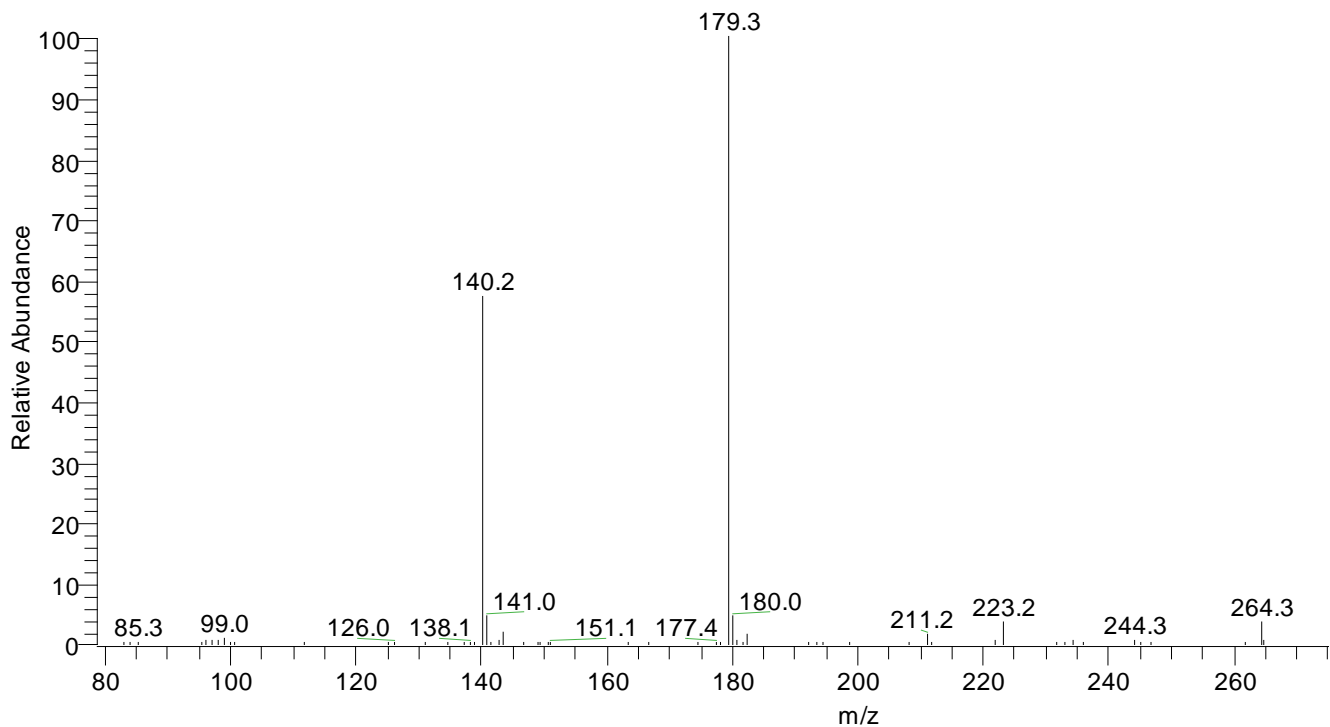


Figure 33. MS<sup>3</sup> of 264 m/z daughter ion at normal kinetic window of 30 ms yielding two fragmentation pathways of large relative abundances at 179 m/z and 140 m/z.

Similar to the DOC dendrimer investigation, the major DIC dendrimer MS<sup>3</sup> daughter ions are explored further with zoom scans around each peak. This allows for comparison to the hypothesized structures and transition states, leading to determination of correct mechanisms with appropriate hydride shifts and double bond migrations.

Examination of the zoom scan around the 179 m/z in Figure 34 reveals agreement with hypothesized structures. Little to no movement of the deuterium atoms creates only two notable m/z peaks – 179 m/z and 182 m/z. Visibly, 179 m/z is the principle structure when paralleled with the 182 m/z of less than 2% relative abundance. By comparison with hypothesized structures, it is evident that the current transition states, structures, and mechanisms are in agreement with the DIC dendrimer fragmentation around 179 m/z.

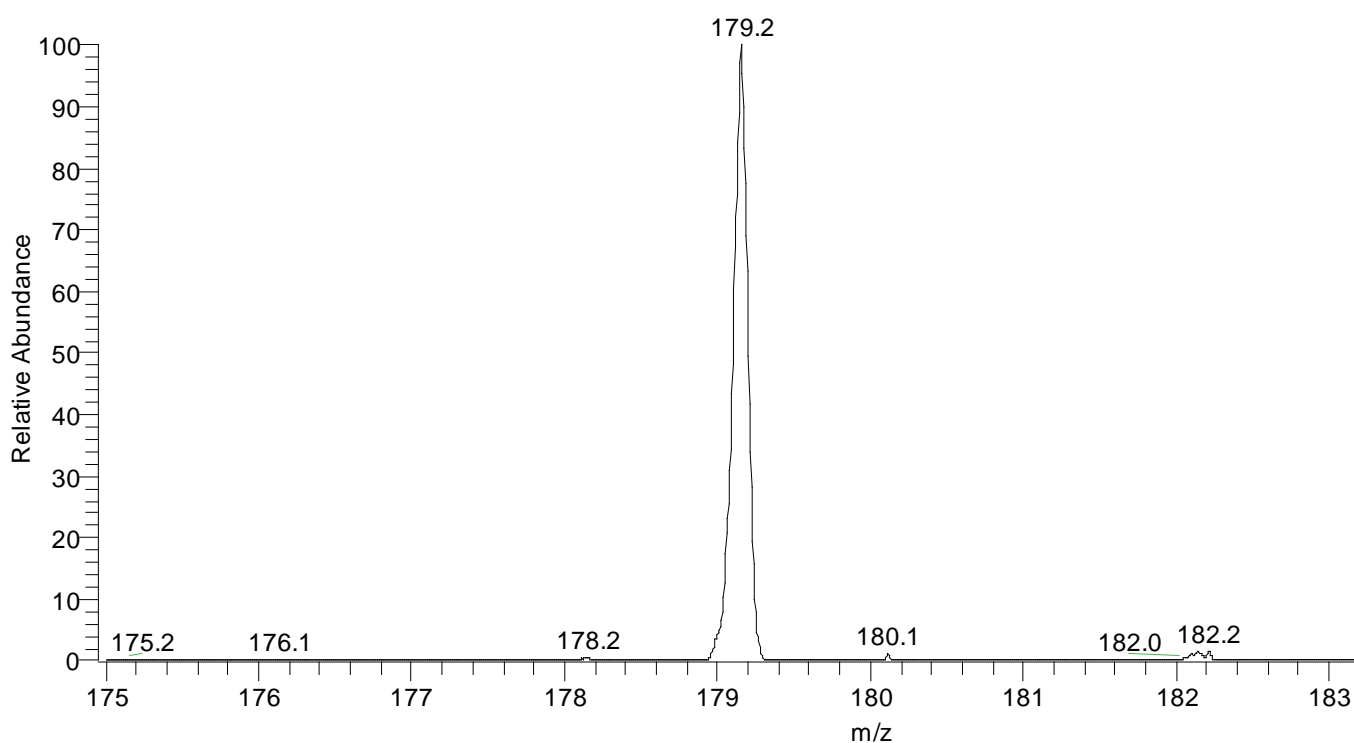


Figure 34. Zoom scan around 179 m/z for the DIC MS<sup>3</sup> spectrum.

The mechanisms for DIC dendrimer mirroring those of the DOC dendrimer are presented in Figure 35. The hypothesized structures for 179 m/z and 182 m/z of the DIC dendrimer have various possible mechanisms and transition states that would yield the same m/z, however since the mechanisms were specific for the DOC dendrimer, the two mechanisms shown for the DIC dendrimer must be the pathway of fragmentation.

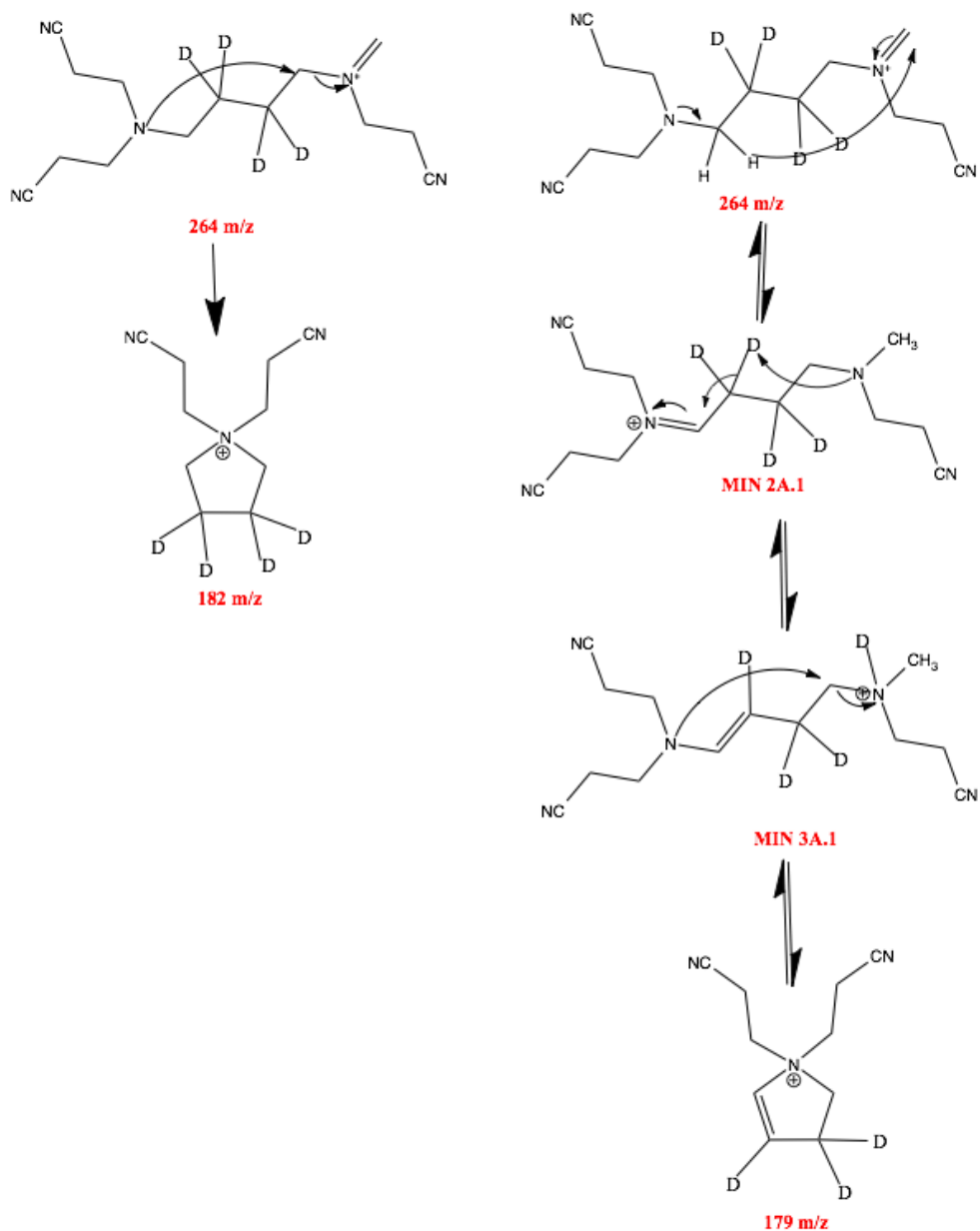


Figure 35. Favored mechanisms for DIC MIN 1A.1  $264\text{ m/z}$  structure yielding predominately  $179\text{ m/z}$  with MIN 2A.1 and MIN 3A.1 transition states and only slight population of  $182\text{ m/z}$  from direct nucleophilic substitution.



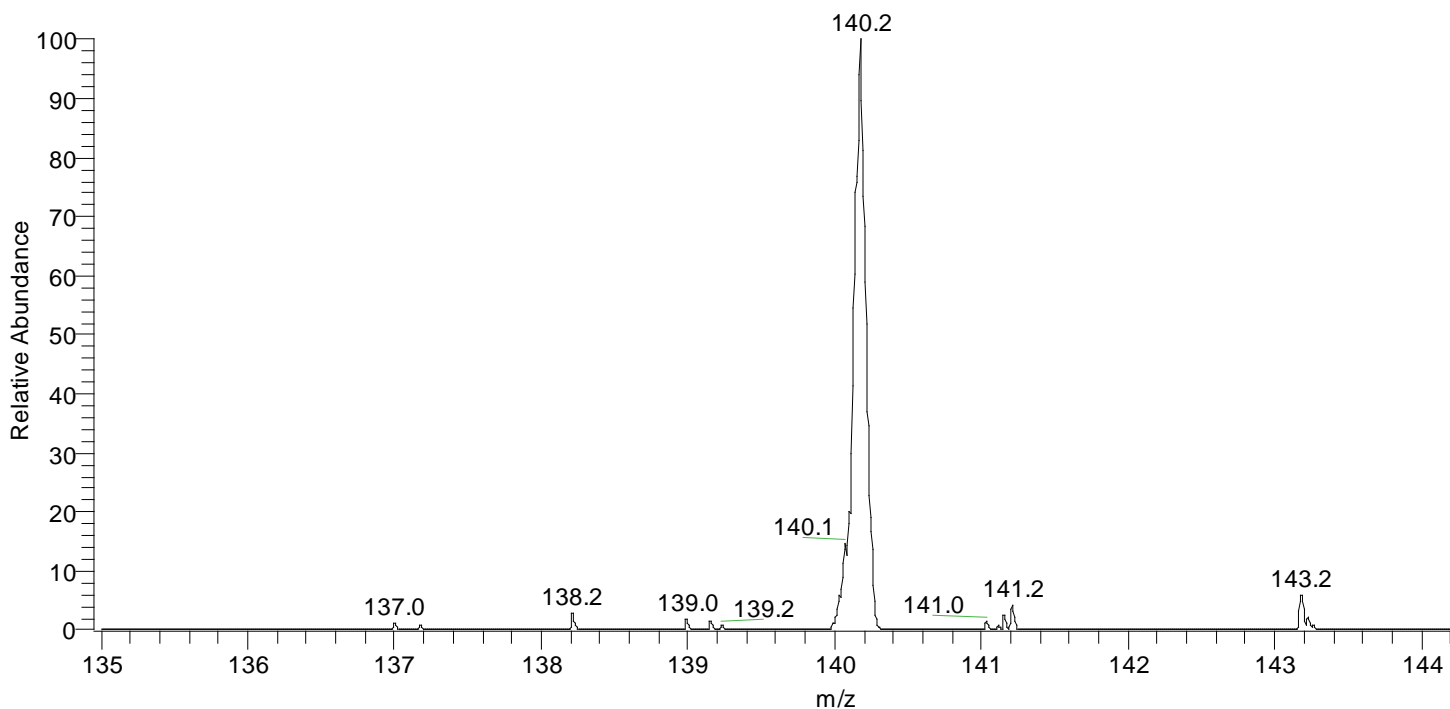


Figure 36. Zoom scan around 140 m/z for DIC MS<sup>3</sup> spectrum.

The zoom scan around the peak of second highest relative abundance in the MS<sup>3</sup> – 140 m/z – is featured in Figure 36. Evaluation of this zoom scan in comparison with the DIC structures hypothesized in Figure 22 confirms mechanisms, yet also raises questions. The m/z of largest state population is clearly that of 140 m/z; this agrees with the hypothesized structures as the only logical transition states and mechanisms for the unsaturated ring structure all result in 140 m/z. The peak at 143 m/z, though a mere 6% of the 140 m/z peak, is also anticipated as it represents the saturated ring structure from direct nucleophilic substitution which remains at low relative abundance as all other saturated ring structures have demonstrated. The corresponding mechanisms for the DIC structures as related to those of the DOC structures are presented in Figure 37.

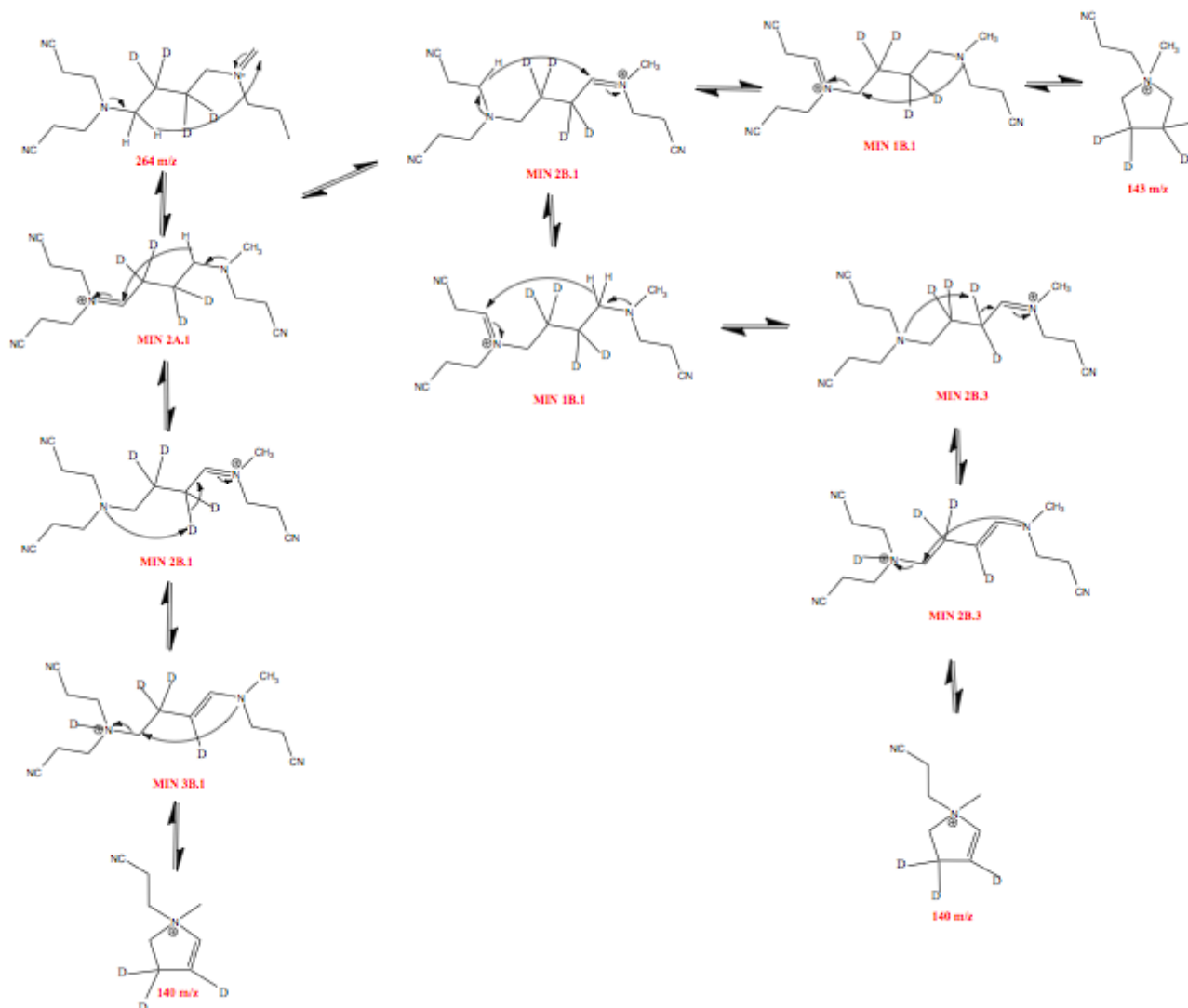


Figure 37. Favored mechanism for formation of highly populated 140 m/z unsaturated ring structure from the MIN 1A.1 264 m/z, as well as the 143 m/z ring structure.

What is questionable is the existence of a peak at 141 m/z; though miniscule, the 141 m/z peak has a relative abundance of about 4%. There are only three possibilities that could account for the appearance of a 141 m/z peak. First, the 141 m/z could be appearing if the saturated ring products lost two of the deuterium atoms resulting in a mass-to-charge ratio of 141 as opposed to 143. This is highly unlikely as the spectrum lacks a peak at 142 m/z which supports the

assumption that the saturated ring structure does not lose a  $\beta$ -deuterium as it does the  $\alpha$ -deuterium evidenced in the DOC dendrimer spectrum. The next possibility for the appearance of 141 m/z is the result of a  $\beta$ -deuteride shifting to the methyl arm. This is a slightly more reasonable explanation, however this would insinuate that the mechanism leading from the 264 m/z MIN 1A.1 structure to the MIN 2A.1 transition state is incorrect, which would invalidate many other mechanisms. Also, if a  $\beta$ -deuteride shifted to the methyl arm transitioning from the MIN 1A.1 structure, this would complicate things mechanistically, as a double bond would be placed in the middle of the carbons on the core. This is also unlikely – a logical first step for many of the mechanisms hypothesized creates an imine double bond in which the pi electrons can move to the electrophilic nitrogen if necessary. The final plausible explanation for appearance of a 141 m/z peak is an incorrect mechanism for the transition between MIN 1A.2 and MIN 2A.2 – instead of another  $\alpha$ -hydride shift (or  $\alpha$ -deuteride in the DOC structures), a  $\beta$ -deuteride shift could be occurring. In order for this to be feasible, the  $\beta$ -deuteride shift would have to be followed by  $\alpha$ -hydride shift to the adjacent carbon. This elaborate, yet most reasonable mechanism is shown in Figure 38.

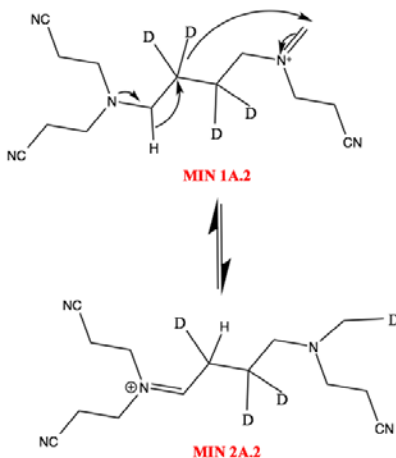


Figure 38. Proposed mechanism for MIN1A.2 transition to MIN 2A.2 explaining appearance of 141 m/z in DIC MS<sup>3</sup>.

## ALKALI AND ALKALINE EARTH METAL-DENDRIMER COMPLEXES

The CID-ESI-MS of various alkali and alkaline earth metals complexed with the G1 nitrile-terminated PPI dendrimer were investigated in hopes of revealing more about how changing the metal affects the fragmentation pathways of the dendrimer. By utilizing metal ions, the labile proton does not have to be considered in the mechanism.

### Sodium-Dendrimer Complex

Sodium-dendrimer complexes were created by utilizing the G1 nitrile-terminated PPI dendrimer of 300 g/mol and adding a sodium acetate solution. Complex was electrosprayed and consequently subjected to CID giving the MS<sup>2</sup> spectrum in Figure 39.

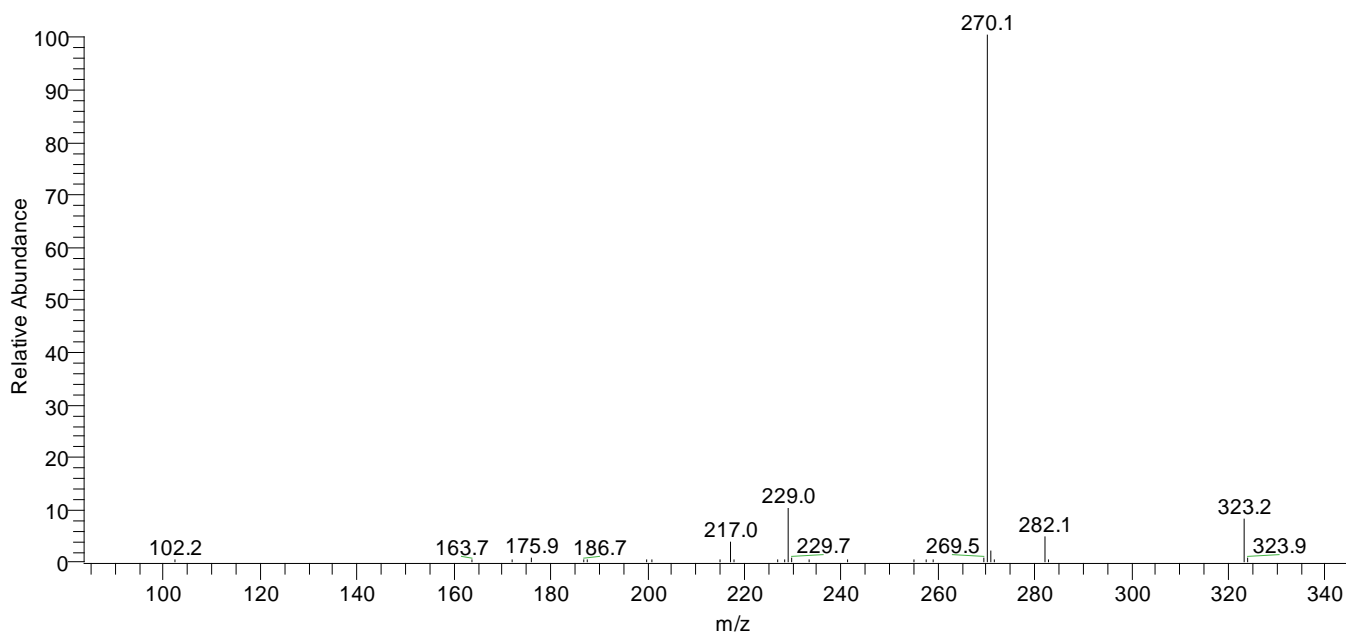


Figure 39. MS<sup>2</sup> of sodium-dendrimer complex with activation time of 30 ms.

The parent ion of 323 m/z accounts for a singly charged complex between one dendrimer molecule and one sodium ion. When subjected to CID, the parent ion yields a primary daughter

ion of 270 m/z, corresponding to a neutral loss of 53 amu. A loss of 53 amu would indicate loss of acrylonitrile.

Subsequent CID of the 270 m/z daughter ion was performed resulting in the spectrum in Figure 40. The fragmentation of the 270 m/z structure yields two daughter ions of 229 m/z and 217 m/z. The loss of neutral 41 amu from the 270 m/z to the 229 m/z daughter ion indicates loss of an arm, causing imine formation. The daughter ion at 217 m/z results from another loss of 53 amu which corresponds, again, to loss of acrylonitrile. The structures and resulting daughter ions are outlined in Table 3.

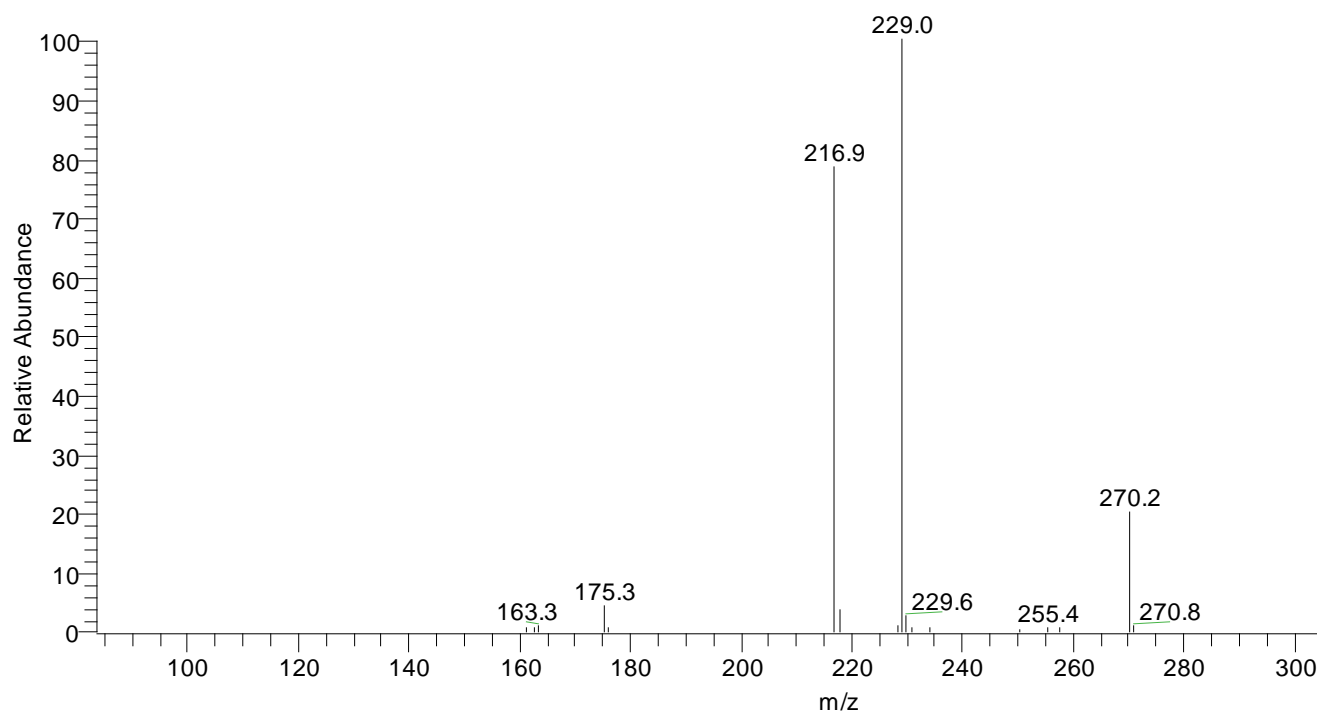


Figure 40. MS<sup>3</sup> of sodium-dendrimer complex with activation time of 30 ms.

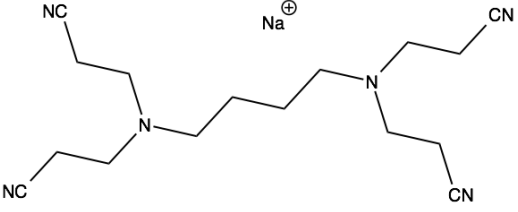
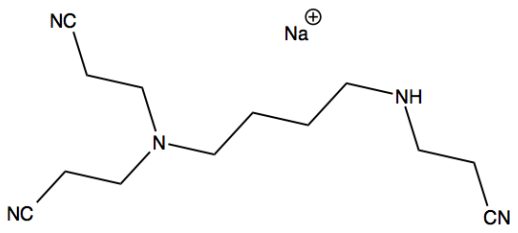
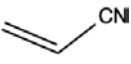
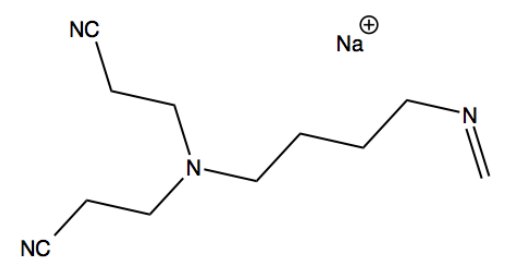
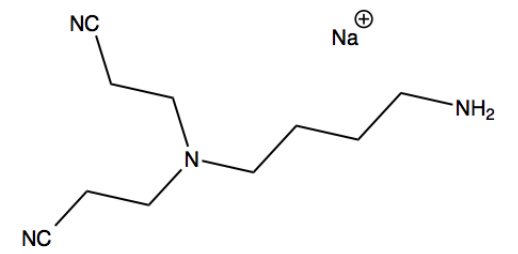
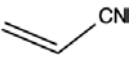
Fragment (m/z)	CID Phase	Structure	Resulted from loss of (amu):	Resulted from loss of (structure):
323	MS		N/A	N/A
270	MS <sup>2</sup>		53	
229	MS <sup>3</sup>		41	CH <sub>3</sub> -CN
217	MS <sup>3</sup>		53	

Table 3. Sodium-dendrimer complex fragmentation structures.

## Potassium-Dendrimer Complex

Potassium-dendrimer complexes were created by utilizing the G1 nitrile-terminated PPI dendrimer of 300 g/mol and adding a potassium acetate solution. Complex was electrosprayed and consequently subjected to CID giving the MS<sup>2</sup> spectrum in Figure 41.

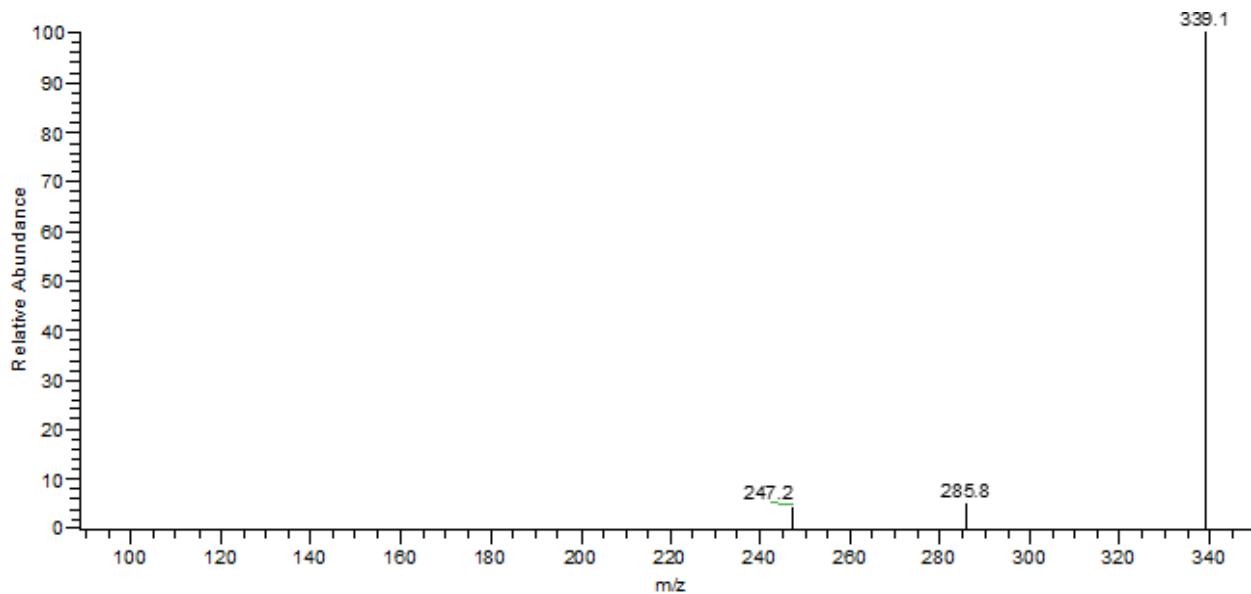


Figure 41. MS<sup>2</sup> of potassium-dendrimer complex with activation time of 30 ms.

The parent ion of 339 m/z corresponds to a singly charged complex between one dendrimer molecule and one potassium ion. Fragmentation of the 339 m/z parent ion was very sensitive; more activation amplitude applied caused all fragments in the ion-trap to be ejected. The resulting spectrum in Figure 41 is the only way to see daughter ions. The 339 m/z structure has two fragmentation pathways at 286 m/z and 247 m/z. Further CID experiments could not be performed due to the aforementioned sensitivity. Table 4 indicates the corresponding structures for the mass-to-charge ratios.

Fragment (m/z)	CID Phase	Structure	Results from loss of (amu):	Results from loss of (structure):
339	MS		N/A	N/A
286	MS <sup>2</sup>		53	
247	MS <sup>2</sup>		92	

Table 4. Potassium-dendrimer complex fragmentation structures.

The loss of a neutral 53 amu, much like in the sodium-dendrimer CID-ESI-MS, from the parent ion of 339 m/z results in the 286 m/z potassium-dendrimer daughter ion. The daughter ion at 247 m/z results from the same loss of 53 amu (acrylonitrile) with subsequent loss of the CH-CN radical.



## Magnesium-Dendrimer Complex

Magnesium-dendrimer complexes were created by utilizing the G1 nitrile-terminated PPI dendrimer of 300 g/mol and adding a magnesium chloride solution. Complex was electrosprayed and consequently subjected to CID giving the MS<sup>2</sup> spectrum in Figure 42.

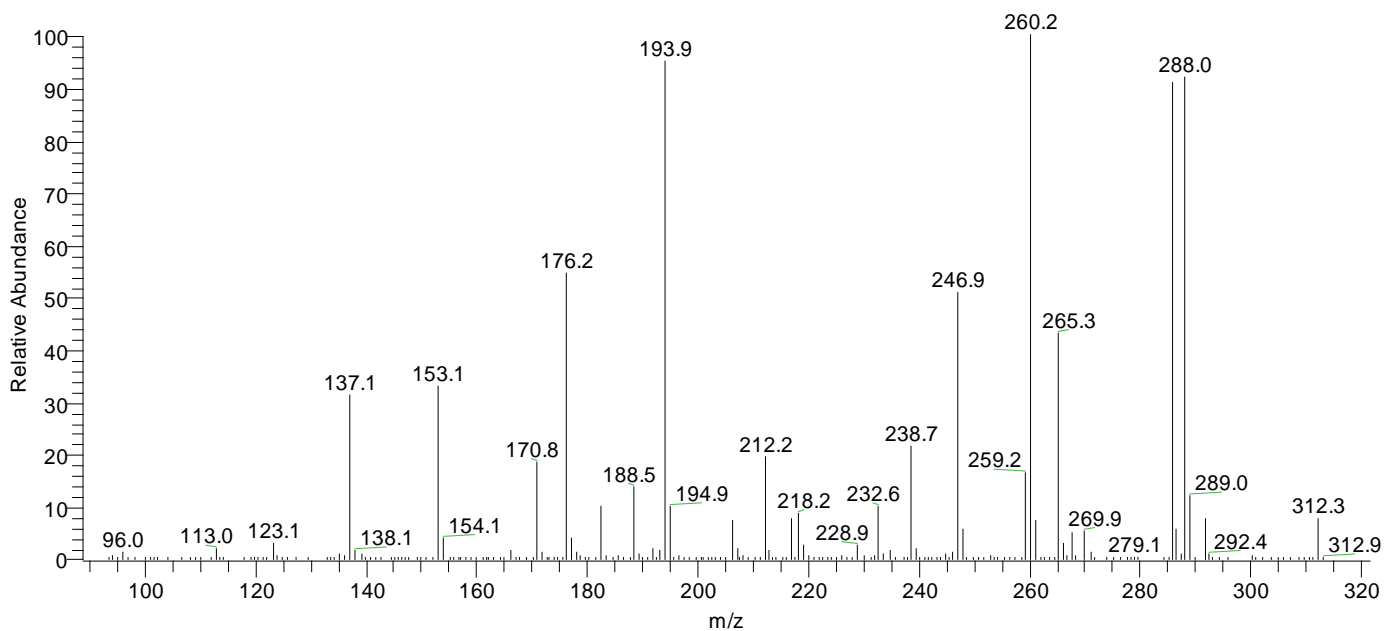


Figure 42. MS<sup>2</sup> of magnesium-dendrimer complex with activation time of 30 ms.

The parent ion for the magnesium-dendrimer complex is 312 m/z. This, as well as the presence of two peaks in the single m/z of 312, indicates that the complex is doubly charged. This implies the presence of two dendrimer molecules per one Mg<sup>2+</sup> ion. Fragmentation of the parent ion results in a surplus of daughter ions. The determined structures for daughter ions and neutral losses are listed in Table 5.

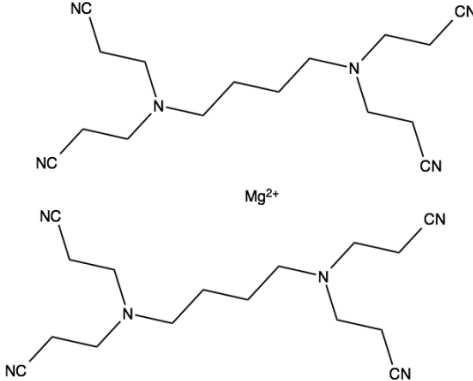
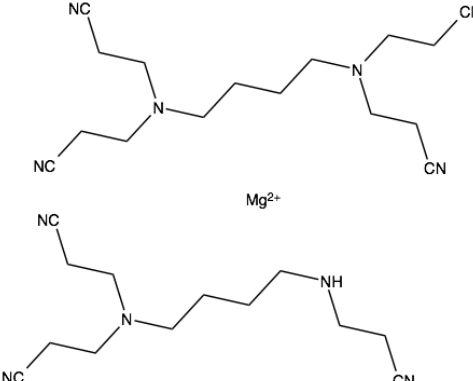
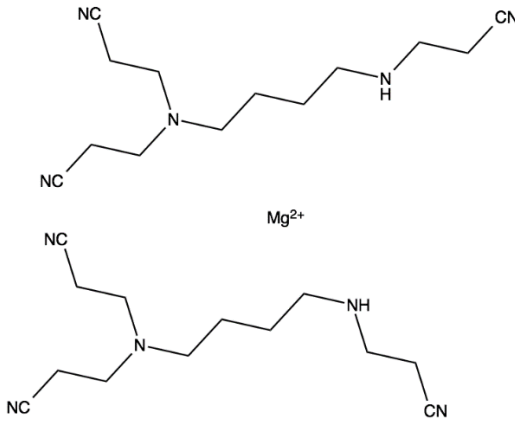
Fragment (m/z)	CID Phase	Structure	Loss of (amu):	Loss of (structure):
312 <i>m=624</i> <i>z=2</i>	MS		N/A	N/A
286 <i>m=572</i> <i>z=2</i>	MS <sup>2</sup>		52	·CHCHCN
260 <i>m=520</i> <i>z=2</i>	MS <sup>2</sup>		104	·CHCHCN + ·CHCHCN

Table 5. Magnesium-dendrimer complex fragmentation structures.

## Calcium-Dendrimer Complexes

Calcium-dendrimer complexes were created by utilizing the G1 nitrile-terminated PPI dendrimer of 300 g/mol and adding a calcium acetate solution. Complex was electrosprayed and consequently subjected to CID giving the MS<sup>2</sup> spectrum in Figure 43.

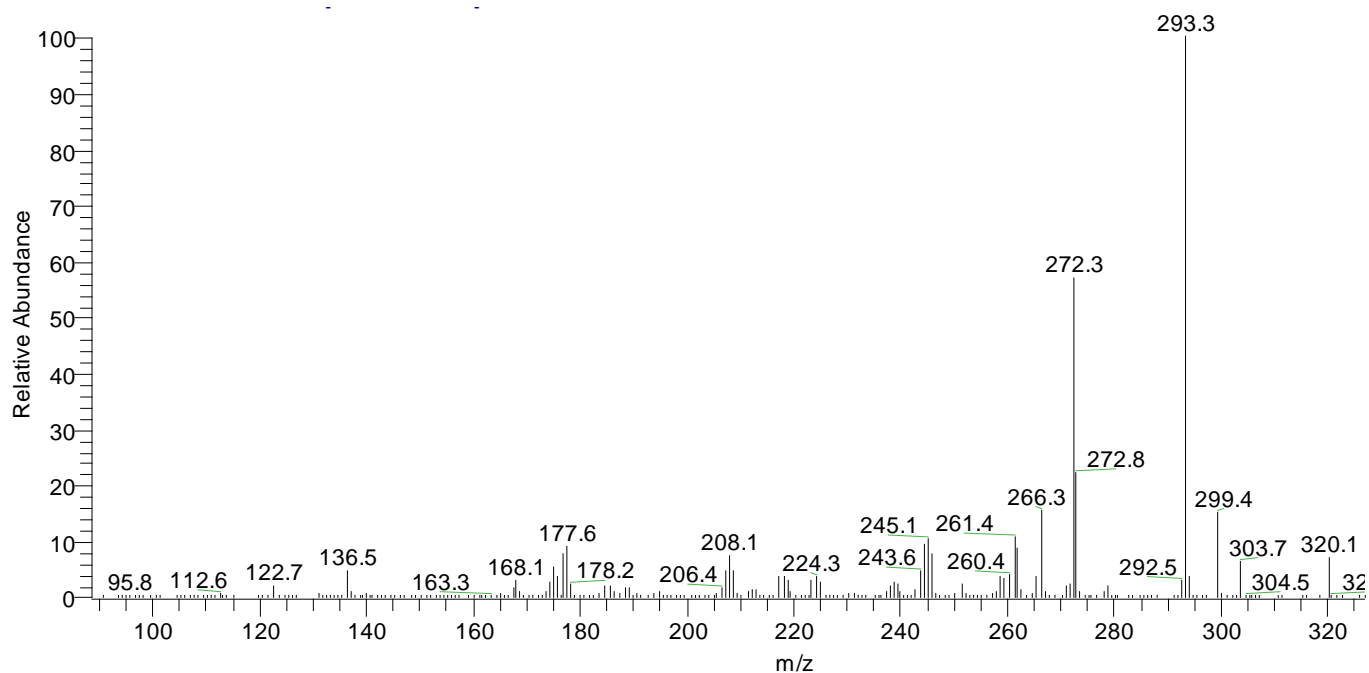


Figure 43. MS<sup>2</sup> of calcium-dendrimer complex with activation time of 30 ms.

The parent ion of 320 m/z has a primary daughter ion at 293 m/z. The 320 m/z ion is doubly charged due to the presence of two peaks in the 320 m/z range. The 320 m/z parent ion is comprised of two dendrimer molecules and a one Ca<sup>2+</sup> ion. Another notable daughter ion is at 272 m/z. Table 6 shows the determined structures for daughter ions and corresponding losses.

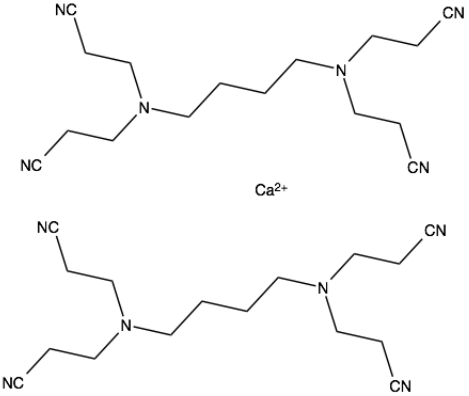
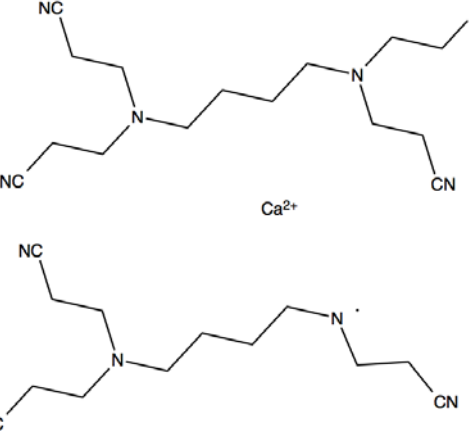
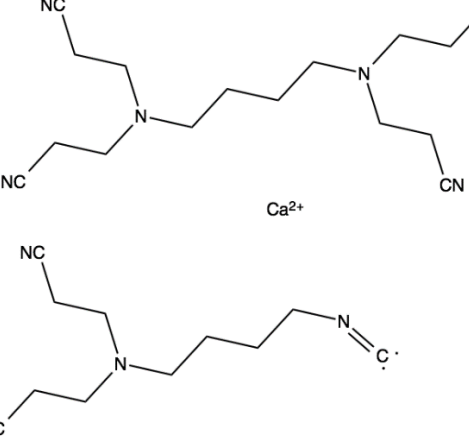
Fragment (m/z)	CID phase	Structure	Loss of (amu):	Loss of (structure):
<b>320</b>  <i>m=640</i> <i>z=2</i>	MS	 <p style="text-align: center;">Ca<sup>2+</sup></p>	N/A	N/A
<b>293</b>  <i>m=586</i> <i>z=2</i>	MS <sup>2</sup>	 <p style="text-align: center;">Ca<sup>2+</sup></p>	54	·CH <sub>2</sub> CH <sub>2</sub> CN
<b>272</b>  <i>m=544</i> <i>z=2</i>	MS <sup>2</sup>	 <p style="text-align: center;">Ca<sup>2+</sup></p>	96	CH <sub>3</sub> CH <sub>2</sub> CN + CH <sub>3</sub> CN

Table 6. Calcium-dendrimer complex fragmentation structures.

## CHAPTER FIVE

### CONCLUSIONS

Mass spectrometry has proven to be a useful analytical tool in the probing of complex, hyperbranched polymers. This thesis used a rapid and precise analytical framework for the characterization of dendrimers by systematically probing the electrospray ionization mass spectrometry (ESI-MS) speciation and the gas-phase collision-induced dissociation (CID) fragmentation patterns for G1 nitrile-terminated polypropylene imine (PPI) dendrimers. Two isotopically labeled dendrimer species were employed for unambiguous assignment of complex structures and mechanisms. Hypothesized mechanisms were verified, again reinforcing the existence of inconsistency between experimental CID data and highly accurate CBS-QB3 quantum calculations. While one anomaly presented for the  $\beta$ -labeled dendrimer and a possible mechanism was presented, further experimentation is necessary to determine the exact cause for its creation. Also, the fragmentation patterns of certain alkali and alkaline earth metal-dendrimer complexes were investigated. These complexes of +1 and +2 charges exhibited similar neutral losses of acrylonitrile and acetonitrile. Losses of radicals also appeared for potassium-, magnesium-, and calcium-dendrimer complexes as the only possible explanation for specific losses, such as 54 amu. However, substituting the labile proton with a metal ion exhibited different fragmentation mechanisms than those of the protonated nitrile-terminated PPI dendrimer.

## REFERENCES

1. Grayson, S.M.; Fréchet, J.M.J. Convergent Dendrons and Dendrimers: From Synthesis to Applications. *Chem. Rev.* **2001**, *101*, 3819-3867.
2. Tomalia, D.A.; Fréchet, J.M.J. Discovery of Dendrimers and Dendritic Polymers: A Brief Historical Perspective. *J. Polymer Science: Part A: Polymer Chemistry.* **2002**, *40*, 2719-2728.
3. Vögtle, F.; Buhleier, E.; Wehner, W. "Cascade"- and "Nonskid-chain-like"- Syntheses of Molecular Cavity Topologies. *Synthesis.* **1978**, *2*, 155-158.
4. Tomalia, D.A.; Christensen, J.B.; Boas, U. *Dendrimers, Dendrons, and Dendritic Polymers: Discovery, Applications, and the Future*; Cambridge University Press: New York, 2012; p. 121.
5. Tomalia, D.A.; Dewald, J.R.; Hall, M.R.; Martin, S.J.; Smith, P.B. Preprints of the 1st International Polymer Conference, Society of Polymer Science Japan, Kyoto, 1984; 65.
6. Tomalia, D.A.; Baker, H.; Dewald, J.; Hall, M.; Kallos, G.; Martin, S.; Roeck, J.; Ryder, J.; Smith, P.A. New Class of Polymers: Starburst-Dendritic Macromolecules. *Polymer J.* **1985**, *17*, 117-132.
7. Jansen, J. F. G. A.; de Brabander-van den Berg, E. M. M.; Meijer, E. W. Encapsulation of Guest Molecules into a Dendritic Box. *Science*, **1994**, *266*, 1226-1229.
8. Boas, U.; Christensen, J.B.; Heegaard, P.M.H. Dendrimers: Design, Synthesis, and Chemical Properties. *J. Mater. Chem.* **2006**, *16*, 3785-3798.
9. Noriega-Luna, B.; Godinez, L.A.; Rodriguez, F.J.; Rodriguez, A.; de Larrea, G.Z.; Sosa-Ferreya, C.F.; Mercado-Curiel, R.F.; Manriquez, J.; Bustos, E. Applications of Dendrimers in Drug Delivery Agents, Diagnosis, Therapy, and Detection. *J. Nanomater.* **2014**, *2014*, 1-19.
10. Tripathy, S.; Das, M.K. Dendrimers and their Applications as Novel Drug Delivery Carriers. *J. App. Pharm. Sci.* **2013**, *3*, 142-149.
11. Niu, Y.; Crooks, R.M. Dendrimer-encapsulated Metal Nanoparticles and their Applications to Catalysis. *C. R. Chimie.* **2003**, *6*, 1049-1059.
12. Jeffery, T. Recent Improvements and Developments in Heck-type Reactions and their Potential in Organic Synthesis. *Advances in Metal-Organic Chemistry.* **1996**, *5*, 153-260.
13. Rahim, E.H.; Kamounah, F.S.; Frederiksen, J.; Christensen, J.B. Heck Reactions Catalyzed by PAMAM-Dendrimer Encapsulated Pd(0) Nanoparticles. *Nano Lett.* **2001**, *1*, 499-501.
14. Bradshaw, D.S.; Andrews, D.L. Mechanisms of Light Energy Harvesting in Dendrimers and Hyperbranched Polymers. *Polymers.* **2011**, *3*, 2053-2077.
15. Caminade, A.; Laurent, R.; Majoral, J. Characterization of Dendrimers. *Advanced Drug Delivery Reviews.* **2005**, *57*, 2130-2146.
16. McLuckey, S.; Asano, K.; Schaaff, G.; Stephenson Jr., J. Ion Trap Collisional Activation of Protonated Poly(Propylene Imine) Dendrimers. *Int. J. Mass Spectrom.* **2000**, *195/196*, 419-437.
17. Gautam, S.P.; Gupta, A.K.; Agrawal, S.; Sureka, S. Spectroscopic Characterization of Dendrimers. *Int. J. Pharm. Pharm. Sci.* **2012**, *4*, 78-80.
18. Banerjee, S.; Mazumdar, S. Electrospray Ionization Mass Spectrometry: A Technique to Access the Information beyond the Molecular Weight of the Analyte. *Int. J. Anal. Chem.* **2011**, *2012*, 1-40.

19. Dole, M.; Mach, L.L.; Hines, R.L.; Mobley, R.C.; Ferguson, L.P.; Alice, M.P. Molecular Beams of Macroions. *J. Chem. Phys.* **1968**, *49*, 2240–2249.
20. Fenn, J.B. Electrospray Ionization Mass Spectrometry: How It All Began. *J. Biomol. Tech.* **2002**, *13*, 101-118.
21. Ho, C.S.; Lam, C.W.K.; Chan, M.H.M.; Cheung, R.C.K.; Law, L.K.; Lit, L.C.W.; Ng, K.F.; Suen, M.W.M.; Tai, H.L. Electrospray Ionisation Mass Spectrometry: Principles and Clinical Applications. *Clin. Biochem. Rev.* **2003**, *24*, 3-12.
22. Rayleigh, J.W.S. On an Instrument Capable of Measuring the Intensity of Aerial Vibrations. *Phil. Mag.* **1882**, *14*, 186-187.
23. Paul, W. Electromagnetic Traps for Neutral and Charged Particles. *Rev. Mod. Phys.* **1990**, *62*, 531-540.
24. Sleno, L.; Volmer, D. A. Ion Activation Methods for Tandem Mass Spectrometry. *J. Mass Spectrom.* **2004**, *39*, 1091-1112.
25. Batchelor, J.D. Mass Spectrometry of Dendrimer Metal Complexes. M.S. Thesis. Marshall University, Huntington, WV, 2008.
26. Pack, K.N. Elucidation of Fragmentation Pathways of Nitrile-Terminated PPI Dendrimers. M.S. Thesis. Marshall University, Huntington, WV, 2010.
27. Weener, J.W.; Van Dongen, J. L. J.; Meijer, E. W. Electrospray Mass Spectrometry Studies of Poly(Propylene Imine) Dendrimers: Probing Reactivity in the Gas Phase. *J. Am. Chem. Soc.* **1999**, *121*, 10346-10355.
28. Price, W.D.; Gemayal, K.; Hendrix, J.; Kilgore, J. T. DFT Comparison of the Fragmentation Pathways of Protonated First-Generation Nitrile-Terminated PPI Dendrimers. Presented at the 243<sup>rd</sup> ACS National Meeting, San Diego, CA, March 25-29, 2012.
29. Price, W.D.; Bott, H.E.; Doerner, C.; Gemayal, K. Computational and Experimental Investigation of the Fragmentation Pathways of First Generation Protonated Nitrile-Terminated PPI Dendrimer. Presented at the 246<sup>th</sup> ACS National Meeting, Indianapolis, IN, September 8-12, 2013.
30. Montgomery, J.A.; Frisch, M.J.; Ochterski, J.W.; Petersson, J.A. A Complete Basis Set Model Chemistry. VI. Use of Density Functional Geometries and Frequencies. *J. Chem. Phys.* **1999**, *110*, 2822.
31. van der Wal, S.J.; De Brabander, E.M.M.; Brackman, J.; Mure-Mak, M.; De Man, H.; Hogeweg, M.; Keulen, J.; Scherrenberg, R.; Coussens, B.; Mengerink, Y. Polypropylenimine dendrimers: Improved Synthesis and Characterization. *Macromol. Symp.* **1996**, *102*, 9–17.

## APPENDIX A



Office of Research Integrity  
Institutional Review Board

March 9, 2015

Hannah E. Bott  
629 14th Street  
Huntington, WV 25701

Dear Ms. Bott:

This letter is in response to the submitted thesis abstract entitled "*Probing a Complex Dissociation Energy Surface with Experimental and Theoretical Methods.*" After assessing the abstract it has been deemed not to be human subject research and therefore exempt from oversight of the Marshall University Institutional Review Board (IRB). The Code of Federal Regulations (45CFR46) has set forth the criteria utilized in making this determination. Since the information in this study does not involve human subjects as defined in the above referenced instruction it is not considered human subject research. If there are any changes to the abstract you provided then you would need to resubmit that information to the Office of Research Integrity for review and a determination.

I appreciate your willingness to submit the abstract for determination. Please feel free to contact the Office of Research Integrity if you have any questions regarding future protocols that may require IRB review.

Sincerely,

A handwritten signature in blue ink that reads 'Bruce F. Day'.

Bruce F. Day, ThD, CIP  
Director



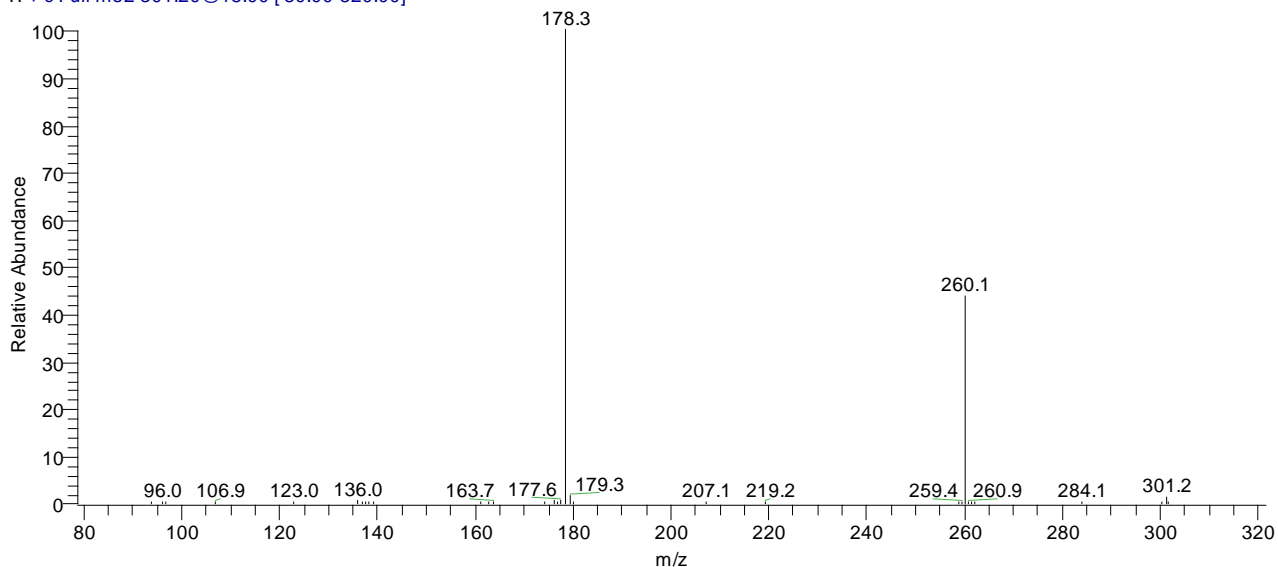
## APPENDIX B

### SUPPLEMENTARY SPECTRA

This appendix contains representative raw mass spectra for the monotopic protonated, isotopically labeled, and alkali/alkaline-earth metal complexed dendrimers.

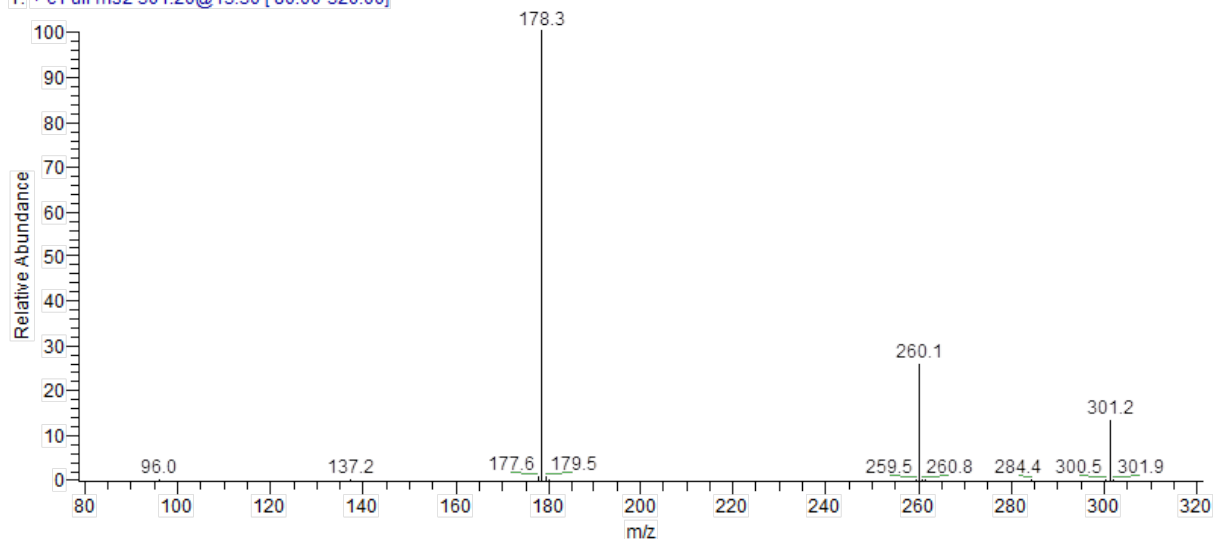
#### Protonated G1 nitrile-terminated PPI dendrimer – MS<sup>2</sup> 301 m/z at 30 ms time:

ms2\_301\_18\_2\_30#1-99 RT: 0.01-1.26 AV: 99 NL: 5.34E6  
T: + c Full ms2 301.20@18.00 [ 80.00-320.00]



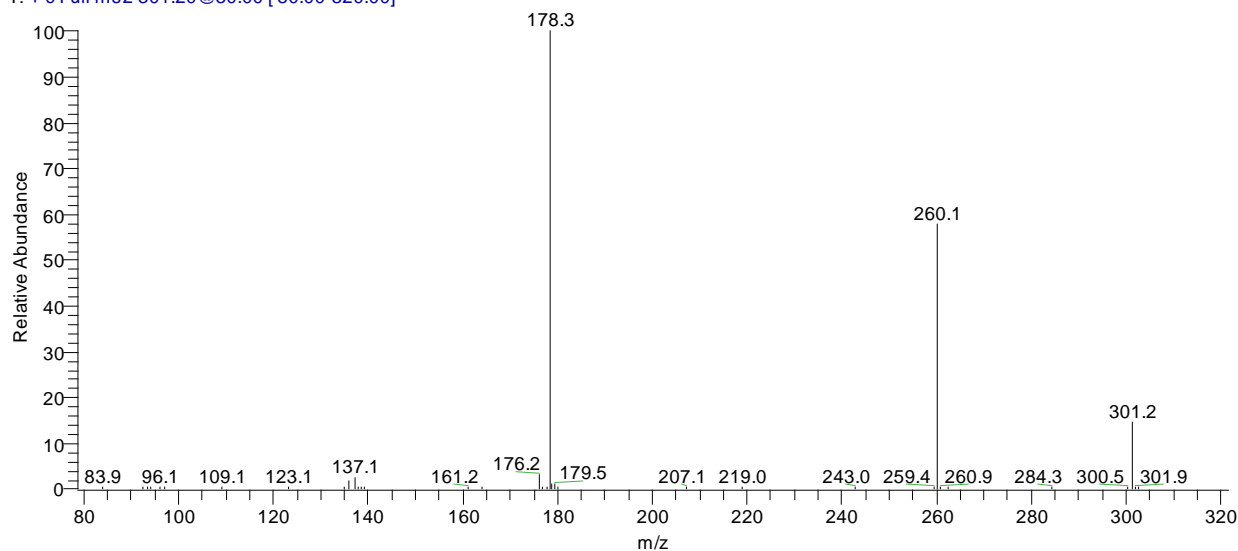
#### Protonated G1 nitrile-terminated PPI dendrimer – MS<sup>2</sup> 301 m/z at 1000 ms time:

ms2\_301\_13\_1000#1-29 RT: 0.03-1.74 AV: 29 NL: 6.47E6  
T: + c Full ms2 301.20@13.30 [ 80.00-320.00]



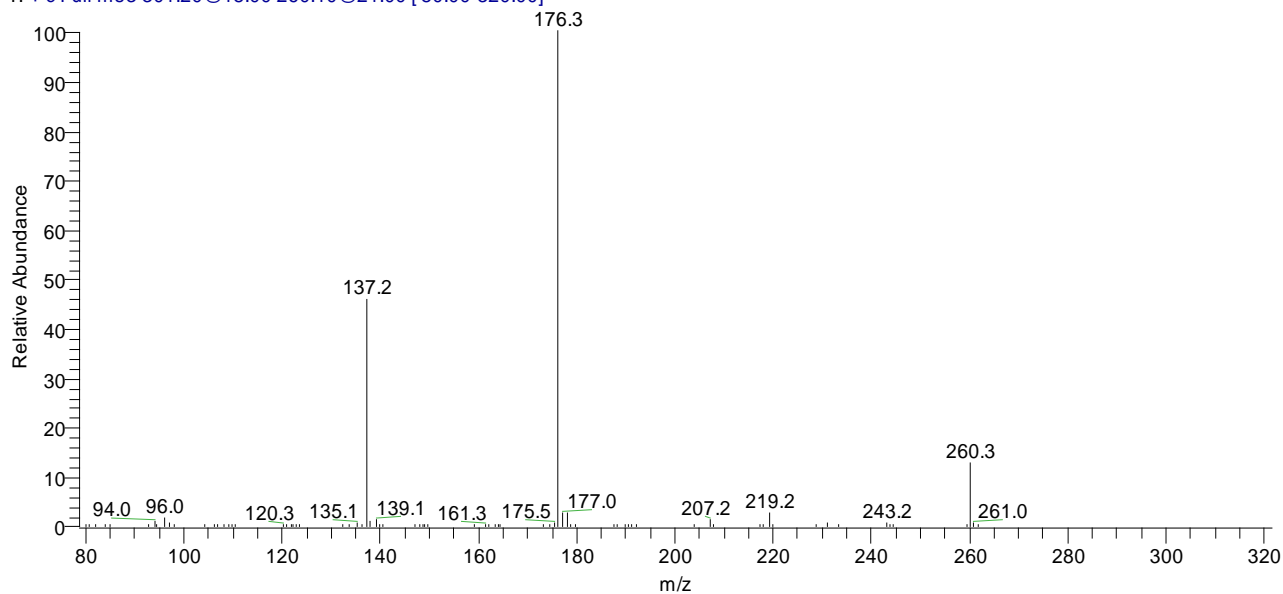
Protonated G1 nitrile-terminated PPI dendrimer – MS<sup>2</sup> 301 m/z at 5 ms time:

ms2\_301\_30\_5#1-30 RT: 0.01-0.34 AV: 30 NL: 4.42E6  
T: + c Full ms2 301.20@30.00 [80.00-320.00]



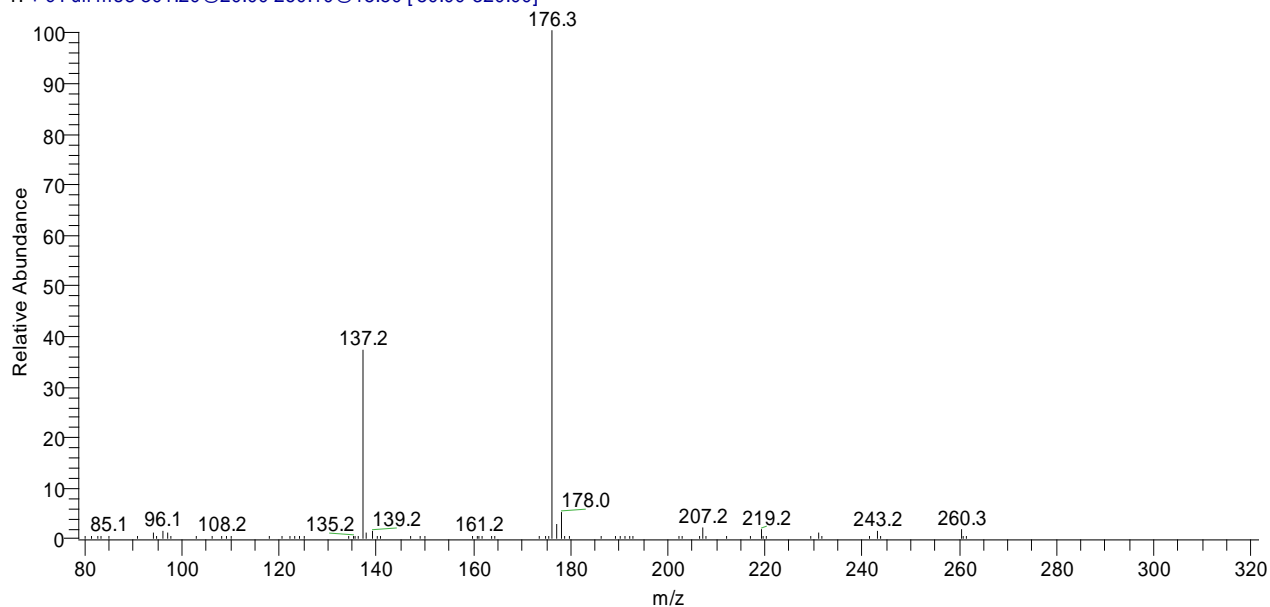
Protonated G1 nitrile-terminated PPI dendrimer – MS<sup>3</sup> 260 m/z at 30 ms time:

ms3\_260\_21\_30\_2#1-100 RT: 0.01-1.60 AV: 100 NL: 6.90E5  
T: + c Full ms3 301.20@18.00 260.10@21.00 [80.00-320.00]



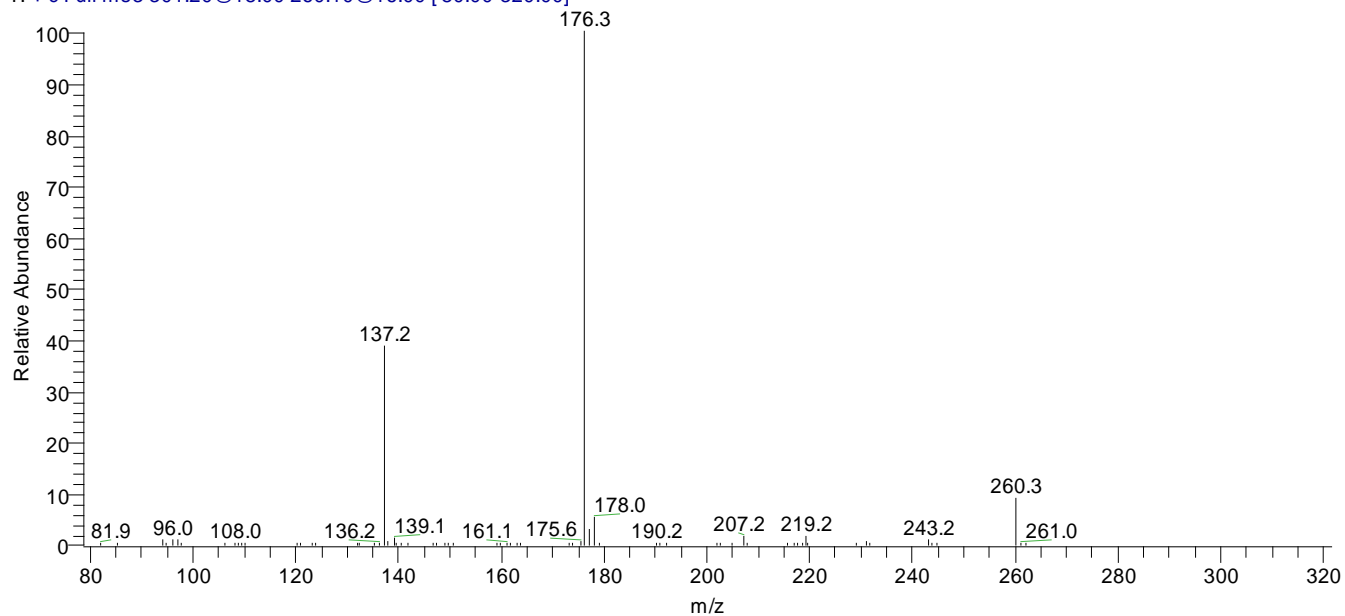
Protonated G1 nitrile-terminated PPI dendrimer – MS<sup>3</sup> 260 m/z at 3000 ms time:

ms3\_260\_15.5\_3000#1-100 RT: 0.10-16.32 AV: 100 NL: 1.71E6  
T: + c Full ms3 301.20@20.00 260.10@15.50 [ 80.00-320.00]



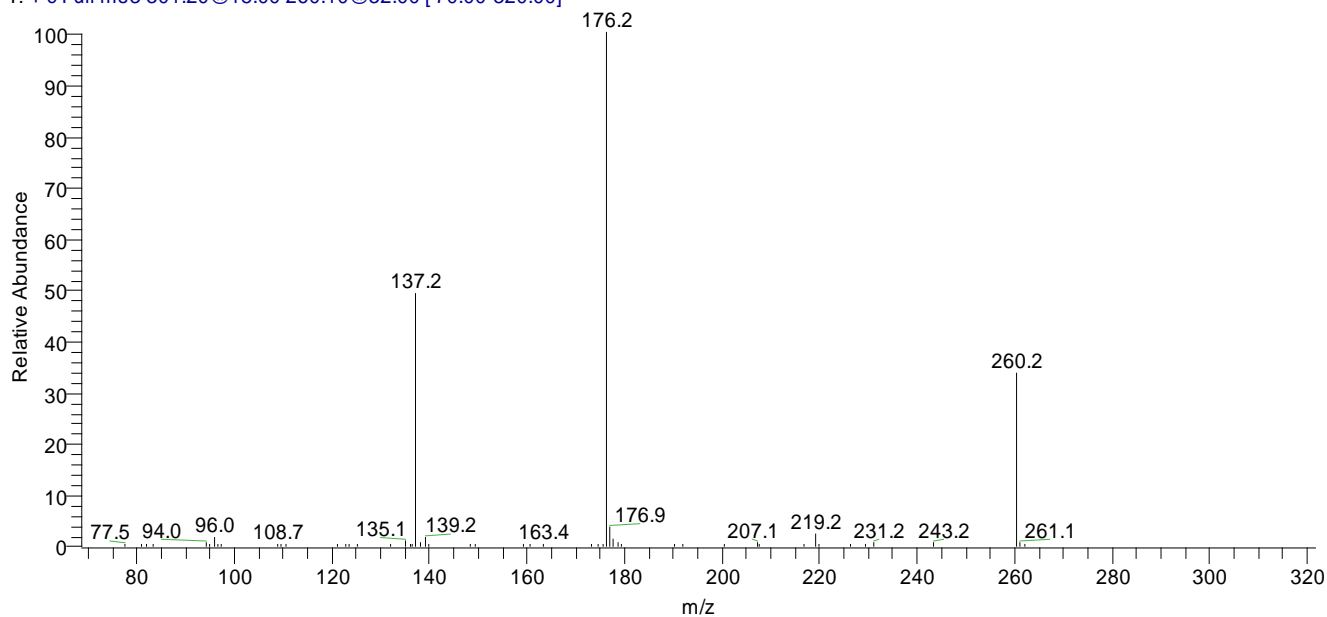
Protonated G1 nitrile-terminated PPI dendrimer – MS<sup>3</sup> 260 m/z at 1000 ms time:

ms3\_260\_16\_1000\_2#2-100 RT: 0.07-6.40 AV: 99 NL: 7.54E5  
T: + c Full ms3 301.20@18.00 260.10@16.00 [ 80.00-320.00]



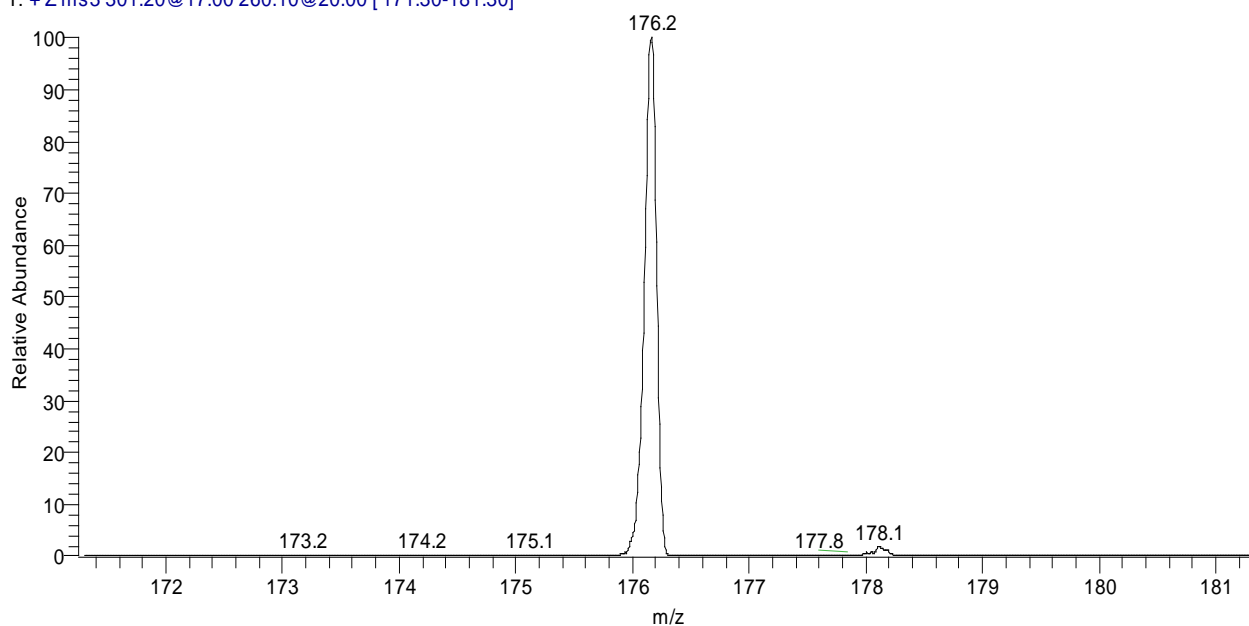
Protonated G1 nitrile-terminated PPI dendrimer – MS<sup>3</sup> 260 m/z at 5 ms time:

ms3\_260\_32\_5#1-30 RT: 0.00-0.40 AV: 30 NL: 1.24E6  
T: + c Full ms3 301.20@18.00 260.10@32.00 [ 70.00-320.00]



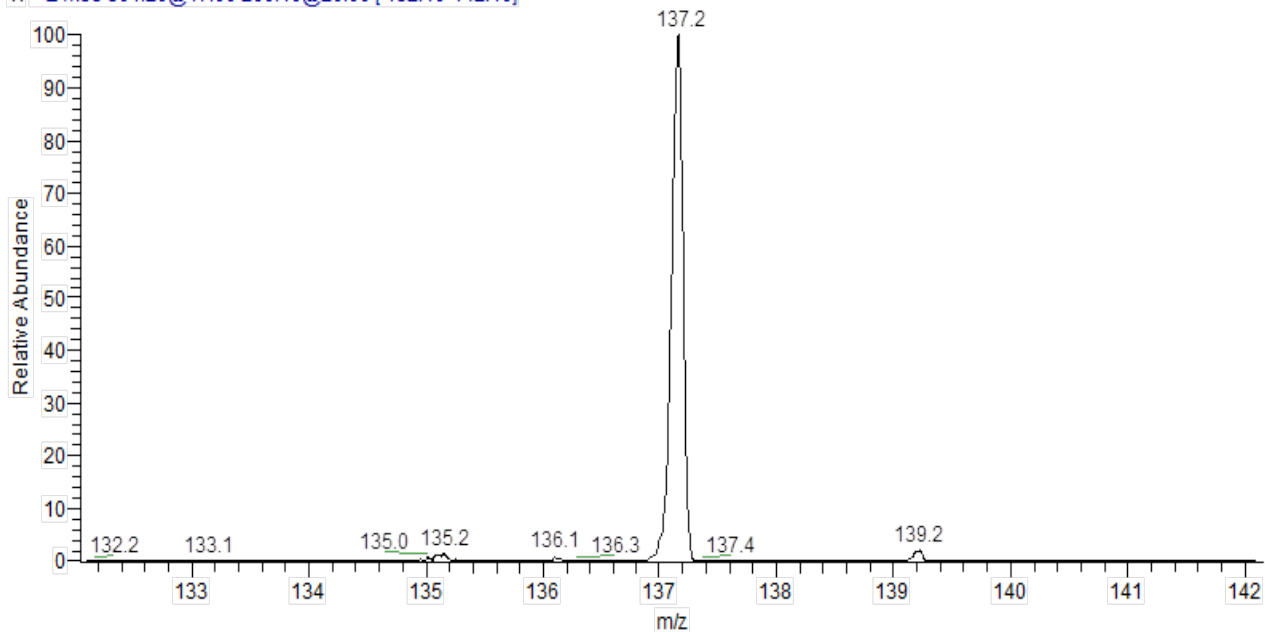
Protonated G1 nitrile-terminated PPI dendrimer – MS<sup>3</sup> 260 m/z; zoom scan at 176 m/z:

ms3\_301\_E17\_T30\_260\_E20\_T30#1-100 RT: 0.02-1.79 AV: 100 NL: 4.61E4  
T: + Z ms3 301.20@17.00 260.10@20.00 [ 171.30-181.30]



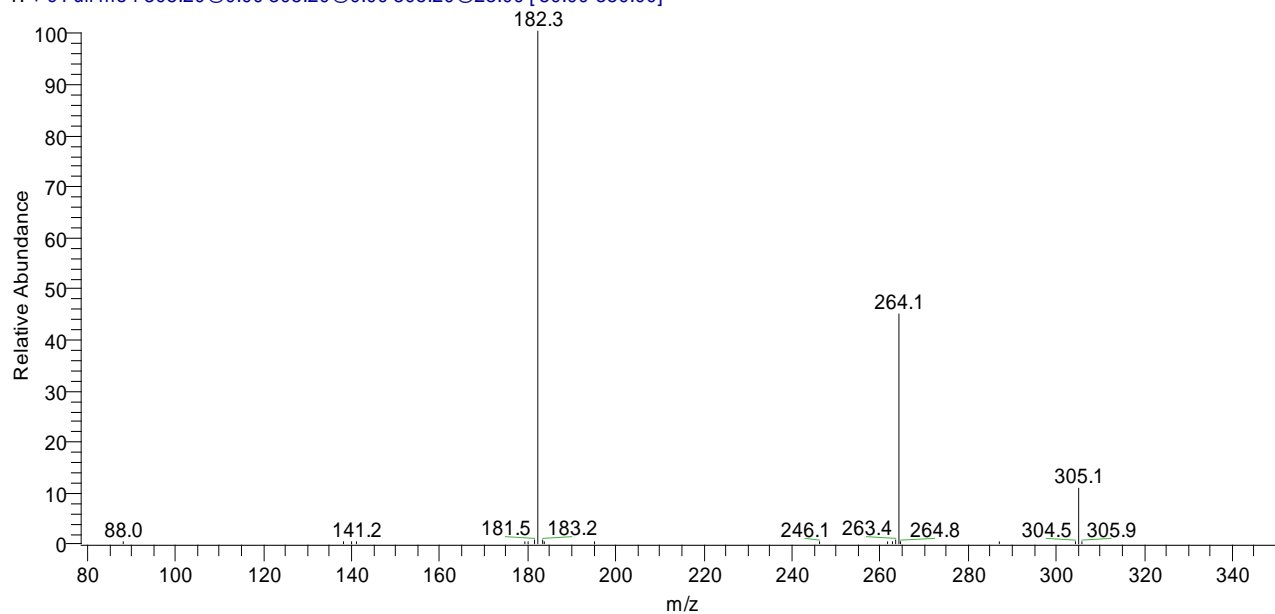
Protonated G1 nitrile-terminated PPI dendrimer – MS<sup>3</sup> 260 m/z; zoom scan at 137 m/z:

ms3\_301\_E17\_T30\_260\_E20\_T30\_zoom137#1-100 RT: 0.02-1.79 AV: 100 NL: 1.66E4  
T: + Z ms3 301.20@17.00 260.10@20.00 [ 132.10-142.10]



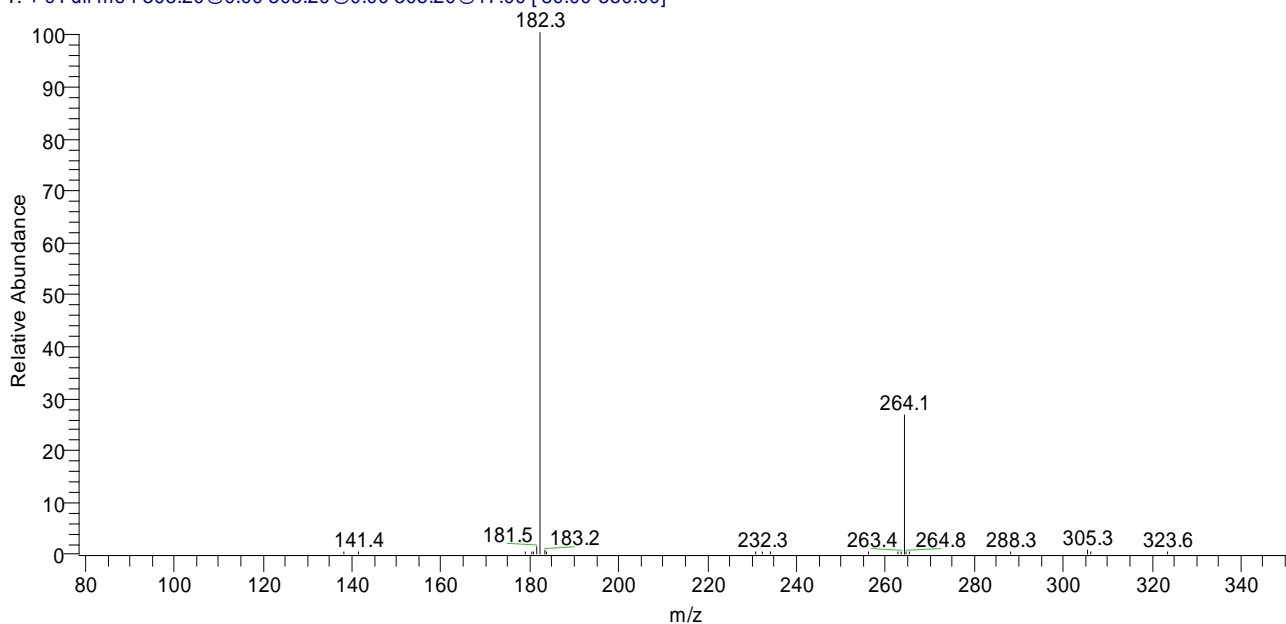
DOC G1 nitrile-terminated PPI dendrimer – MS<sup>2</sup> 305 m/z at 30 ms time:

ms\_2\_305\_E23\_T30#1-20 RT: 0.05-1.01 AV: 20 NL: 7.78E5  
T: + c Full ms4 305.20@0.00 305.20@0.00 305.20@23.00 [ 80.00-350.00]



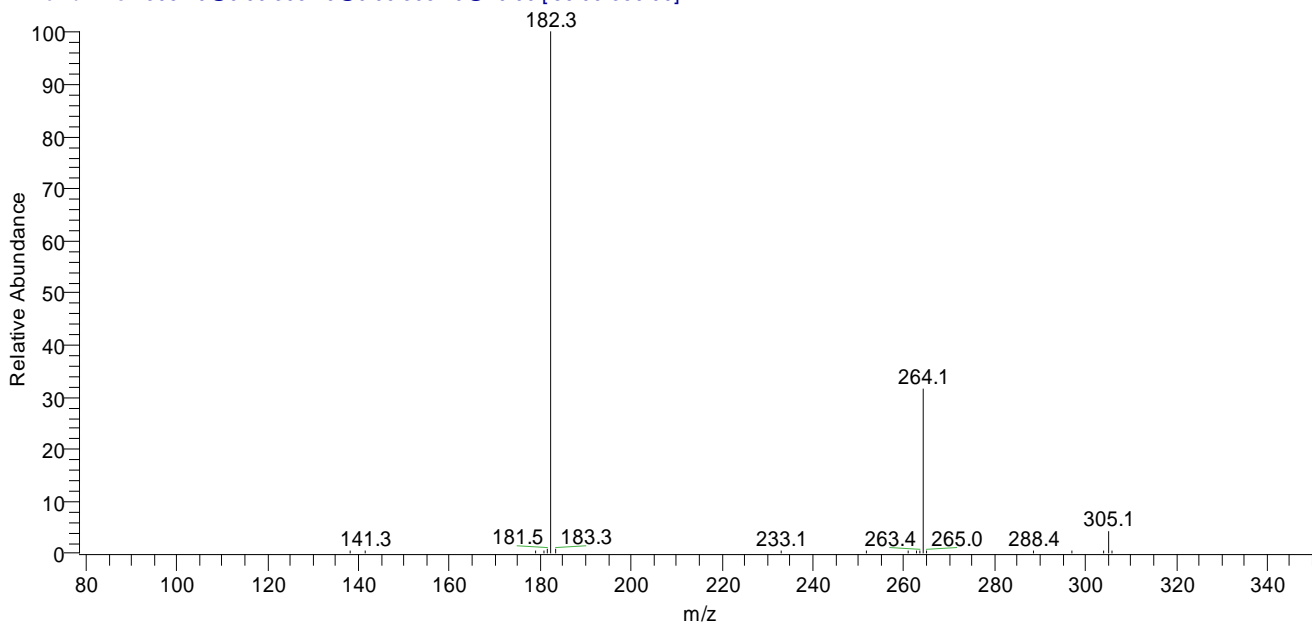
DOC G1 nitrile-terminated PPI dendrimer – MS<sup>2</sup> 305 m/z at 3000 ms time:

ms\_2\_305\_E17\_T3000#1-20 RT: 0.29-5.85 AV: 20 NL: 1.43E6  
T: + c Full ms4 305.20@0.00 305.20@0.00 305.20@17.00 [ 80.00-350.00]



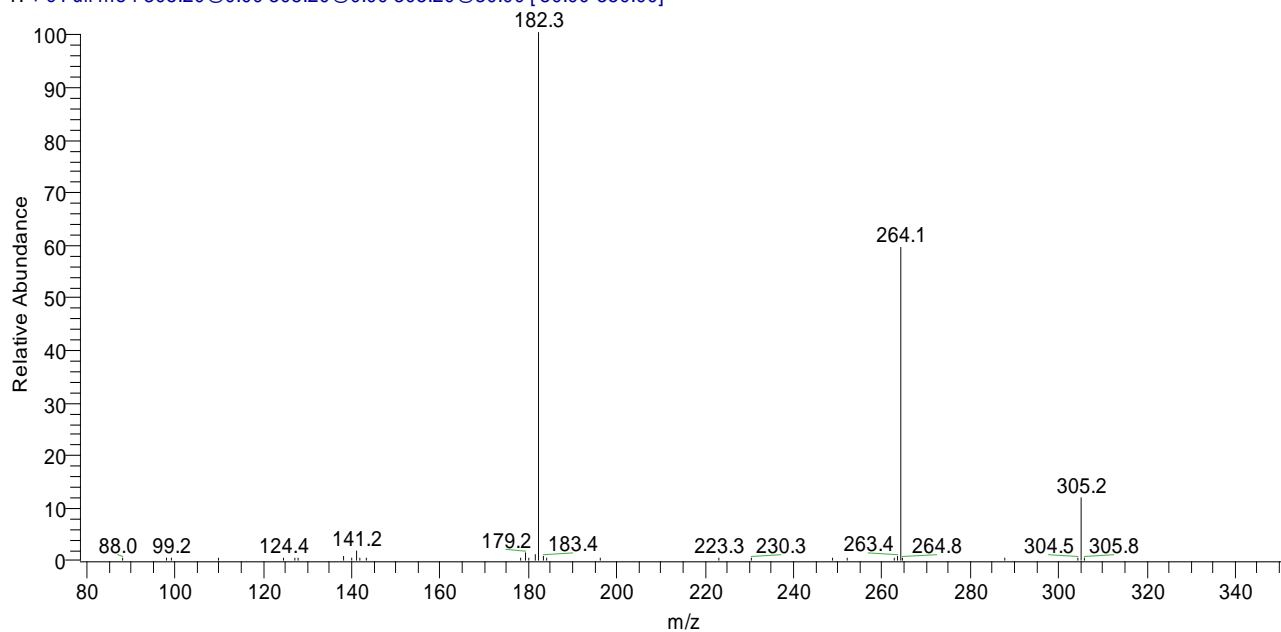
DOC G1 nitrile-terminated PPI dendrimer – MS<sup>2</sup> 305 m/z at 300 ms time:

ms\_2\_305\_E19\_T300#1-19 RT: 0.01-1.28 AV: 19 NL: 9.61E5  
T: + c Full ms4 305.20@0.00 305.20@0.00 305.20@19.00 [ 80.00-350.00]



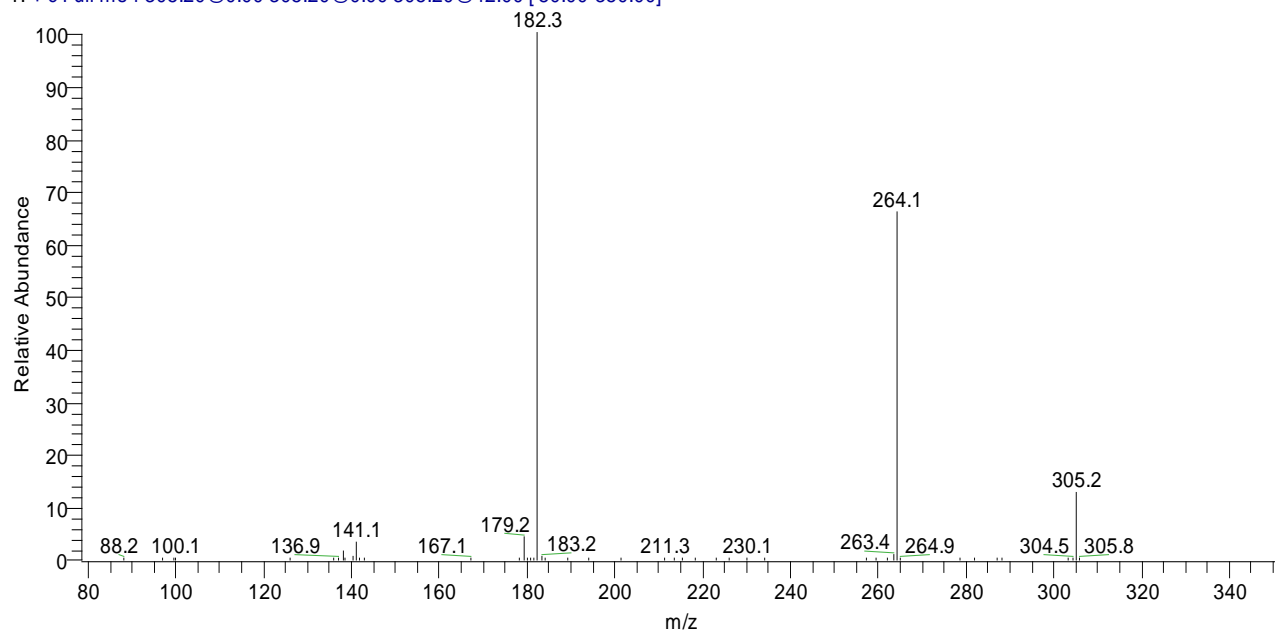
DOC G1 nitrile-terminated PPI dendrimer – MS<sup>2</sup> 305 m/z at 6 ms time:

ms\_2\_305\_E30\_T6#1-20 RT: 0.00-0.91 AV: 20 NL: 7.63E5  
T: + c Full ms4 305.20@0.00 305.20@0.00 305.20@30.00 [ 80.00-350.00]



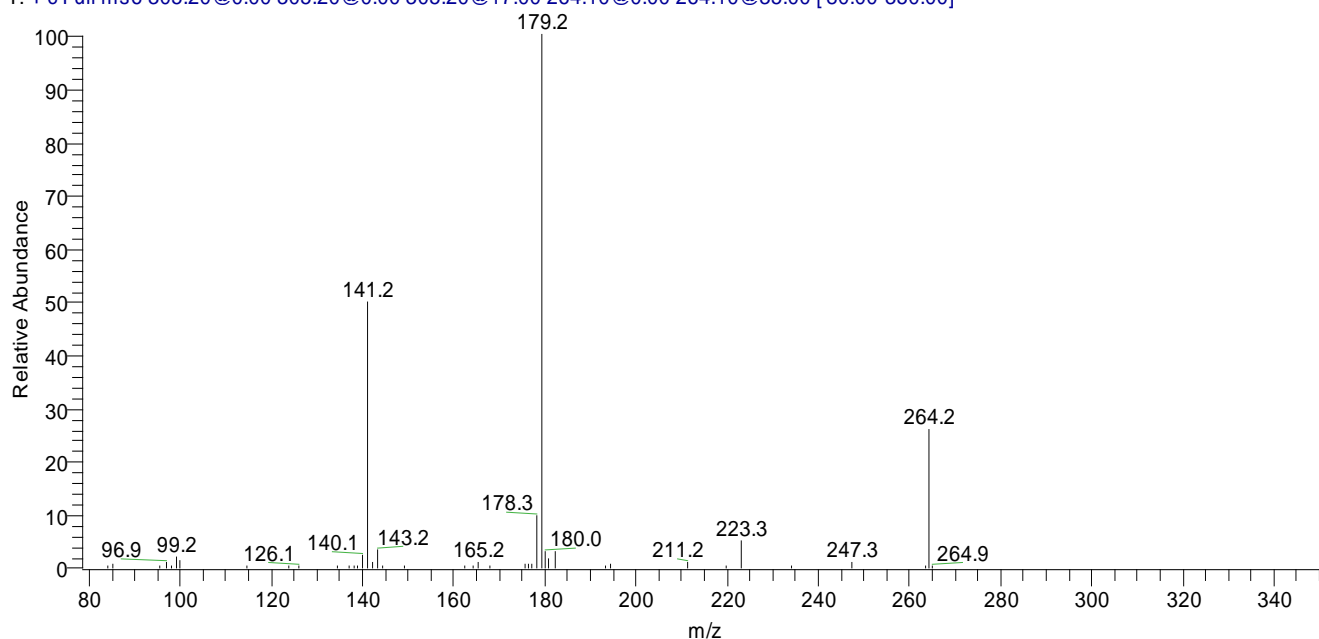
DOC G1 nitrile-terminated PPI dendrimer – MS<sup>2</sup> 305 m/z at 3 ms time:

ms\_2\_305\_E42\_T3#1-20 RT: 0.03-0.93 AV: 20 NL: 5.96E5  
T: + c Full ms4 305.20@0.00 305.20@0.00 305.20@42.00 [80.00-350.00]



DOC G1 nitrile-terminated PPI dendrimer – MS<sup>2</sup> at 3000 ms; MS<sup>3</sup> 264 m/z at 6 ms time:

ms\_3\_305\_E17\_T3000\_264\_E35\_T6#1-20 RT: 0.16-6.00 AV: 20 NL: 5.86E4  
T: + c Full ms6 305.20@0.00 305.20@0.00 305.20@17.00 264.10@0.00 264.10@35.00 [80.00-350.00]

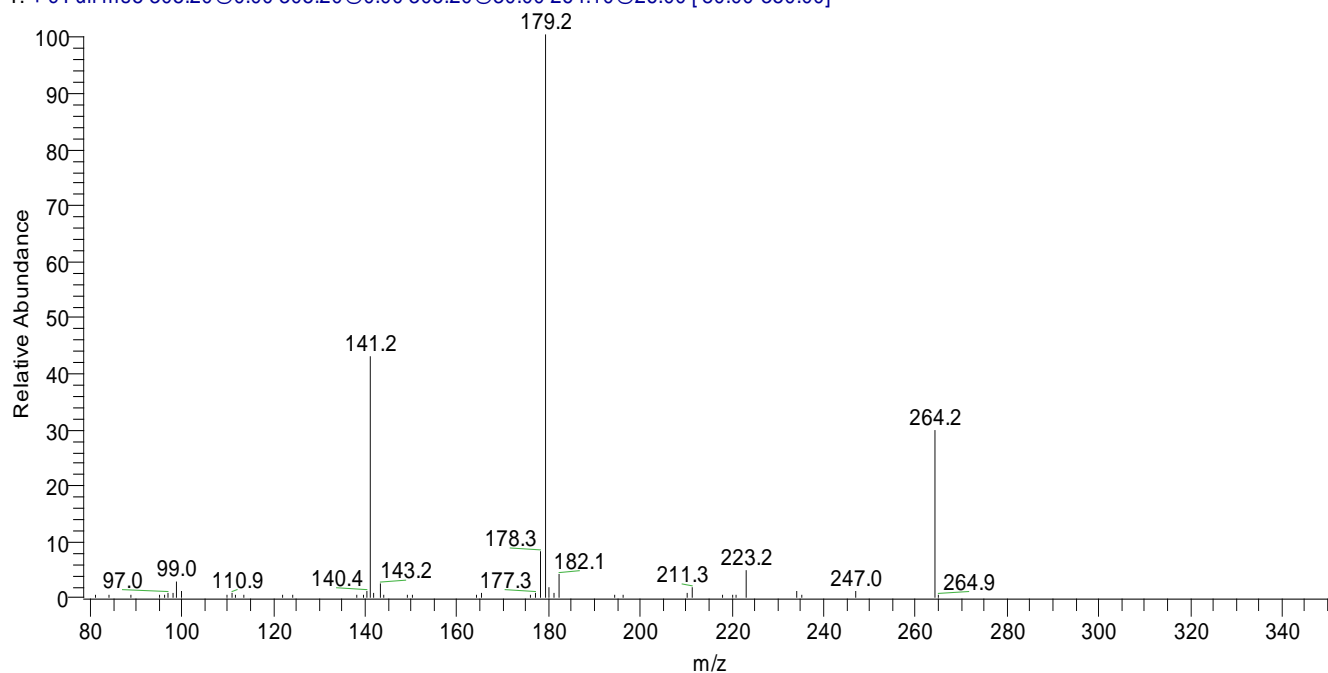




DOC G1 nitrile-terminated PPI dendrimer – MS<sup>2</sup> at 6 ms; MS<sup>3</sup> 264 m/z at 30 ms time:

ms\_3\_305\_E30\_T6\_264\_E26\_T30#1-20 RT: 0.03-0.99 AV: 20 NL: 1.07E5

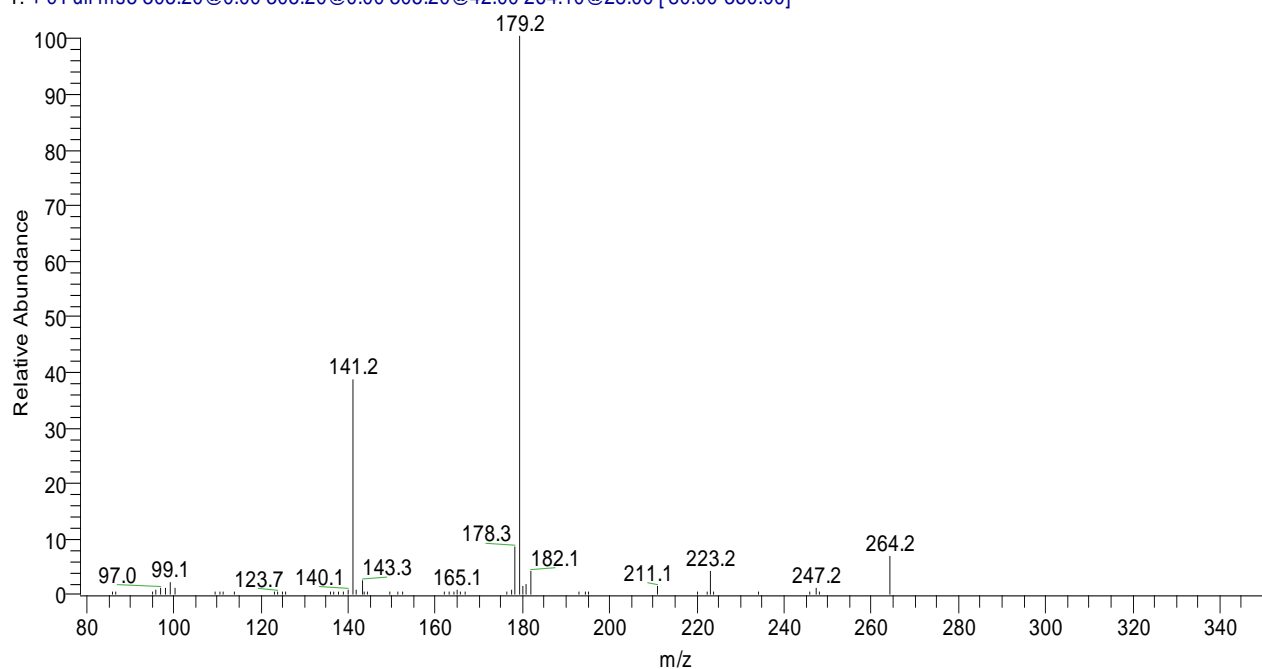
T: + c Full ms5 305.20@0.00 305.20@0.00 305.20@30.00 264.10@26.00 [ 80.00-350.00]



DOC G1 nitrile-terminated PPI dendrimer – MS<sup>2</sup> at 3 ms; MS<sup>3</sup> 264 m/z at 30 ms time:

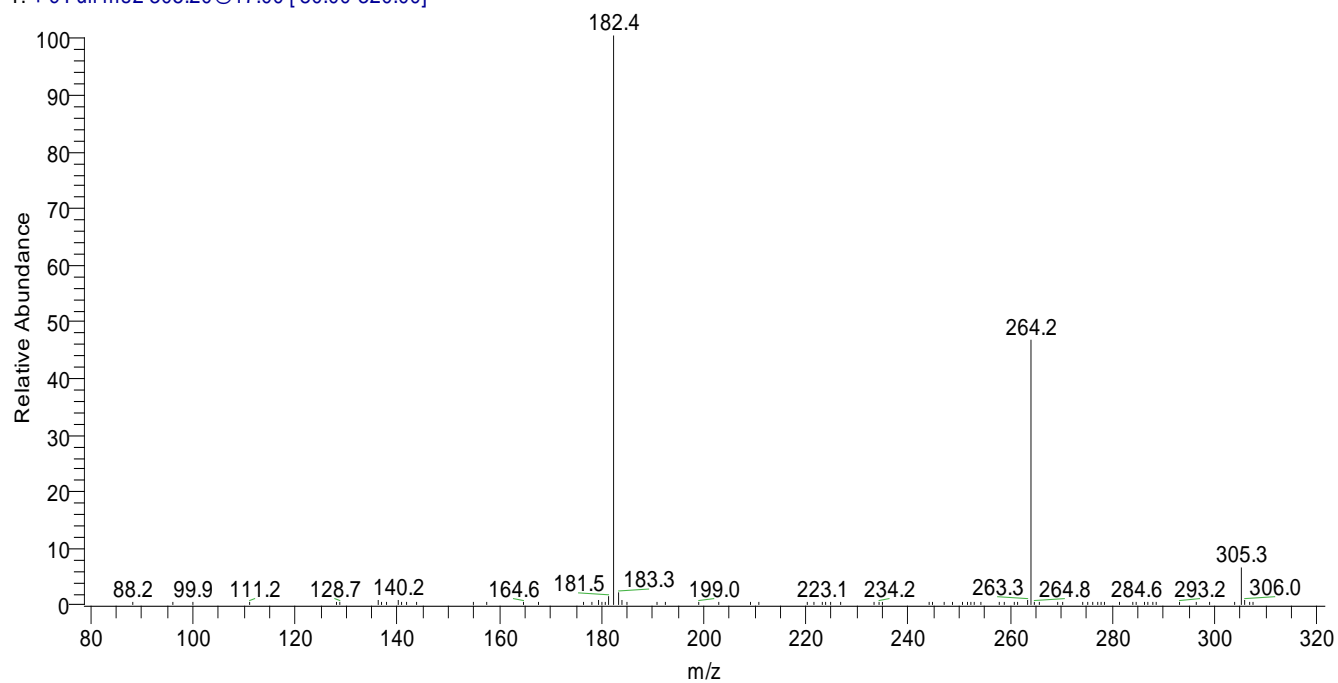
ms\_3\_305\_E42\_T3\_264\_E28\_T30#1-20 RT: 0.04-1.08 AV: 20 NL: 9.52E4

T: + c Full ms5 305.20@0.00 305.20@0.00 305.20@42.00 264.10@28.00 [ 80.00-350.00]



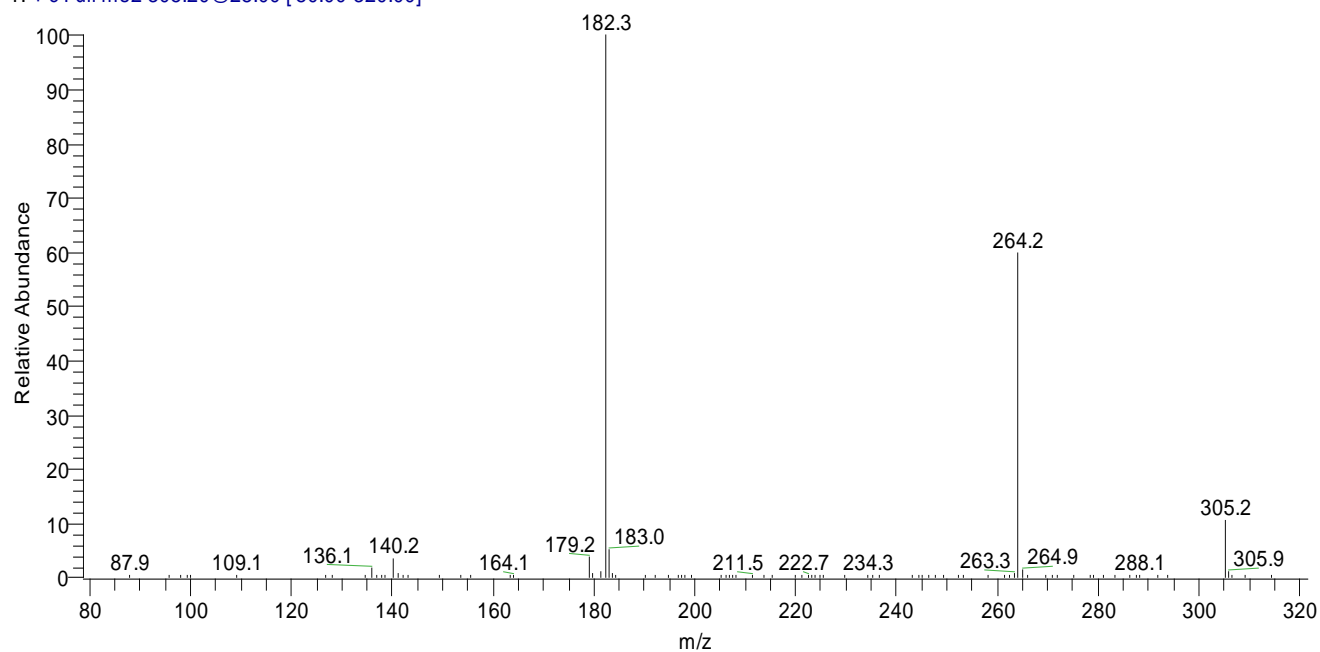
DIC G1 nitrile-terminated PPI dendrimer – MS<sup>2</sup> 305 m/z at 30 ms:

ms2\_305\_E17\_T30#1-100 RT: 0.00-2.09 AV: 100 NL: 1.67E5  
T: + c Full ms2 305.20@17.00 [ 80.00-320.00]



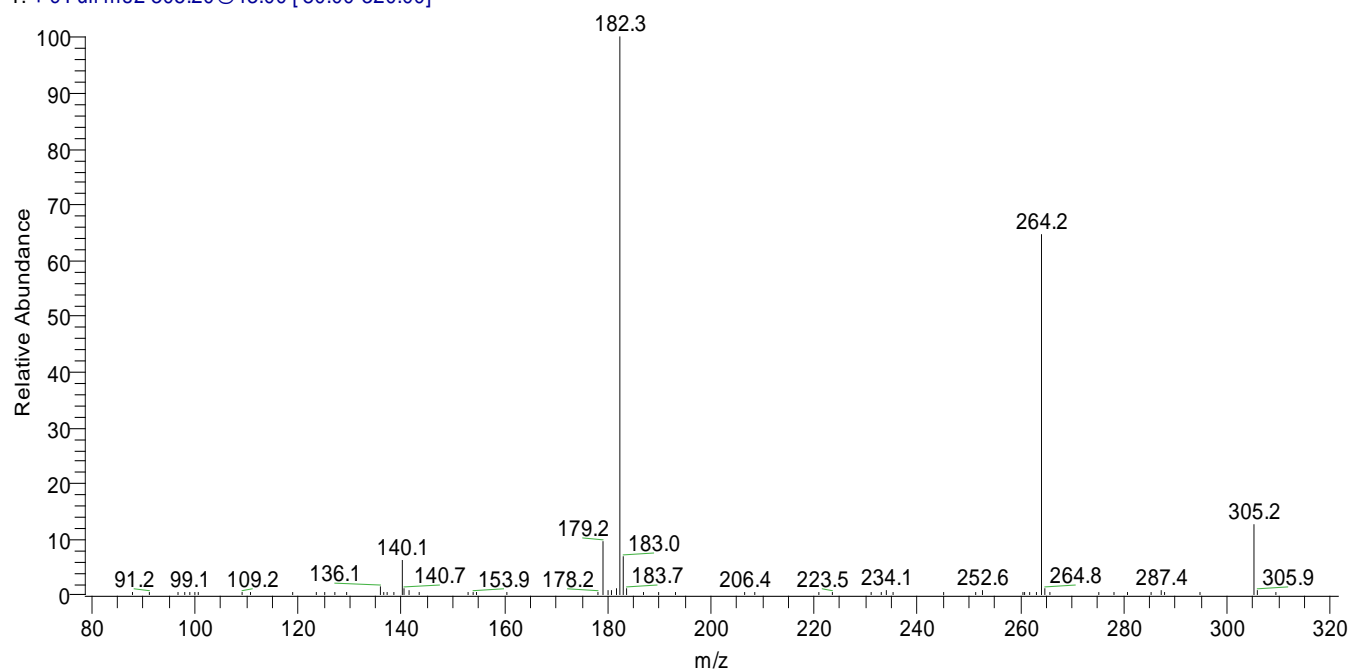
DIC G1 nitrile-terminated PPI dendrimer – MS<sup>2</sup> 305 m/z at 6 ms:

ms2\_305\_E28\_T6#1-100 RT: 0.01-1.98 AV: 100 NL: 1.01E5  
T: +c Full ms2 305.20@28.00 [ 80.00-320.00]



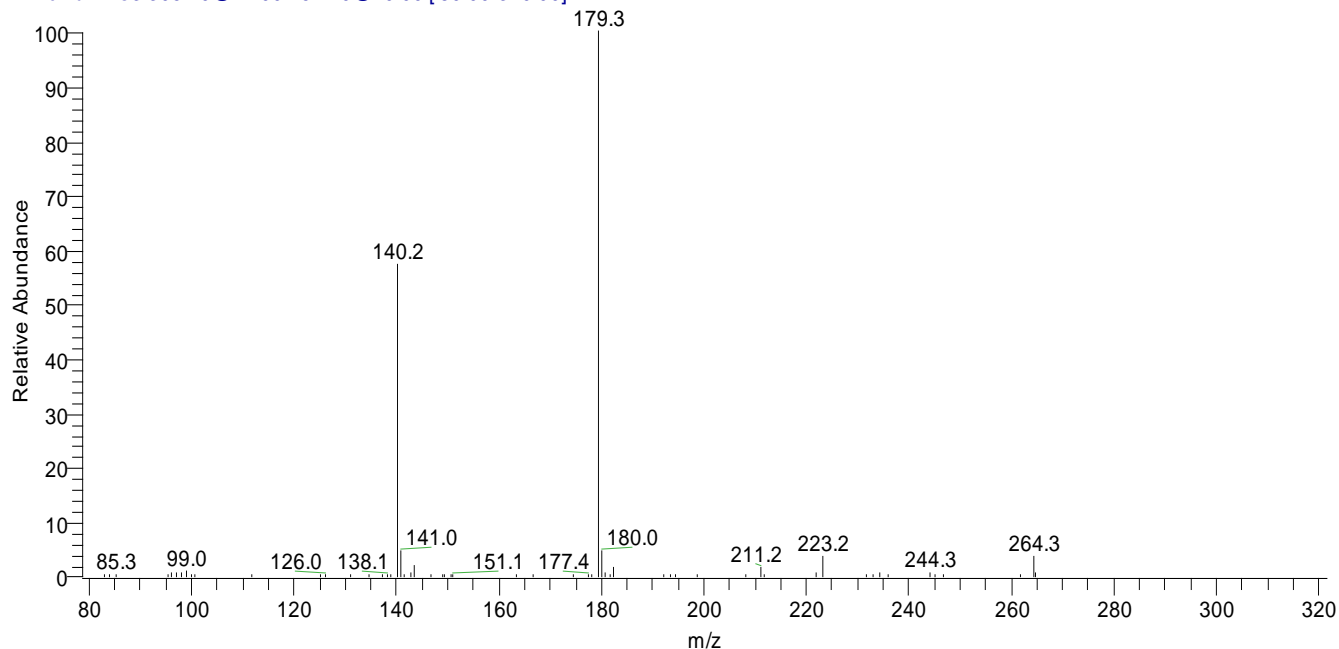
DIC G1 nitrile-terminated PPI dendrimer – MS<sup>2</sup> 305 m/z at 4 ms:

ms2\_305\_E43\_T4#1-100 RT: 0.01-1.97 AV: 100 NL: 2.58E4  
T: +c Full ms2 305.20@43.00 [ 80.00-320.00]



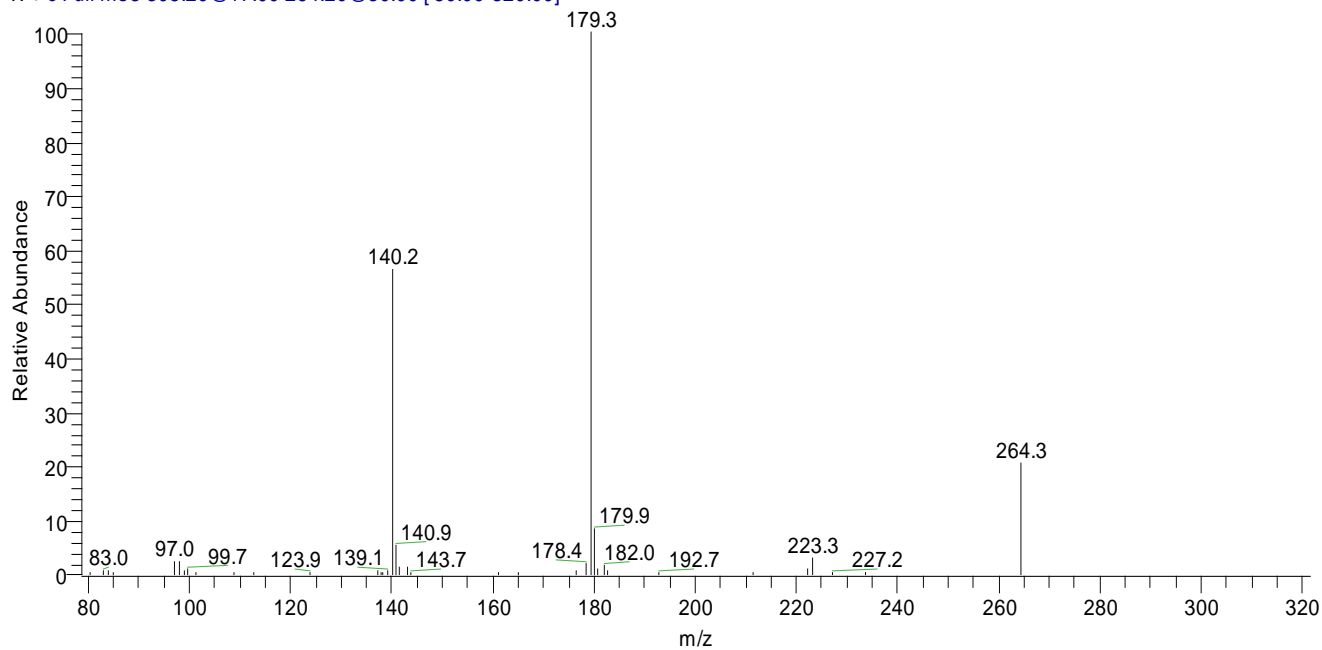
DIC G1 nitrile-terminated PPI dendrimer – MS<sup>2</sup> at 4 ms; MS<sup>3</sup> at 30 ms:

ms3\_305\_E43\_T4\_264\_E20\_T30#1-99 RT: 0.01-2.37 AV: 99 NL: 2.16E4  
T: + c Full ms3 305.20@17.00 264.20@20.00 [ 80.00-320.00]



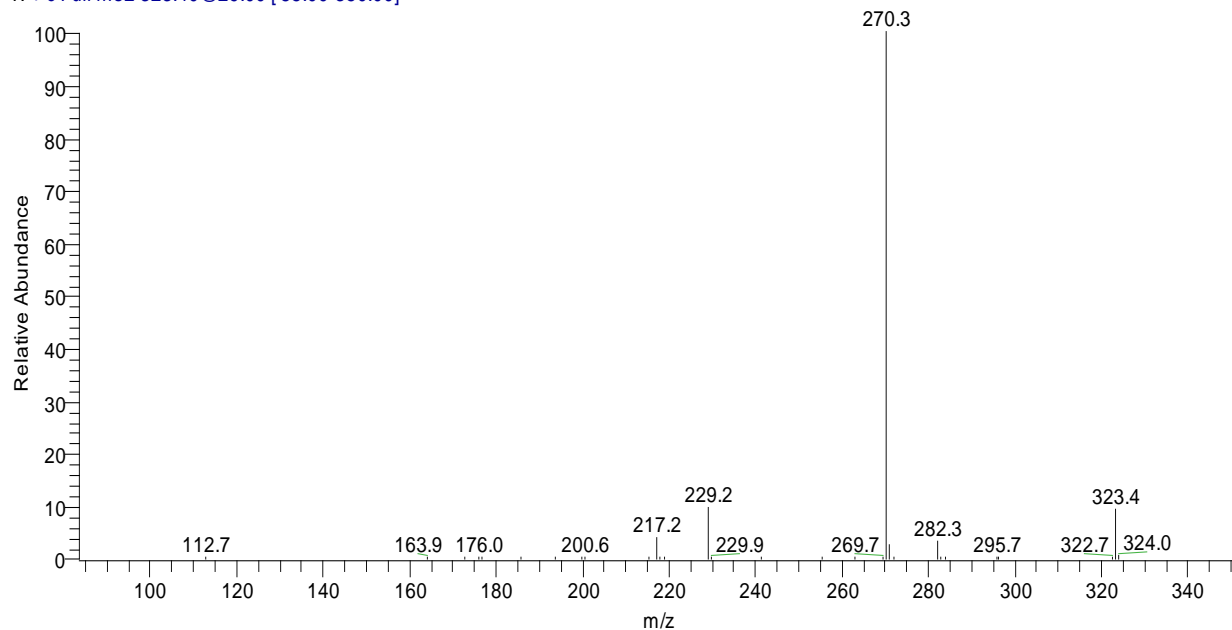
DIC G1 nitrile-terminated PPI dendrimer – MS<sup>2</sup> at 4 ms; MS<sup>3</sup> at 6 ms:

ms3\_305\_E43\_T4\_264\_E30\_T6#1-100 RT: 0.02-2.28 AV: 100 NL: 8.88E3  
T: + c Full ms3 305.20@17.00 264.20@30.00 [ 80.00-320.00]



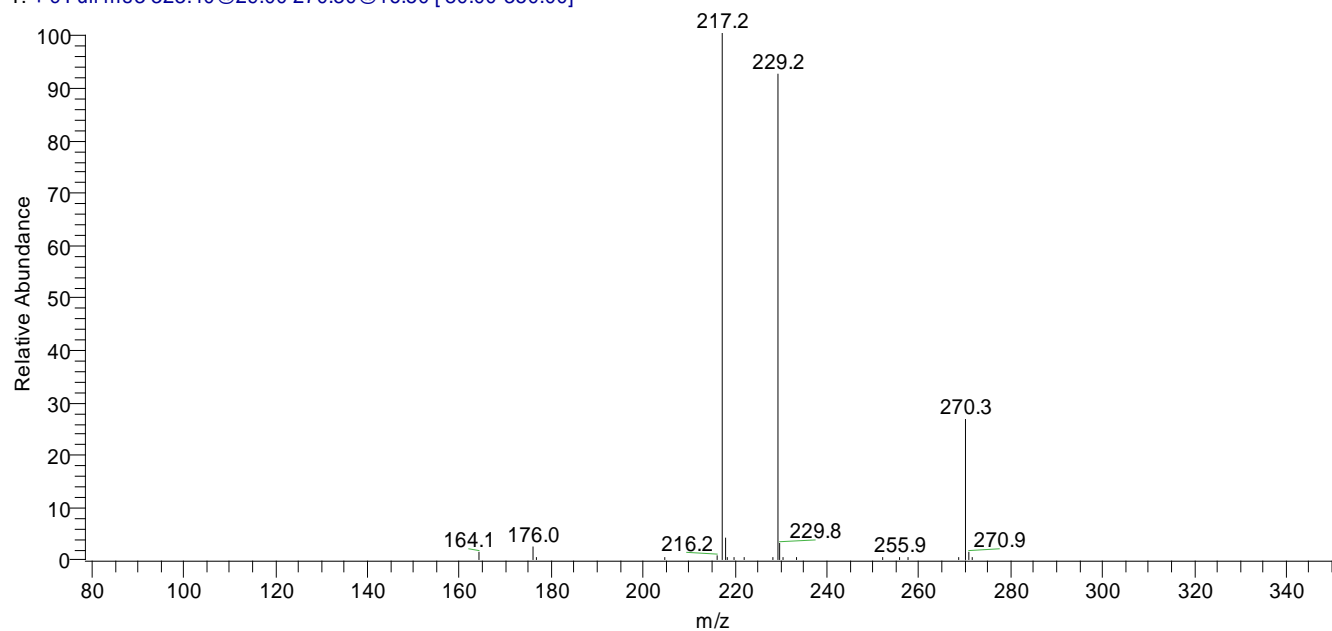
Sodium-G1 dendrimer complex – MS<sup>2</sup> of 323 m/z at 30 ms:

ms2\_323\_29\_30#1-100 RT: 0.00-1.16 AV: 100 NL: 2.34E6  
T: + c Full ms2 323.40@29.00 [85.00-350.00]



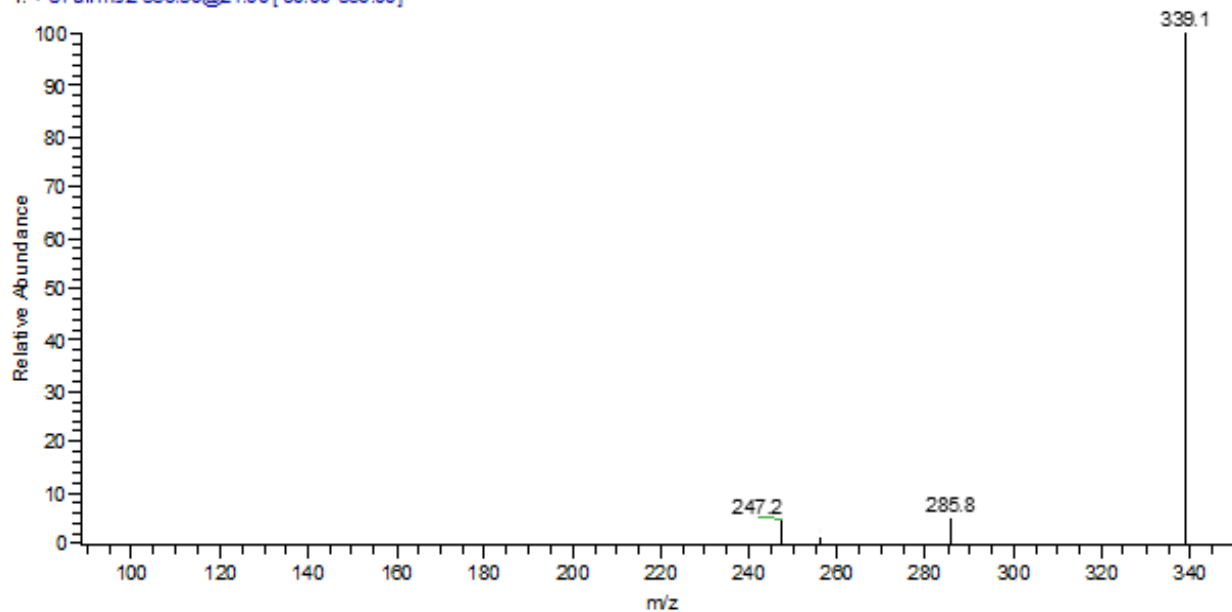
Sodium-G1 dendrimer complex – MS<sup>3</sup> of 270 m/z at 30 ms:

ms3\_270\_16.5\_1000#1-100 RT: 0.01-6.36 AV: 100 NL: 9.14E4  
T: + c Full ms3 323.40@29.00 270.30@16.50 [80.00-350.00]



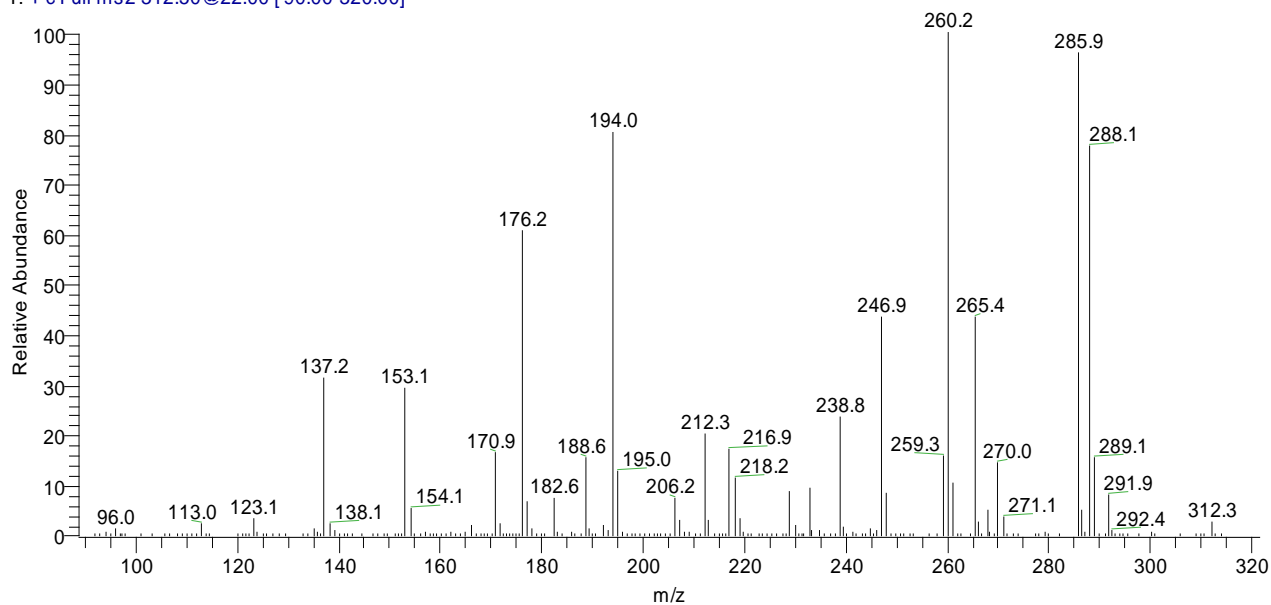
### Potassium-G1 dendrimer complex – MS<sup>2</sup> of 339 m/z at 30 ms:

ms2\_393\_E24\_T30#1-100 RT: 0.00-1.92 AV: 100 NL: 3.70E2  
T: + c Full ms2 339.30@24.00 [ 90.00-350.00]



### Magnesium-G1 dendrimer complex – MS<sup>2</sup> of 312 m/z at 30 ms:

ms2\_312\_22\_30\_2#1-100 RT: 0.00-1.15 AV: 100 NL: 5.14E6  
T: + c Full ms2 312.50@22.00 [ 90.00-320.00]



Calcium-G1 dendrimer complex – MS<sup>2</sup> of 320 m/z at 30 ms:

ms2\_320\_E19\_T30#1-100 RT: 0.01-1.18 AV: 100 NL: 1.65E7

T: +c Full ms2 320.20@19.00 [90.00-350.00]

